NEAR-CONSTANT BEAMWIDTH WIDEBAND HORN ANTENNA DESIGN

by
Türker İsenlik

Submitted to Graduate School of Nature and Applied Sciences
in Partial Fulfillment of the Requirements
for the Degree of Doctor of Philosophy in
Electrical and Electronics Engineering

Yeditepe University
2019

NEAR-CONSTANT BEAMWIDTH WIDEBAND HORN ANTENNA DESIGN

APPROVED BY:

Prof. Dr. Duygun Erol Barkana
(Thesis Supervisor)

Prof. Dr. Ahmet Arif Ergin

Prof. Dr. Korkut Yeğin

Assoc. Prof. Dr. Hamid Torpi

Assoc. Prof. Dr. Serkan Topaloğlu

DATE OF APPROVAL: ..../..../2019

ACKNOWLEDGEMENTS

ABSTRACT

NEAR-CONSTANT BEAMWIDTH WIDEBAND HORN ANTENNA DESIGN

The use of horn antennas is increasing because of their need in wideband, and high gain antenna applications. Beamwidth constancy along the wideband becomes particularly important and necessary in applications such as direction finding (DF) and reflector antenna feeds. We propose a design methodology for near-constant beamwidth, wideband, corrugated double ridged horn antenna over 4:1 frequency band in this thesis.

In this study, the beamwidth constancy is not restricted to a single-plane or to a symmetrical geometry antenna which has a limited bandwidth (BW) ratio of 2:1. Rather, we aimed to design a rectangular horn with constant beamwidths at both azimuth and elevation planes from 4.5 to 18 GHz. We first design X-band standard gain horn antenna (SGHA) to understand the characteristics of horns and a conventional double ridged horn antenna (DRHA) to use it as a reference for beamwidth variation of wideband horns through the operating band. We also investigate the root causes that impede the antenna from constant beamwidth along wideband, and the requirements to achieve the beamwidth constancy. We first modify the DRHA to design near-constant beamwidth wideband horn antenna (NCBWHA), and then use structures called "pinwall" and "stepped-shape corrugated slot", which are implemented in H-plane sidewalls and in E-plane walls, respectively. We derive the input admittance of a new step-shaped slot, and then determine the bandwidth by comparing to conventional corrugations. The proposed corrugation presents wideband characteristics with a BW ratio of more than 4:1. We also designed a broadband double ridged waveguide-to-coaxial (rwg-to-coax) adapter to match the antenna impedance to 50 Ω.

After the design is completed in simulations, two different prototypes of antennas are built which are coax-fed curved pinwall DRHA and NCBWHA. The radiation pattern and other parameters of manufactured antennas are measured using a commercially available near-field system. We observe that the measurement results corroborate with simulation ones fairly well. The proposed antenna in this study has 4:1 wideband characteristics with $31.0^{o}\pm2.5^{o}$ in H-plane and $37.4^{o}\pm5.2^{o}$ in E-plane 3-dB beamwidths.

ÖZET

SABİT HÜZMELİ GENİŞ BANTLI HUNİ ANTEN TASARIMI

Geniş bantlı ve yüksek kazançlı anten uygulamalarında huni antenlere olan ihtiyaç nedeniyle söz konusu antenlerin kullanımı artmaktadır. Geniş bant boyunca hüzmenin sabit kalması, özellikle yön bulma (DF) uygulamaları ve yansıtıcılı anten beslemeleri gibi bazı alanlarda önemli ve gerekli hale gelmektedir. Bu tezde, 4:1 bant genişliği oranını sağlayan, yaklaşık-sabit hüzmeli, geniş bantlı, oluklu, çift mahyalı horn antenin tasarım yöntemi açıklanmıştır.

Bu çalışmada sabit hüzme özelliği yalnızca tek bir düzleme ya da bant genişliği 2:1 oranıyla sınırlı simetrik geometrili bir antene sınırlandırılmamıştır. Onun yerine, 4.5 – 18 GHz bandında, hem yatay, hem düşey eksenlerde sabit hüzme özelliği gösteren dikdörtgen huni anten tasarlanmıştır. Öncelikle, huni antenlerin karakteristiğini anlamak için X-bant standart kazançlı huni anten (SGHA) ve geniş bantlı huni antenlerin çalışma bandı boyunca hüzme değişimine referans olması için klasik çift mahyalı huni anten (DRHA) tasarlanmıştır. Geniş bant boyunca antenin sabit hüzmeli olmasını engelleyen sebepler ve sabit hüzmeli olması için gerekenler araştırılmıştır. İlk olarak DRHA modifiye edilmiş, ardından H-düzlem yanduvarları için "çubuk"lar, E-düzlem duvarları için ise "basamaklı oluk"lar kullanılarak NCBWHA tasarlanmıştır. Yeni olukların giriş admitans denklemleri çıkartılmış ve bant genişliği grafiği klasik oluklar ile karşılaştırmalı olarak verilmiştir. Önerilen yeni oluk 4:1 oranından daha büyük bir bant genişliği sunmaktadır. Bu arada, 50 Ω empedans uyumunu sağlayacak şekilde dalgakılavuzu-koaksiyel adaptör tasarımı da yapılmıştır.

Anten tasarımı sırasında elde edilen başarılı simulasyon sonuçlarından sonra tasarlanan antenlerden iki tanesi üretilmiştir. Üretilen antenlerin ışıma diyagramları ve diğer parametreleri mevcut bir yakın alan ölçüm sistemi ile ölçülmüştür. Ölçüm sonuçlarının simulasyonlar ile uyumlu olduğu görülmüştür. Sunulan geniş bantlı anten, 4:1 bant boyunca, H-düzlemde $31.0^{o}\pm2.5^{o}$, E-düzlemde $37.4^{o}\pm5.2^{o}$ 3-dB hüzme genişliğine sahiptir.

TABLE OF CONTENTS

LIST OF FIGURES

LIST OF TABLES

LIST OF SYMBOLS/ABBREVIATIONS

ATAM	Antenna Measurement and Research Center
BILGEM	Advanced Technologies of Informatics and Information Security Research Center
BW	Bandwidth
CST	Computer simulation technology
Dbw	Directivity-beamwidth
DF	Direction finding
DRHA	Double ridged horn antenna
ELINT	Electronic intelligence
EM	Electromagnetic
EW	Electronic warfare
HPBW	Half power beamwidth
NCBWHA	Near-constant beamwidth wideband horn antenna
QRFH	Quadruple-ridged flared horn
RLCW	Ring-loaded corrugated waveguide
SGHA	Standard gain horn antenna
SLL	Side lobe level
SNF	Spherical near field
SNR	Signal to system noise ratio
TE	Transverse electric
TEM	Transverse electromagnetic
TM	Transverse magnetic
TUBITAK	Scientific and Technological Research Council of Turkey
UWB	Ultra-wideband
VSWR	Voltage standing wave ratio

1. INTRODUCTION

1.1. PROBLEM STATEMENT

Frequency bandwidth requirements for continuously increasing countermeasure applications, direction finding (DF) systems, and reflector antennas lead to the development of broadband, high gain and constant beamwidth antennas. Microwave and millimetre wave remote sensing, electromagnetic compatibility testing, accurate antenna measurements, electronic warfare (EW), and radar systems are all application areas where broadband horn antennas are widely used.

The conventional horn antennas have well-known properties such as high gain, ease-to-construct, low voltage standing wave ratio (VSWR), well-shaped beam, relatively stable phase center and adjustable beamwidth. However, these properties may not be sufficient for some applications such as wideband reflector antenna feeds and certain DF systems based on amplitude comparison.

As horns are used on their own, they are often used as a primary feed for reflector antennas which are the first choice in many applications such as radio astronomy, point-to-point communications or any applications that require high gain, low side lobes, and high-performance directional antennas. The properties that are important for the feed antenna in reflector antenna design are radiation pattern, VSWR, location of the phase center, and the frequency dependence of these properties. The way to design a highly efficient, low side lobe level, wideband reflector antenna is that the feed of the reflector should be broadband, and the phase center should not change too much along the frequency band. The performance of the feed directly affects the performance of the reflector.

Although different DF techniques require several antenna elements and systems, wide bandwidth and pattern stability are usually the desired features. The magnitudes of the signal captured by various adjacent antennas of an array are compared to determine the direction of transmission of the signal in many DF applications, i.e. amplitude comparison. The performance of such a DF system is limited by signal to system noise ratio (SNR), antenna pattern stability, and receiver channel stability [1]. Besides the properties like

input VSWR and boresight gain, the 3-dB beamwidth constancy is also important for DF applications because this affects detection sensitivity [1]. Thus, it is desirable to use an antenna that should provide a relatively high gain with a constant half power beamwidth (HPBW) over a wide frequency range to obtain accurate bearing information, and to meet the requirements of broadband DF systems. The crossing level for beams coming from adjacent horns must be at the same point along the frequency band regardless of the fact that the beamwidth obtained from an aperture type antenna is inversely proportional to the aperture physical dimensions of the wavelength [2], [3].

Note that it is also possible to use sinuous/spiral and log-periodic type frequency-independent antennas for wideband reflector antenna feeds and DF systems. Spiral antennas are frequency-independent and they are low-gain antennas with high back lobes. The gain varies between -6 dBi and 6 dBi depending on the diameter of the antenna. It is possible to lower the back-lobe levels, and to increase the antenna gain by forming a cavity with the metal surface behind the antenna. However, the distance to the metal surface behind the antenna will vary along the frequency band in terms of wavelength, thus the gain increase will be in very narrow band, and will cause ripple in the antenna pattern outside that region. Therefore, the purpose of using the metal cavity behind the antenna is not to increase the gain along the wideband, but rather to reduce the back-lobe levels. The distortions that may occur in the radiation diagram of the antenna with reflections from the metal surface can be prevented using absorbing material in the cavity [4], [5]. Additionally, the spiral antenna has a constraint in polarization, and it can be designed only right hand or left hand circular polarized. Thus, if linear polarization is desired, then the gain will fall approximately 3 dB. Furthermore, it is not possible to change the beamwidths of the antenna patterns.

Sinuous antennas are also similar to spiral antennas in terms of gain, bandwidth, power strength, and radiation pattern characteristics. Sinuous antennas are generally designed to radiate in one direction by adding a cavity structure to the back of the antenna as in the spiral antenna. The biggest difference between sinuous and spiral antennas is their polarization capabilities. In sinusoidal antennas, there are two ports, which are perpendicular to each other (one port is for horizontal polarized waves and the other one is vertical polarized signal, or one port is for right hand circular polarized and the other one is left hand polarized signal). Therefore, it is possible to receive the signal in all polarizations

which is an important feature for applications such as EW/DF systems. Reception of all polarizations does not allow any signals in the system's range to be missed due to polarization.

Log-periodic is extremely wideband antenna with higher gain than sinuous and spiral antennas, but lower gain than horn antennas. The beamwidth of log-periodic antenna is near-constant. However, log-periodic antenna consists of a number of half-wave dipole driven elements of gradually increasing length, and the phase center of log-periodic antennas varies along the frequency band too much due to position variation of active regions at different frequencies [6]. The phase center variation causes extra spillover losses, and lowers the radiation efficiency, and causes high side lobe levels when it is used as a reflector feed. Furthermore, the physical dimension and coupling can be a problem when positioning the log-periodic antenna in the array at low frequencies.

If a horn that provides the desired characteristics such as pattern stability and near-constant beamwidth with the BW ratio of 3:1 or wider can be designed, then it will remove the negative aspects of other wideband antennas. It should be noted that designing a horn antenna offers more freedom and flexibility to the designer than designing spiral/sinuous type or log-periodic antennas in terms of antenna parameters. Furthermore, horn antennas allow independent control over azimuth and elevation beamwidths, which is important since the beamwidths can be chosen to enable different numbers horn array systems to be devised.

The radiation patterns and beamwidths of conventional horn antennas vary linearly with frequency as shown in Figure 1.1. The beamwidth of the main lobe is inversely proportional to the physical dimensions of the aperture in wavelengths because of the path length differences. The difference increases with frequency, and it generates a phase variation across the aperture that causes significant variation of radiation patterns with frequency. The vital point of the wideband horn problem lies in the form of the electromagnetic fields at the horn aperture. Flared horns had been originally designed to have a similar aperture field distribution of open ended waveguide with a quadratic phase error imposed [1].

If such a conventional horn has a narrow flare, then there is a nearly constant phase along the aperture. Since the beamwidth depends on the dimension of the aperture measured in

wavelengths, the beamwidth also reduces when frequency is increased. Thus, large flare horns are used to have a phase distribution across the aperture that increases with successive frequency. The phase distribution causes a wider beam at higher frequencies, and consequently the changes in the beamwidth are noticed to be less. However, the radiation patterns of such horns still vary significantly with frequency.
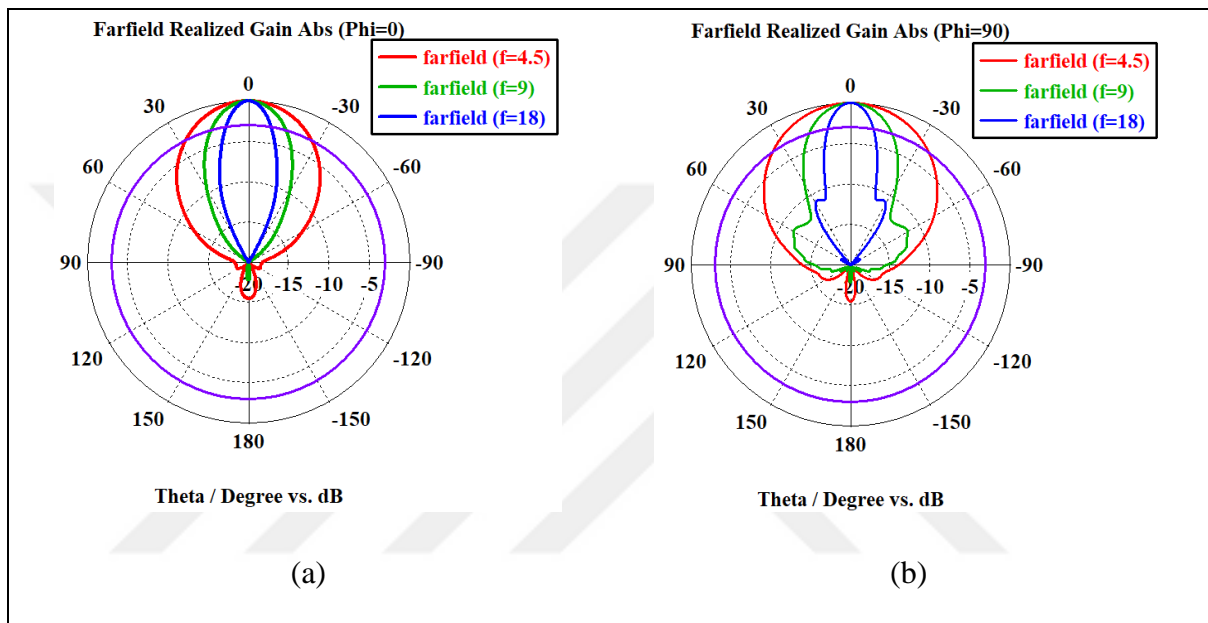
Figure 1.1. Normalized (a) azimuth and (b) elevation beamwidth variations of double ridged horn antenna (DRHA) from 4.5 to 18 GHz

Another significant problem in wideband horns is the higher-order modes. If the horn has more than one mode present in waveguide, then the radiation pattern can vary significantly with frequency, and degrade constant beamwidth property of the horn antenna. This is because of the phase relation of the modes at the aperture mouth of the horn varies, and changes in the field distribution at the aperture. The rectangular, circular or any shaped metallic hollow waveguides cannot support Transverse Electromagnetic (TEM) waves, and there is no cut-off frequency for waveguides that support TEM waves. On the other hand, Transverse Electric (TE) or Transverse Magnetic (TM) modes have particular cut-off frequencies that cause radiation of higher order modes as the frequency band expands. These higher order modes deteriorate the antenna characteristic parameters, especially pattern form and beamwidths.

Most of the studies of broadband, corrugated, or nearly constant beamwidth horn antennas in the literature generally prefer cylindrical, conical or single-plane (mostly H-plane) sectoral geometries. Cylindrical or conical geometries provide simpler analysis and manufacturing due to their axial symmetry, and single-plane sectoral horns provides a relatively simple design procedure. In this dissertation, we design a wideband rectangular horn antenna with a constant beamwidth property in all planes that can also provide us capabilities to obtain independent E- and H- plane radiation patterns.

1.2. PURPOSE

The aim of this dissertation is to design a NCBWHA, and to analyse the impact of design parameters on the performance of an antenna. A design methodology to develop a new type horn antenna that satisfies a constant beamwidth over an extremely wide frequency range is proposed. The design objectives are constant azimuth and elevation pattern beamwidths over the BW ratio of 4:1 (4.5 to 18 GHz), and better typical VSWR than a ratio of 2.5:1. The intended H-plane half-power beamwidth (HPBW) is about 30 degrees and the desired gain is more than 10 dBi along the frequency band.

The beamwidth of the pattern is defined as the angular separation between two identical points on the opposite side of the pattern maximum [7]. Half-power beamwidth (or 3-dB beamwidth) and 10-dB beamwidth are widely used ones. 10-dB beamwidth term is usually used in reflector antenna designs. Therefore, we are more interested in 3-dB beamwidth in this dissertation. Since the aperture/wavelengths ratio varies with frequency change, the directivity and the beamwidth of conventional horn antenna also change along the operating frequency band. Thus, the classic horn antenna is not a frequency-independent antenna and it is subject to the usual $1/f$ variation of beamwidth with frequency. In this context, "near-constant beamwidth" does not mean that the beamwidth remains absolutely constant. "Near-constant beamwidth" indicates that the designed antenna achieves almost-constant beamwidth compared to frequency variance in the entire frequency band, and breaks down the 1/f relation between frequency and beamwidth. It should be noted that analytical solutions do not exist for the fields due to the complexity of boundary conditions with these types of cross sections that are being studied in this dissertation. Therefore, numerical analysis is also used to model corrugated walls and pinwall sidewalls along with

analytical derivations during the design and development of broadband structure employing ridged waveguides with tapered ridges.

1.3. RESEARCH CONTRIBUTION

The main research contribution of this dissertation is to propose a design methodology for double ridged horn antenna with constant beamwidth property, and to meet an antenna requirement that have relatively high gain, wideband with a BW ratio of 3:1 or more, stable phase center location, independent azimuth and elevation beam control and constant beamwidth features. There are antennas that satisfy one or more of the above features, however the contribution of this dissertation will be the design of an antenna that has all the aforementioned properties at the same time. We make changes in geometries using different structures such as pinwall (grid) and stepped-shape slot in flare walls of the horn which form boundary conditions that directly affect the radiation diagrams of the antenna. Curved pinwall sidewalls and novel corrugated slot geometry will be introduced into the current state of the art antenna designs. A constant beamwidth will be achieved throughout the bandwidth that has not been achieved so far with these new structures. Furthermore, straightforward design procedure for DRHA will be presented starting from the ridged waveguides.

1.4. OUTLINE

The problem statement, objective and scope of the dissertation are provided in Section 1.1, Section 1.2 and Section 1.3, respectively. The rest of the dissertation is organised as follows:

Chapter 2 presents background information about waveguides and ridged waveguides. Since the horn antenna is a type of shaped and flared waveguide and the most important reason of the deterioration of radiation patterns is the higher-order mode propagations, it is necessary to understand the waveguide structure and the notion of modes. Furthermore, the ridge waveguides are also discussed in this chapter because the bandwidth of conventional rectangular waveguide and horn antenna can be improved using the ridges. Important

parameters such as impedance, BW, cut-off frequency, propagating higher-order modes, field distributions are also defined and derived.

Chapter 3 presents information about the X-band standard gain horn antenna (SGHA) and other double ridged horn antenna designs. The design procedures are explained and the antennas are modelled and analysed using CST-Microwave Studio EM simulation software program (full-wave 3D EM-solver). The bandwidths of the antennas, the frequency dependence of beamwidth, and higher-order modes propagation are also examined. The DRHA is designed to extend the operating frequency bandwidth because the designed SGHA has relatively limited bandwidth, and it does not provide the target bandwidth which is in the order of minimum 3:1 BW ratio.

The design of a constant beamwidth broadband horn antenna is detailed in Chapter 4. The literature review on near-constant beamwidth wideband horn antenna (NCBWHA) has been presented. The reasons of difficulty to achieve constant beamwidth along wideband are given and ways to achieve the constant beamwidth are also investigated in this chapter. The structures are implemented in the new type of DRHA design.

Chapter 5 presents the performance of the manufactured antennas. The antenna parameters such as radiation patterns, gain and VSWR are measured in an anechoic chamber using near-field measurement system in TUBITAK. The measured results from the manufactured antennas are compared with the ones that are obtained in simulation to validate the design approach and manufacturing tolerances.

Chapter 6 presents the discussion and conclusion of the presented work. The research contribution of the dissertation is presented.

Chapter 7 presents the limitations of the proposed work and suggestions for future works.

2. BACKGROUND

In this chapter, theory of waveguides and ridged waveguides are presented and critical parameters such as impedance, bandwidth, cut-off frequency, propagating and higher-order modes, and field distribution in waveguides and ridged waveguides are defined.

2.1. WAVEGUIDES

The horn antenna is a type of shaped and flared waveguide, and the most important reason for the deterioration of radiation patterns of horn antennas is the higher-order mode propagation in the waveguides.

Waveguide is a type of transmission line that has an advantage of high-power handling capability and low loss. A representation of rectangular waveguide is shown in Figure 2.1. In this study, we will only focus on the rectangular waveguides because the horn antenna we will design is rectangular.
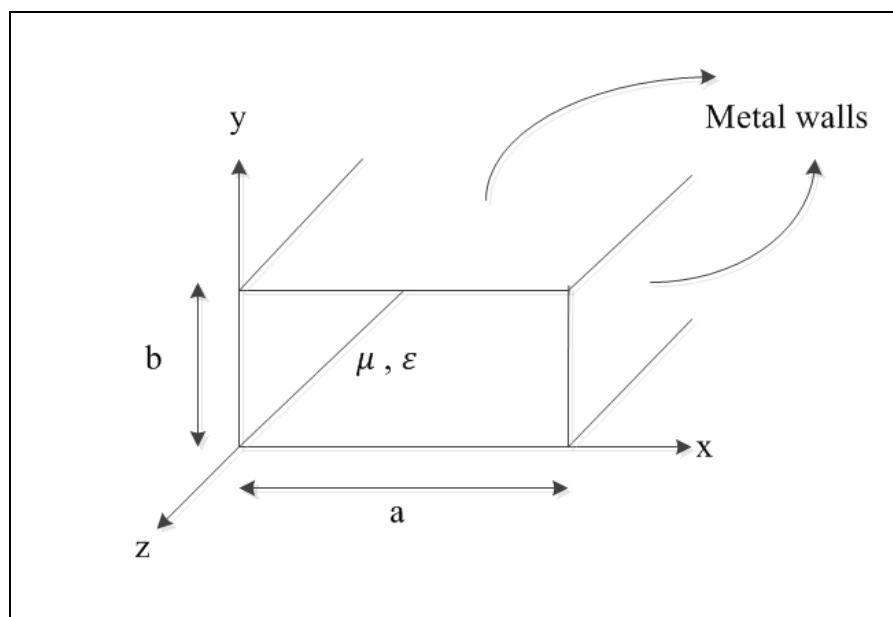
Figure 2.1. Geometry of rectangular waveguide

It is assumed that the waveguide is invariant in the z-direction, and the wave propagates in z as $e^{-j\beta z}$. The solutions of Maxwell's equations that propagate along the guiding direction are found, and the electric and magnetic fields with $e^{j\omega t}$ time-dependence are written as:

$$\vec{E}(x, y, z; t) = \vec{E}(x, y)e^{j\omega t - j\beta z} \tag{2.1}$$

$$\vec{H}(x, y, z; t) = \vec{H}(x, y)e^{j\omega t - j\beta z} \tag{2.2}$$

where, β is the propagation wavenumber along the guide direction, ω is the radial frequency. $\vec{E}(x, y)$ and $\vec{H}(x, y)$ are the transverse electric and magnetic field components, respectively. Maxwell equations in source-free region are given as:

$$\nabla x \vec{E} = -j\omega\mu\vec{H} \tag{2.3}$$

$$\nabla x \vec{H} = j\omega\varepsilon\vec{E} \tag{2.4}$$

x and y components of $\vec{E}$ and $\vec{H}$ can be found as:

$$H_x = \frac{j}{k_c^2}\left(\omega\varepsilon\frac{\partial E_z}{\partial y} - \beta\frac{\partial H_z}{\partial x}\right) \tag{2.5}$$

$$H_y = -\frac{j}{k_c^2}\left(\omega\varepsilon\frac{\partial E_z}{\partial x} + \beta\frac{\partial H_z}{\partial y}\right) \tag{2.6}$$

$$E_x = -\frac{j}{k_c^2}(\beta \frac{\partial E_z}{\partial x} + \omega\mu \frac{\partial H_z}{\partial y}) \tag{2.7}$$

$$E_y = \frac{j}{k_c^2}(-\beta \frac{\partial E_z}{\partial y} + \omega\mu \frac{\partial H_z}{\partial x}) \tag{2.8}$$

$k_c^2 = k^2 - \beta^2$, k_c is the cut-off wave number and $k^2 = \omega^2\mu\varepsilon$ where k is the wavenumber of transverse electromagnetic (TEM) wave in the propagation medium, and ε, μ, represent permittivity and permeability, respectively.

Transverse electric (TE) wave has $E_z = 0$ and $H_z \neq 0$. The first step is to find H_z from the Helmholtz wave equation as given below:

$$(\frac{\partial^2}{\partial x^2} + \frac{\partial^2}{\partial y^2} + \frac{\partial^2}{\partial z^2} + k^2)H_z = 0 \tag{2.9}$$

Note that $H_z(x, y, z) = h_z(x, y)e^{-j\beta z}$ thus (2.9) is reduced to a two-dimensional wave equation for h_z

$$(\frac{\partial^2}{\partial x^2} + \frac{\partial^2}{\partial y^2} + k_c^2)h_z(x, y) = 0 \tag{2.10}$$

Equation (2.10) can be solved using separation of variables method as given below. Let

$$h_z(x, y) = X(x)Y(y) \tag{2.11}$$

By substituting (2.11) into (2.10), the following equation is obtained

$$\frac{1}{X}\frac{d^2 X}{dx^2} + \frac{1}{Y}\frac{d^2 Y}{dy^2} + k_c^2 = 0 \tag{2.12}$$

Then, the general solution can be written as

$$h_z(x,y) = (A\cos k_x x + B\sin k_x x)(C\cos k_y y + D\sin k_y y) \tag{2.13}$$

where, A, B, C and D are arbitrary constants, k_x and k_y are defined separation constants such that

$$k_x^2 + k_y^2 = k_c^2 \tag{2.14}$$

$$\frac{1}{X}\frac{d^2 X}{dx^2} + k_x^2 X = 0 \tag{2.15}$$

$$\frac{1}{Y}\frac{d^2 Y}{dy^2} + k_y^2 Y = 0 \tag{2.16}$$

When the boundary conditions on the electric field components tangential to the waveguide walls are applied, then the following equation is found as

$$H_z(x,y,z) = A_{mn}\cos\frac{m\pi x}{a}\cos\frac{n\pi y}{b}e^{-j\beta z} \tag{2.17}$$

where, A_{mn} is an arbitrary constant, a and b are the width and the height of the waveguide, respectively. Then, the transverse field components of the TE_{mn} can be found using (2.5) - (2.8) and (2.17).

$$E_x = \frac{j\omega\mu n\pi}{k_c^2 b} A_{mn} \cos\frac{m\pi x}{a} \sin\frac{n\pi y}{b} e^{-j\beta z} \tag{2.18}$$

$$E_y = -\frac{j\omega\mu m\pi}{k_c^2 a} A_{mn} \sin\frac{m\pi x}{a} \cos\frac{n\pi y}{b} e^{-j\beta z} \tag{2.19}$$

$$H_x = -\frac{j\beta m\pi}{k_c^2 a} A_{mn} \sin\frac{m\pi x}{a} \cos\frac{n\pi y}{b} e^{-j\beta z} \tag{2.20}$$

$$H_y = \frac{j\beta n\pi}{k_c^2 b} A_{mn} \cos\frac{m\pi x}{a} \sin\frac{n\pi y}{b} e^{-j\beta z} \tag{2.21}$$

The propagation constant is $\beta = \sqrt{k^2 - k_c^2} = \sqrt{k^2 - \left(\frac{m\pi}{a}\right)^2 - \left(\frac{n\pi}{b}\right)^2}$, which is real when $k > k_c$, and corresponds to a propagating mode. Each mode has a combination of m and n, and the cut-off frequency is given as:

$$f_{c_{mn}} = \frac{k_c}{2\pi\sqrt{\mu\varepsilon}} = \frac{1}{2\pi\sqrt{\mu\varepsilon}} \sqrt{\left(\frac{m\pi}{a}\right)^2 - \left(\frac{n\pi}{b}\right)^2} \tag{2.22}$$

The cut-off frequency can clearly be described such that: the field expressions for $\vec{E}$ and $\vec{H}$ are all zero if both *m=n=0*, that means there is no TEM mode ($E_z = H_z = 0$) in hollow metallic waveguides. EM waves will only propagate when the frequency is large enough, and exceeds some lower threshold for rectangular, circular, elliptical or any shaped metallic hollow waveguides. This minimum frequency for wave propagation is called cut-

off frequency. Infinite number of modes can propagate through the waveguide if the operating frequency is higher than the cut-off frequency of the mode. The modes with $f < f_c$ lead to an imaginary β, which means all field components decay exponentially away from the source of excitation. These modes are referred to as cut-off modes, or evanescent modes. If more than one mode is propagating, then the waveguide is called overmoded. The modes that have the same cut-off frequency are called degenerate. Single mode operation is desirable in a waveguide because the total power is distributed among the existing modes in a multimode waveguide operation, and the detection of the total power of multimodes is required. The notation TE$_{mn}$ and TM$_{mn}$ are commonly used to denote the type of wave and its mode, where m and n are the mode number in the horizontal and vertical directions, respectively.

On the other hand, guided EM waves require at least two distinct conductors (transmission lines such as coaxial cable, parallel plate waveguide, microstrip and stripline) to support wave propagation for frequencies 0^+ Hz (TEM mode, no cut-off frequency).

The dominant mode is the one with the lowest frequency or the longest cut-off wavelength, i.e. the mode TE$_{10}$ having m = 1, n=0 for rectangular waveguide. This mode has the following field components and parameters:

$$H_z = A_{10} cos\frac{\pi x}{a} e^{-j\beta z} \tag{2.23}$$

$$E_y = -\frac{j\omega\mu\pi}{\pi} A_{10} sin\frac{\pi x}{a} e^{-j\beta z} \tag{2.24}$$

$$H_x = \frac{j\beta a}{\pi} A_{10} sin\frac{\pi x}{a} e^{-j\beta z} \tag{2.25}$$

$$E_x = E_z = H_y = 0 \tag{2.26}$$

$$k_c = \frac{\pi}{a}, \ \omega_c = \frac{c\pi}{a}, \ f_c = \frac{c}{2a}, \ \lambda_c = 2a, \ \beta_c = \sqrt{k^2 - (\frac{\pi}{a})^2} \tag{2.27}$$

where, λ_c is the cut-off wavelength, ω_c is the cut-off radial frequency. TM modes are characterized by fields with $H_z = 0$, and E_z that must satisfy the following equation

$$(\frac{\partial^2}{\partial x^2} + \frac{\partial^2}{\partial y^2} + k_c^2)e_z(x, y) = 0 \tag{2.28}$$

TE components are found using appropriate boundary conditions by applying same procedure, and the transverse field components of the TM_{mn} are computed as

$$E_x = -\frac{j\beta m\pi}{k_c^2 a} B_{mn} \cos\frac{m\pi x}{a} \sin\frac{n\pi y}{b} e^{-j\beta z} \tag{2.29}$$

$$E_y = -\frac{j\beta n\pi}{k_c^2 b} B_{mn} \sin\frac{m\pi x}{a} \cos\frac{n\pi y}{b} e^{-j\beta z} \tag{2.30}$$

$$H_x = \frac{j\omega\varepsilon n\pi}{k_c^2 b} B_{mn} \sin\frac{m\pi x}{a} \cos\frac{n\pi y}{b} e^{-j\beta z} \tag{2.31}$$

$$H_y = -\frac{j\omega\varepsilon m\pi}{k_c^2 a} B_{mn} \cos\frac{m\pi x}{a} \sin\frac{n\pi y}{b} e^{-j\beta z} \tag{2.32}$$

The cut-off frequencies, the guide wavelength and phase velocity for the TM_{mn} modes are also the same as those of the TE_{mn} modes. If either m or n is zero, then the field expressions for $\vec{E}$ and $\vec{H}$ are zero. Thus, there is no TM_{00}, TM_{01}, or TM_{10} mode, and the lowest order TM mode to propagate (lowest f_c) is the TM_{11} mode.

The interval between the cut-off frequencies or wavelengths of the first two lowest order modes determine the operating bandwidth of single mode operation so that only the lowest mode will propagate. These remarks apply to all waveguide systems, not just hollow conducting waveguides. The comparison of single mode operation in rectangular, circular and elliptical waveguides is given by Kretzschmar [8]. It is clear that the bandwidth of the rectangular waveguide is the highest and is followed by that of the elliptical waveguide. The circular waveguide has nearly half the bandwidth of the elliptical guide. In rectangular waveguides, the operating bandwidth is given in Figure 2.2.
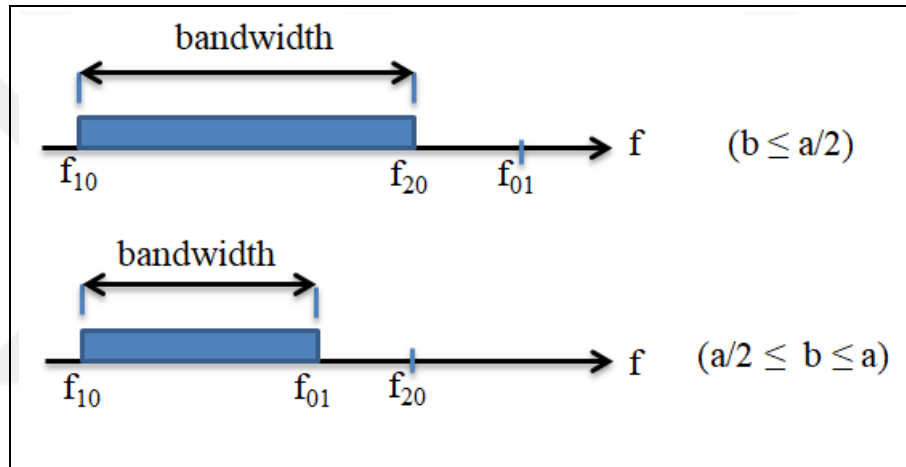
Figure 2.2. The operating BW of rectangular waveguide according to dimensions

In order to make sure that the first mode (TE$_{10}$) is well above cut-off, and the second mode (TE$_{01}$ or TE$_{20}$) is strongly evanescent, a safety margin of about 20 per cent is considered in practical applications.

The wave impedances of TE and TM modes are defined as

$$Z_{TE} = \frac{E_x}{H_y} = \frac{-E_y}{H_x} = \frac{k\eta}{\beta}, \qquad Z_{TM} = \frac{E_x}{H_y} = \frac{-E_y}{H_x} = \frac{\beta\eta}{k} \qquad (2.33)$$

where, $\eta = \sqrt{\mu/\varepsilon}$ is the intrinsic impedance of the material filling the waveguide. A section of rectangular waveguide is modelled in CST Studio Suite. The first eight modes

are excited and their field distributions are analysed to verify the theory explained above. The cut-off frequencies, attenuation and propagation constants corresponding to the modes are calculated. The dimensions of the modelled waveguide are the dimensions of the standard WR-90 waveguide. The model is simulated using the time domain solver between 4.5 − 18 GHz which covers X band, 8 − 12 GHz. E- and H- field monitors are set up to 0.5 GHz intervals from 4.5 GHz to 18 GHz. The schematic view of dominant mode, TE_{10}, of the rectangular waveguide, and the field patterns for the first 8 modes excited in a rectangular waveguide are given in Figure 2.3 and Figure 2.4, respectively.

| (a) Side view, E-field | (c) Top view, E-field | (e) Front view, E-field |
| (b) Side view, H-field | (d) Top view, H-field | (f) Front view, H-field |
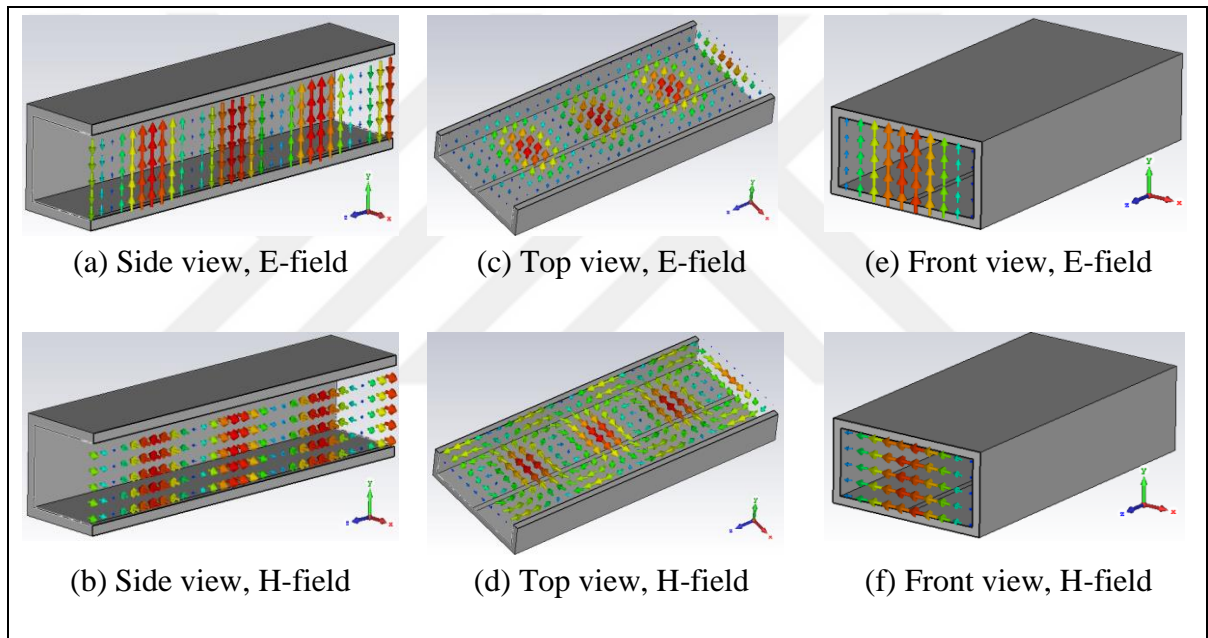
Figure 2.3. The E- and H- field patterns of the dominant mode, TE_{10}, of a rectangular waveguide

The mode information is given in Table 2.1. β and α, are phase and attenuation constants, respectively and they are all frequency dependent parameters that are calculated for each different frequency. The parameters are calculated for the first 8 modes in a rectangular waveguide at the frequency point of 11.25 GHz in Table 2.1.
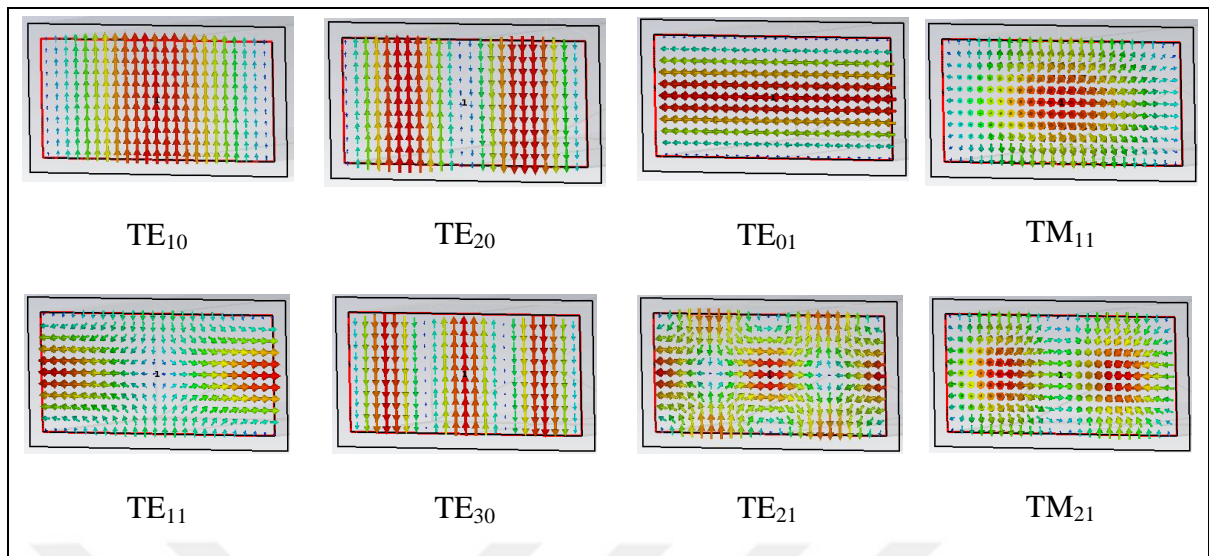
Figure 2.4. Field patterns for the first 8 modes in a rectangular waveguide

Table 2.1. The cut-off frequencies and other parameters of the first 8 modes for modelled X-band rectangular waveguide at 11.25 GHz

Mode	Type	β (1/m)	α (1/m)	Distance (-40dB) (mm)	Cut-off frequency (GHz)	
					Simulation	Calculation
1	TE$_{10}$	191.55	-	-	6.56	6.56
2	TE$_{20}$	-	141.01	32.66	13.11	13.12
3	TE$_{01}$	-	199.72	23.06	14.74	14.76
4	TM$_{11}$	-	241.74	19.05	16.11	16.15
5	TE$_{11}$	-	242.53	18.99	16.14	16.15
6	TE$_{30}$	-	336.81	13.67	19.62	19.68
7	TE$_{21}$	-	339.64	13.56	19.73	19.75
8	TM$_{21}$	-	339.66	13.56	19.73	19.75

It can be noticed that, only dominant mode propagation occurs in the frequency range 8 – 12 GHz with a safety margin below and above this range. It can also be seen that the analytical and simulation cut-off frequency results are close to each other. Note that, there is no real beta at 11.25 GHz for the higher-order modes because those modes are below the

cut-off frequency and the propagation constant becomes entirely imaginary. As these modes do not propagate, the distances at which 40-dB attenuation occurred are calculated (Figure 2.5). TE_{10} mode cannot propagate below cut-off frequency and it attenuates before it reaches the other end of the waveguide.

| 4.5 GHz | 6 GHz | 12 GHz | 18 GHz |
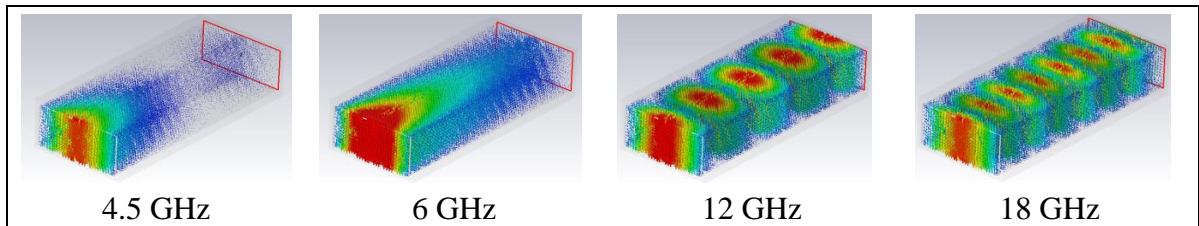
Figure 2.5. TE_{10} mode 3D E-field distribution for different frequencies

The propagation of modes can also be observed by comparing the S_{21} parameters between the 2 ports of the waveguide (Figure 2.6). As can be seen from the Figure 2.6, the wave propagation along the waveguide from port 1 to port 2 is very low before the cut-off frequencies of each mode.
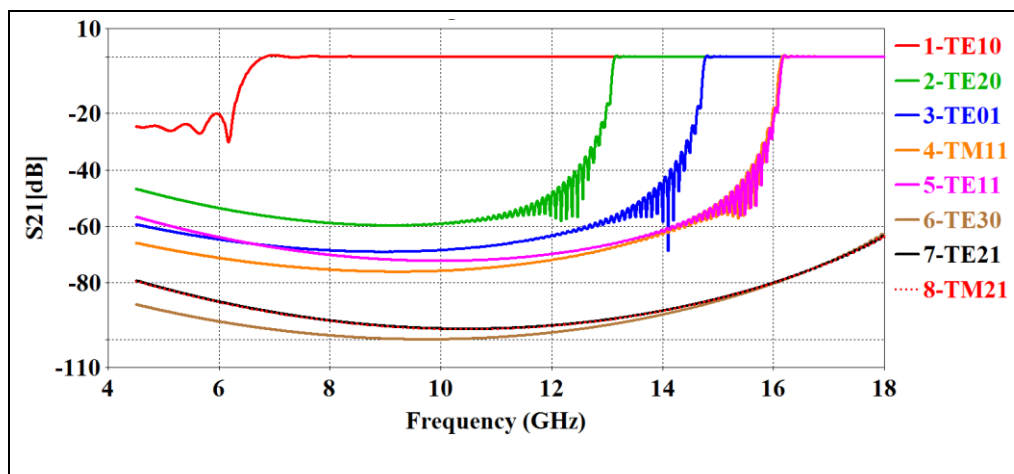
Figure 2.6. The comparison of S_{21} parameters for the first 8 modes in X-band rectangular waveguide

As a result, TE_{10} mode is a single mode operation in the X-band (8 – 12 GHz) that is often preferred in the applications. On the other hand, it is also clear that the bandwidth of the

dominant single mode propagation of the rectangular waveguide is not sufficient in broadband applications where the frequency ratio (f_H:f_L) is greater than 1.5. Detailed analysis about waveguides can also be found in the literature [9], [10], and [11].

2.2. RIDGED WAVEGUIDES

Ridge waveguides have been used in microwave and antenna systems that require wideband operation due to their unique characteristics of low cut-off frequency, wide bandwidth and low impedance. The original ridge waveguide consists of a regular rectangular waveguide, and one or two ridge inserts. Most passive components that may be realized in conventional rectangular waveguides are also available in ridge geometry.

The bandwidth of conventional rectangular waveguide and horn antenna has been improved using the ridges. Ridged waveguides behave as a tapered transmission line, and cause capacitive effects. The cut-off frequency of the ridged waveguide is lower than that of the rectangular waveguide because the cut-off frequency of the transmission line is zero, and the cut-off frequency of the rectangular waveguide depends on its dimensions [12], [13]. The dominant single mode operation in ridged waveguides has also been achieved over the entire frequency band by lowering the cut-off frequency of the fundamental propagating mode. The ridged waveguides are well documented in the literature [14 – 21]. The cut-off frequency equations and impedance curves for ridged waveguides were presented in [16]. Design curves for various aspect ratios were given including the step discontinuity susceptance [12]. The curves of discontinuity susceptance between parallel plate waveguides, and the exact equivalent circuits were obtained in [17]. An algebraic expression was derived to determine the cut-off wavelength of the ridge waveguides in [18]. An approximate determination of the dominant-mode fields was made in ridged waveguides [19] using the eigenvalues given in [16]. An analysis of error effects was carried out by extending the design data given in [16] for ridged rectangular waveguides of any aspect ratios [20]. A complete solution of the ridged waveguide eigenvalue problem was obtained by the formulation of an integral eigenvalue equation which was subsequently solved numerically by applying the Ritz-Galerkin method [21]. Figure 2.7 shows the cross-sectional view of a ridged waveguide and equivalent circuit of a unit length ridged waveguide. The parameter "*a*" is the width of the waveguide, "*b*" is the

waveguide height, "*s*" is the width of the ridge, and "*d*" represents the distance between two opposite ridges.
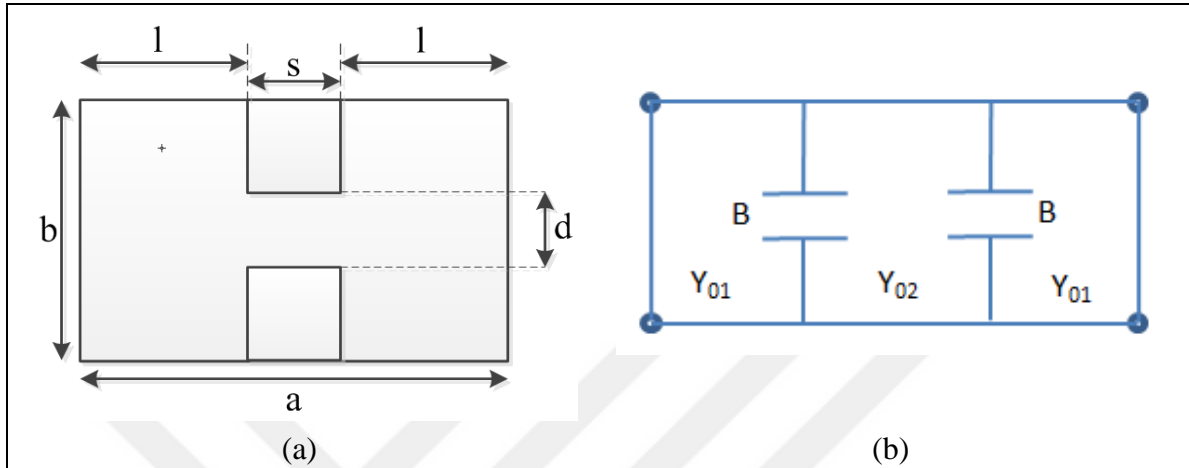
Figure 2.7. Double ridged waveguide (a) Cross-sectional view (b) Equivalent circuit representation

The equations for the cut-off conditions of the various TE_{n0} modes are given as follows [16]:

$$cot\left(\kappa_c \frac{a-s}{2}\right) - \frac{b}{d}tan\left(\kappa_c \frac{s}{2}\right) - \frac{B}{Y_{01}} = 0 \qquad (2.34)$$

$$cot\left(\kappa_c \frac{a-s}{2}\right) + \frac{b}{d}cot\left(\kappa_c \frac{s}{2}\right) - \frac{B}{Y_{01}} = 0 \qquad (2.35)$$

where, κ_c is the propagation constant (cut-off wavenumber) related to the corresponding cut-off wavelength,

$$\kappa_c = \frac{2\pi}{\lambda_c} \qquad (2.36)$$

The value of the normalized susceptance term, B/Y_{01} represents the step discontinuity derived in [19], where Y_{01} and Y_{02} are the characteristic admittances defined as:

$$Y_{01} = \frac{\kappa_c}{\omega\mu}\frac{1}{b} \tag{2.37}$$

$$Y_{02} = \frac{\kappa_c}{\omega\mu}\frac{1}{d} \tag{2.38}$$

The corresponding result for a double ridged waveguide susceptance term is approximated as given in [16], [17]

$$\frac{B}{Y_{01}} \approx 2\left(\frac{b}{a}\right)\left(\frac{a}{\lambda_c}\right)lncosec\left(\frac{\pi d}{2b}\right) \tag{2.39}$$

where, $lncosec\left(\frac{\pi d}{2b}\right)$ can be written as follows and $\alpha = \frac{d}{b}$.

$$lncosec\left(\frac{\pi\alpha}{2}\right) = \left[\frac{\alpha^2+1}{\alpha}cosh^{-1}\left(\frac{\alpha^2+1}{1-\alpha^2}\right) - 2ln\left(\frac{4\alpha}{1-\alpha^2}\right)\right] \tag{2.40}$$

Equation (2.31) applies to TE_{n0} modes where n is odd and (2.32) applies where n is even. The approximate characteristic impedance expression of the ridged waveguides for TE_{n0} modes at infinite frequency is given in [12] and written as

$$Z_{0\infty} = \frac{1}{\sqrt{\frac{\varepsilon\lambda_c}{\mu\pi d}}\left\{\frac{\frac{2d}{\lambda_c}cos^2\left(\frac{\pi a}{\lambda_c}\right)lncosec\left(\frac{\pi d}{2b}\right)+\frac{\pi s}{2\lambda_c}+\frac{1}{4}sin\left(\frac{2\pi s}{\lambda_c}\right)+\cdots}{\frac{d}{b}\frac{cos^2\left(\frac{\pi s}{\lambda_c}\right)}{sin\left(\frac{\pi(a-s)}{\lambda_c}\right)}\left[\frac{\pi(a-s)}{2\lambda_c}-\frac{1}{4}sin\left(\frac{2\pi(a-s)}{\lambda_c}\right)\right]}\right\}} \tag{2.41}$$

where, λ_c/a is calculated for the values b/a, s/a, d/b for the TE_{10} mode using (2.34).

The characteristic impedance at any frequency can be found using the following equation

$$Z_0 = \frac{Z_{0\infty}}{\sqrt{1-\left(\frac{f_c}{f}\right)^2}} \tag{2.42}$$

Furthermore, the graphs given in [12] provide guidance to design double ridged waveguide. The graphs include the extension factors λ_{cn0}/a for the TE_{10}, TE_{20}, TE_{30} modes (Figure 2.8). Additionally, the bandwidth curves of double ridged waveguide were represented as a function of s/a and d/b for the constant aspect ratio b/a=0.5.

(a)   (b)
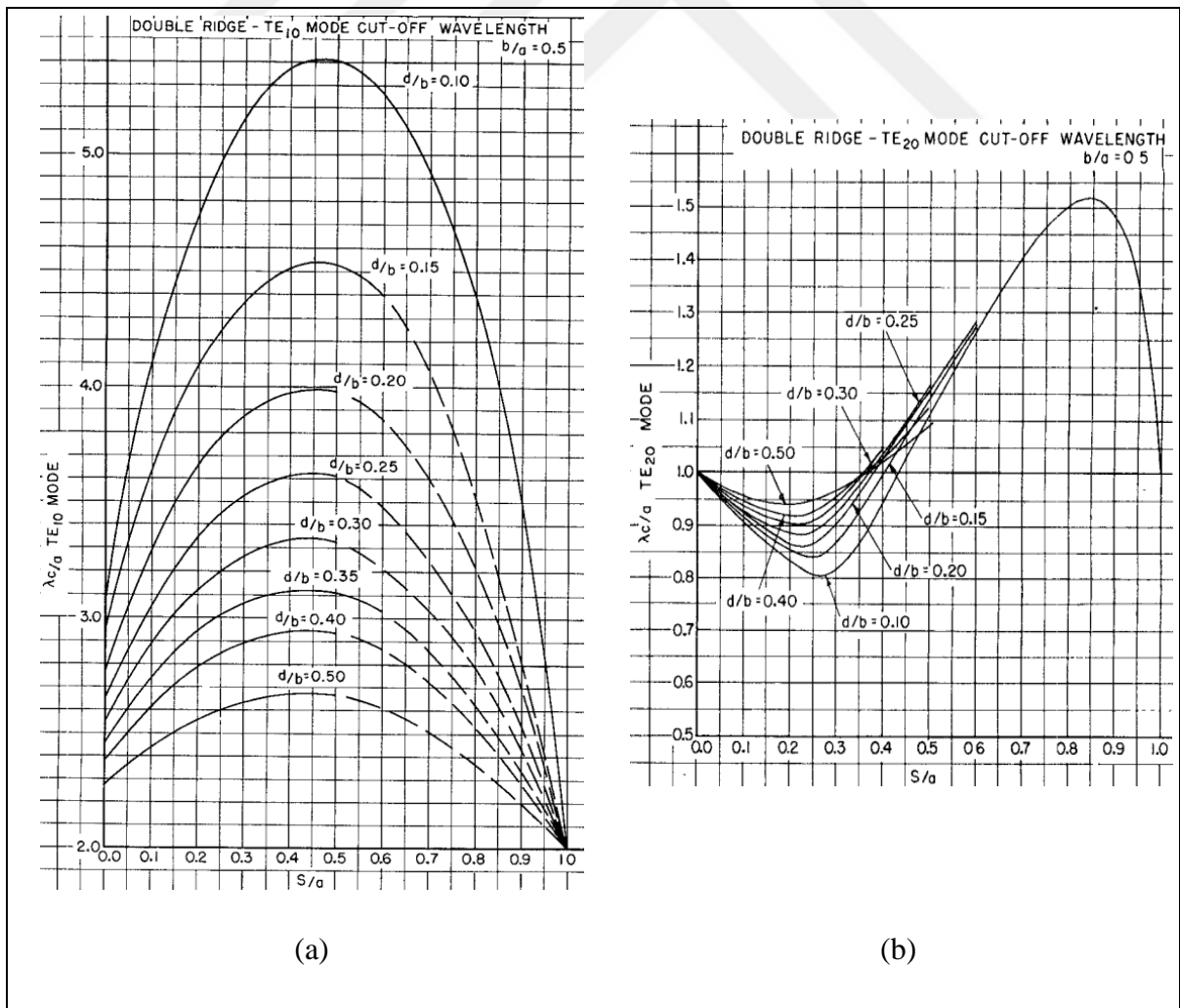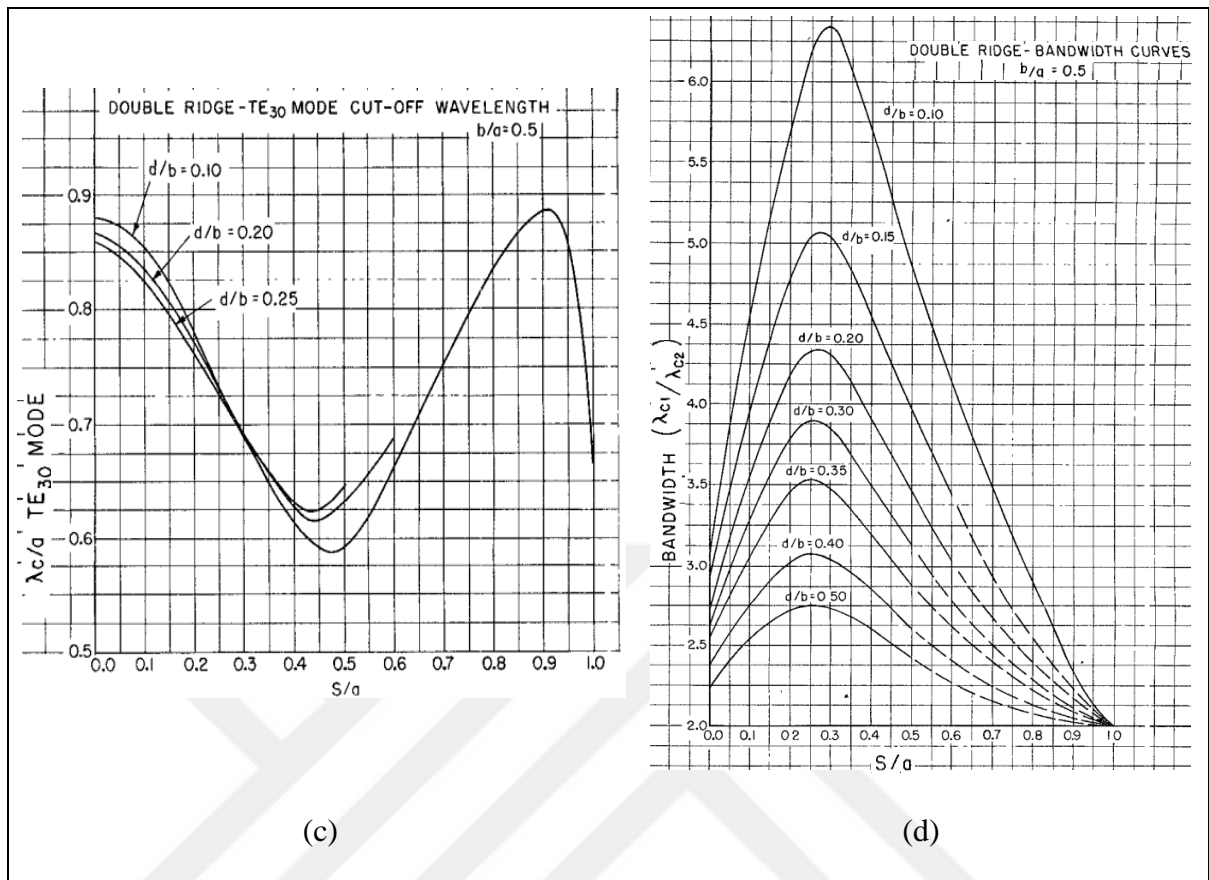
Figure 2.8. λ_c/a for (a) TE$_{10}$ mode, (b) TE$_{20}$ mode, (c) TE$_{30}$ mode, (d) BW curves of double ridged waveguide (copied from [12])

Although it is not necessarily the useful bandwidth, the bandwidth of waveguide is defined as the ratio of the cut-off frequency of the next higher-order mode to that of the dominant mode. The double ridged waveguide (DRW) in the same wall dimensions as the standard waveguide, WR90, and with the same ridge dimensions as WRD500 are compared to see the effect of the ridges in Table 2.2. The theoretical bandwidth ratios of WR-90, DRW are given as 2 and 4.5, respectively.

Besides the cut-off frequency comparison, ridged waveguides with 3 different d/b ratios for 4 different s/a ratio were also analyzed. The cut-off frequencies of the first two modes of DRWs with the same wall dimension as WR90 but with different ridge dimensions are given Table 2.3. As can be seen, the bandwidth results are consistent with the ones given in Figure 2.8-(d). As can be seen from the Table 2.3, the highest bandwidth was provided when the ratio of d/b was low and the s/a ratio was about 0.25.

Table 2.2. The comparison of the cut-off frequencies of the first 8 modes

Mode	Cut-off frequency (GHz)	
	WR-90	**DRW in same wall dimensions as WR-90**
1	6.56	3.29
2	13.11	14.79
3	14.74	14.79
4	16.11	15.47
5	16.14	17.13
6	19.62	22.06
7	19.73	22.06
8	19.73	22.25

Table 2.3. The cut-off frequencies of the first two modes of DRWs with different s/a and d/b ratios

Frequency (GHz)	d/b=0.1	d/b=0.25	d/b=0.5
s/a=0.1	$f_{\text{cut-off}\_1^{\text{st}}\text{mode}}$=3.21 $f_{\text{cut-off}\_2^{\text{nd}}\text{mode}}$=14.38	$f_{\text{cut-off}\_1^{\text{st}}\text{mode}}$=4.36 $f_{\text{cut-off}\_2^{\text{nd}}\text{mode}}$=14.11	$f_{\text{cut-off}\_1^{\text{st}}\text{mode}}$=5.47 $f_{\text{cut-off}\_2^{\text{nd}}\text{mode}}$=13.72
s/a=0.25	$f_{\text{cut-off}\_1^{\text{st}}\text{mode}}$=2.64 $f_{\text{cut-off}\_2^{\text{nd}}\text{mode}}$=14.76	$f_{\text{cut-off}\_1^{\text{st}}\text{mode}}$=2.43 $f_{\text{cut-off}\_2^{\text{nd}}\text{mode}}$=11.82	$f_{\text{cut-off}\_1^{\text{st}}\text{mode}}$=2.80 $f_{\text{cut-off}\_2^{\text{nd}}\text{mode}}$=8.96
s/a=0.5	$f_{\text{cut-off}\_1^{\text{st}}\text{mode}}$=3.84 $f_{\text{cut-off}\_2^{\text{nd}}\text{mode}}$=14.89	$f_{\text{cut-off}\_1^{\text{st}}\text{mode}}$=3.66 $f_{\text{cut-off}\_2^{\text{nd}}\text{mode}}$=11.62	$f_{\text{cut-off}\_1^{\text{st}}\text{mode}}$=4.12 $f_{\text{cut-off}\_2^{\text{nd}}\text{mode}}$=9.76
s/a=0.75	$f_{\text{cut-off}\_1^{\text{st}}\text{mode}}$=5.10 $f_{\text{cut-off}\_2^{\text{nd}}\text{mode}}$=13.97	$f_{\text{cut-off}\_1^{\text{st}}\text{mode}}$=4.95 $f_{\text{cut-off}\_2^{\text{nd}}\text{mode}}$=12.08	$f_{\text{cut-off}\_1^{\text{st}}\text{mode}}$=5.35 $f_{\text{cut-off}\_2^{\text{nd}}\text{mode}}$=11.14

We carry out the design of the waveguide according to the analysis using the figures (Figure 2.7, Figure 2.8), tables (Table 2.2-Table 2.3) and equations (2.34) − (2.42). The dimensions of the ridged waveguide were determined as a=19 mm, b=8 mm, s=5.3 mm, and d=1.2 mm. The simulation model was presented in Figure 2.9. The first 5 modes of the double ridged waveguide were calculated, and the related parameters were given in Table 2.4. It was observed that only dominant mode propagation occurred in the frequency range

4.5 – 18 GHz, in where the dimensions were appropriate for antenna to be designed in the following chapters of this dissertation. The double ridged waveguide design is directly related with the realization of the wideband horn antenna.
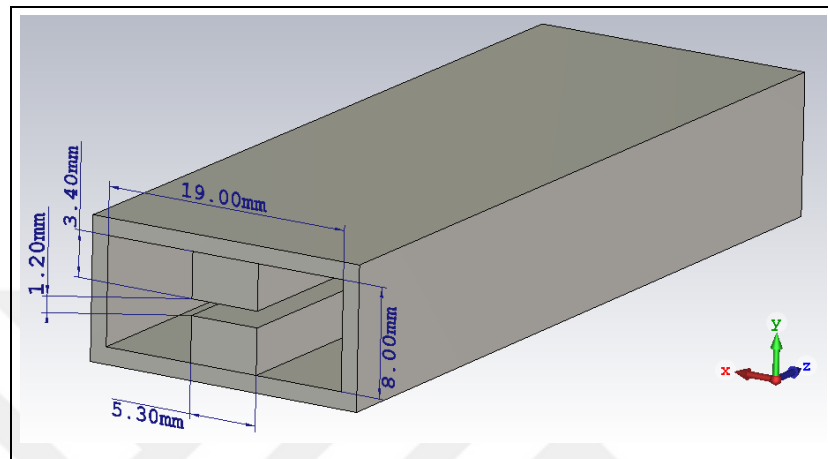
Figure 2.9. The dimensions of the modelled double ridged waveguide

Table 2.4. The cut-off frequencies and other parameters of the first 5 modes for modelled DRW at 11.25 GHz

Mode	β (1/m)	α (1/m)	Distance (-40dB) (mm)	Cut-off frequency (GHz)
1	222.64	-	-	3.70
2	-	315.31	14.61	18.79
3	-	315.60	14.60	18.79
4	-	315.32	14.60	18.79
5	-	401.20	11.48	22.20

Figure 2.10 shows the electric field pattern for the first mode of the DRW, TE_{10} mode. 3D E-field distributions of TE_{10} mode for different frequencies are given in Figure 2.11. The propagation and attenuation of modes can also be observed by comparing the S_{21} parameters between the 2 ports of the waveguide. It could be noticed that TE_{10} mode was only propagating wave along the frequency band 4.5 GHz – 18 GHz (Figure 2.12).
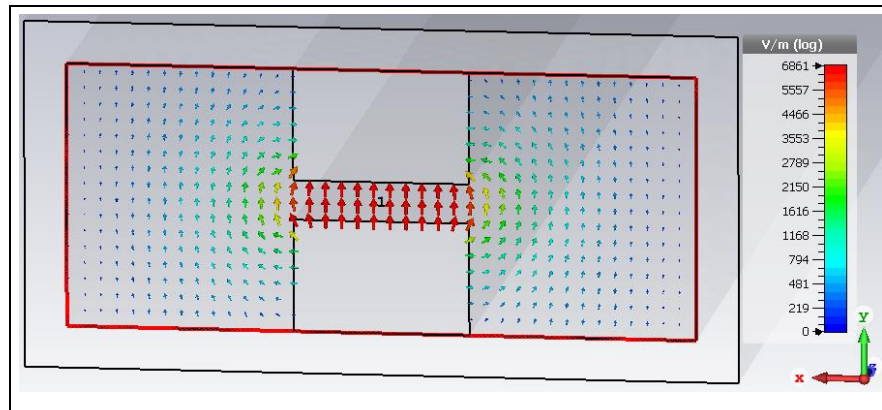
Figure 2.10. TE$_{10}$ mode E-field pattern

4.5 GHz

6 GHz

12 GHz

18 GHz
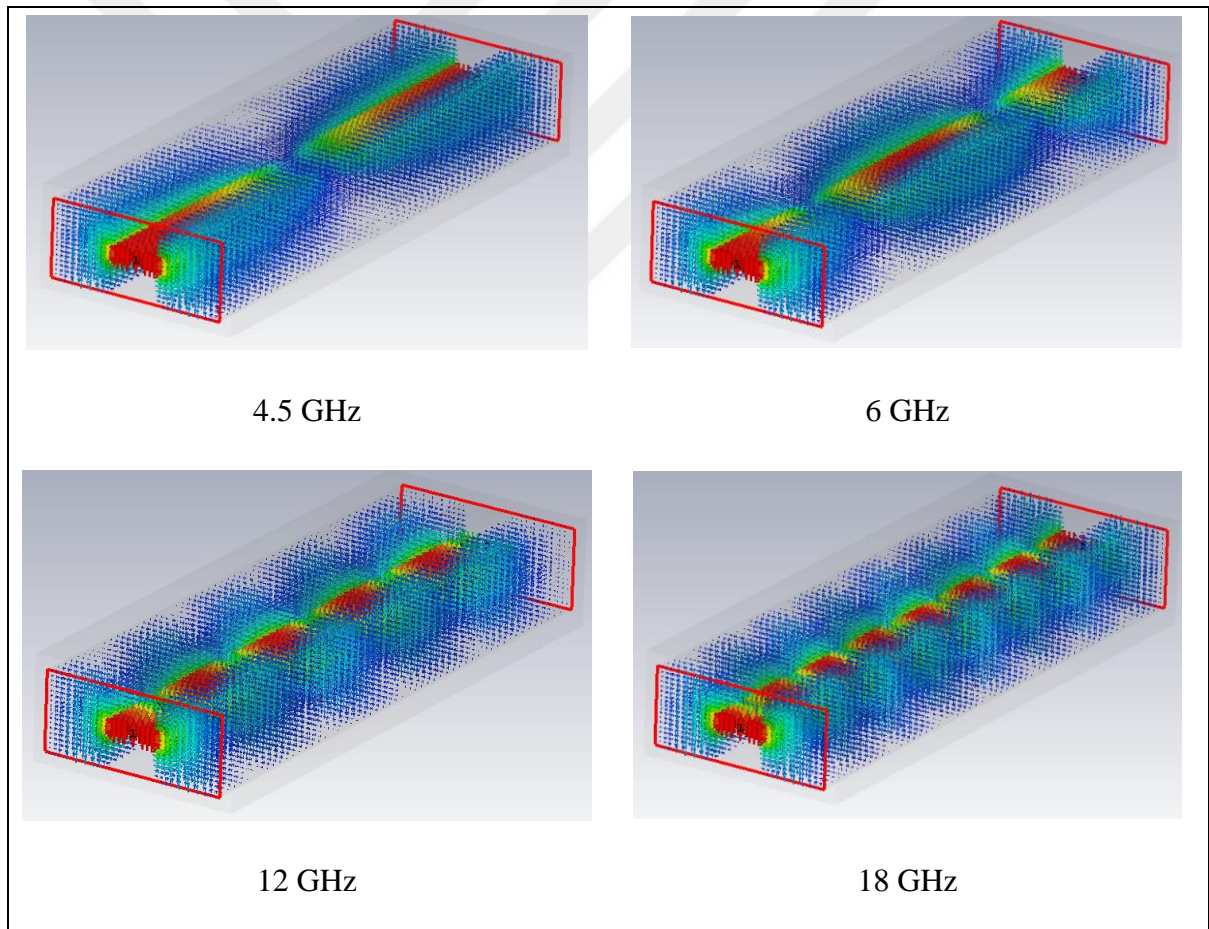
Figure 2.11. TE$_{10}$ mode 3D E-field distribution for different frequencies
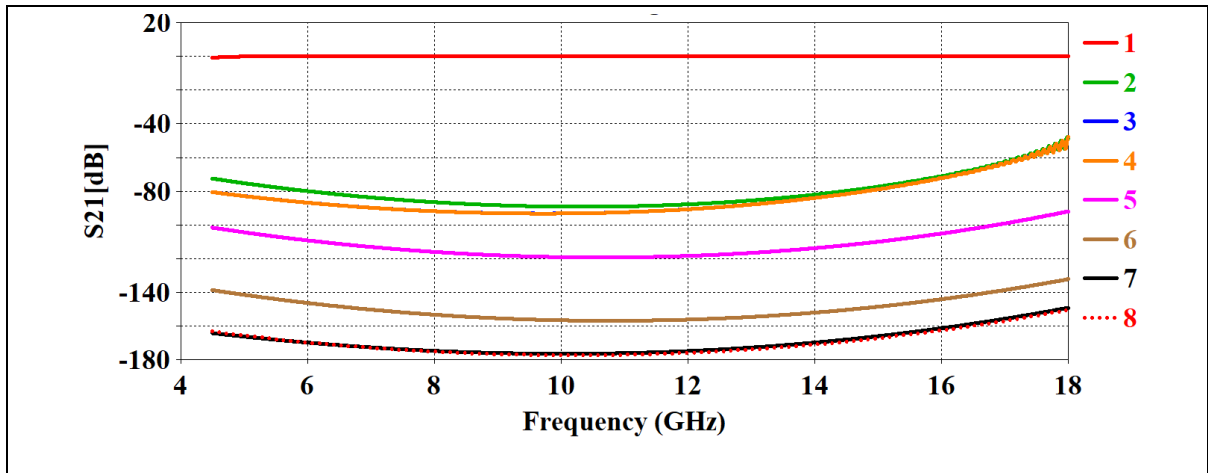
Figure 2.12. The comparison of S_{21} parameters for the first 8 modes in designed double ridged waveguide

3. HORN ANTENNA DESIGNS

In this chapter, the design details of the SGHA and DRHA are given. The design procedures are explained and the antennas are modelled and analysed. The bandwidths of the antennas, the frequency-dependent beamwidth variation and the interaction of the antenna radiation pattern with the bandwidth are also examined in detail. In this study, we first design the SGHA as an example to understand the characteristics of horn antennas, and then we utilize it as a reference to study the variation of beamwidth of horns along the operating frequency band. Since the desired wideband property is in the order of minimum f_{max}:f_{min} ratio 4:1, the DRHA is designed to extend the operating frequency band by adopting the ridges in the waveguides to horns.

3.1. X-BAND STANDARD GAIN HORN ANTENNA

Horns are generally the most widely used microwave antennas because of they are high gain, ease-to-construct, moderate bandwidth, and highly accurate radiating devices with low VSWR. The most common type of horn used as a standard gain horn is the pyramidal horn (Figure 3.1).

The aperture dimensions (A, B) and flare length (L_{flare}) that provide the desired gain and half power beamwidths for a given operating frequency need to be determined during the design of SGHA. It should be noted that SGHA does not consist of waveguide to coaxial matching section. Ideal waveguide port was used to excite waves in both design and simulation model. Since the dimensions of the standard waveguide WR90 in waveguide section of SGHA are preferred, it is possible to use the commercially available waveguide-coaxial adapters that suitable for antenna waveguide sections.
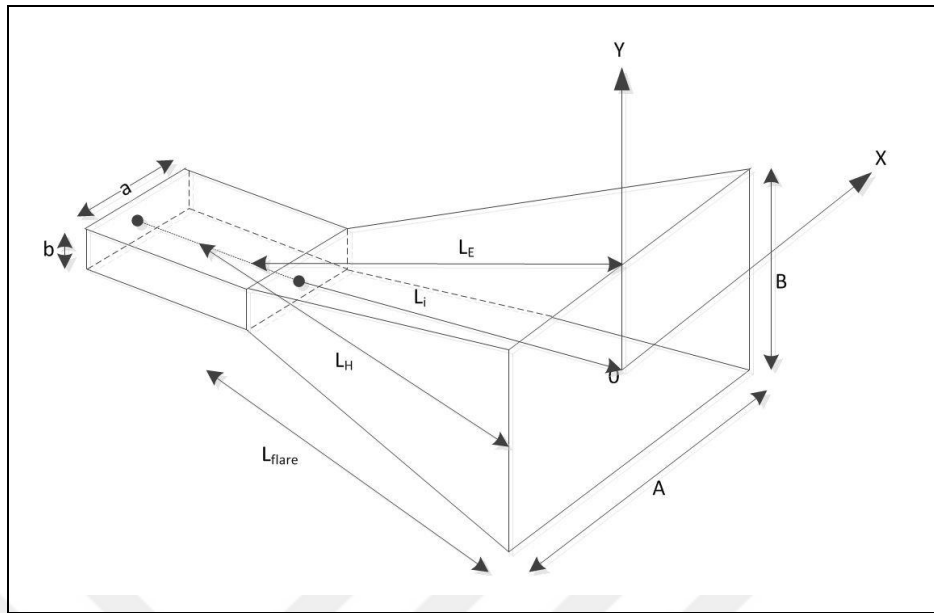
Figure 3.1. Geometry of a pyramidal horn

The theoretical background of SGHA design was studied previously, and X-band SGHA covering 8 − 12 GHz was modelled and analysed. Different analytical design techniques were presented in [22 − 28]. It is possible to use any of these analytical design techniques, and the key specifications for target application are bandwidth and HPBW parameters.

The most important differences between design procedures arise from the accuracy of the antenna gain formula, and either exact phase errors are taken into consideration [26] or taken as constant values. The longer path length from the waveguide to the edge of the horn aperture (L_E and L_H in Figure 3.1) compared to the aperture center in the flare plane (L_i in Figure 3.1) introduces a phase delay across the aperture which causes phase errors. In fact, the exact phase errors are dependent on the desired gain, dimensions of the waveguide, and the operating frequency. However, if the following conditions are met, then the variations of the waveguide dimensions and frequency become negligible in phase error calculations:

$$2 \le a/b \le 2.5 \qquad\qquad (3.1)$$

$$1 < \lambda/a < 1.7 \qquad\qquad (3.2)$$

Additionally, there are design methods based on empirical measurements that also give accurate results [29]. Minor variations in antenna size due to differences in design techniques may be ignored for our design as these variations can create differences that will not affect the beamwidth variation along the operating frequency band of the antenna. The aperture dimension values found by analytical design method were also confirmed by CST.

A pyramidal horn can be considered as a combination of E-plane sectoral, and H-plane sectoral horns where both dimensions of the input waveguide are broadened along the flare section. Therefore, the transverse fields and the radiation pattern can be directly obtained from the propagating fields and radiation patterns of sectoral E- and H- plane horns. The directivity can also be expressed as a combination of directivities of sectoral horns as:

$$G = \frac{\pi}{32}\left(\frac{\lambda}{a}D_E\right)\left(\frac{\lambda}{b}D_H\right) = \frac{4\pi}{\lambda^2}\varepsilon_{ap}A \qquad (3.3)$$

$$D_E = \frac{a}{\lambda}\frac{32}{\pi}\frac{B}{\lambda}K_E \qquad (3.4)$$

$$D_H = \frac{b}{\lambda}\frac{32}{\pi}\frac{A}{\lambda}K_H \qquad (3.5)$$

where, G is the boresight gain, D_E and D_H are the gains of E- and H- plane sectoral horns respectively, K_E and K_H are the parameters related with aperture efficiency contributions, and ε_{ap} is the aperture efficiency, which is a measure of how efficiently the antenna physical area is utilized. Since the radiation efficiency is close to unity for horn antennas, ε_{ap} can be defined as the composition of the aperture taper efficiency, ε_t, and phase error efficiency, ε_{ph} as follows:

$$\varepsilon_{ap} = \varepsilon_t\varepsilon_{ph} = \varepsilon_t\varepsilon_{ph}^E\varepsilon_{ph}^E \qquad (3.6)$$

$$K_E = \varepsilon_{ph}^E = \frac{C^2(q)+S^2(q)}{q^2} \tag{3.7}$$

$$K_H = \varepsilon_{ph}^H = \frac{\pi^2}{64t}\{[C(p_1) - C(p_2)]^2 + [S(p_1) - S(p_2)]^2\} \tag{3.8}$$

where,

$$q = 2\sqrt{s} \tag{3.9}$$

$$p_1 = 2\sqrt{t}\left(1 + \frac{1}{8t}\right), p_2 = 2\sqrt{t}\left(-1 + \frac{1}{8t}\right) \tag{3.10}$$

where $C(\ )$ and $S(\ )$ are Fresnel integrals. s and t are phase error parameters defined in the E- and H- plane respectively as

$$t = \frac{A^2}{8\lambda R_1} \tag{3.11}$$

$$s = \frac{B^2}{8\lambda R_2} \tag{3.12}$$

where, R_1 and R_2 dimensions that are shown in Figure 3.2 and Figure 3.3. The equations from (3.3) to (3.10) were derived using relations derived by Schelkunoff [30].
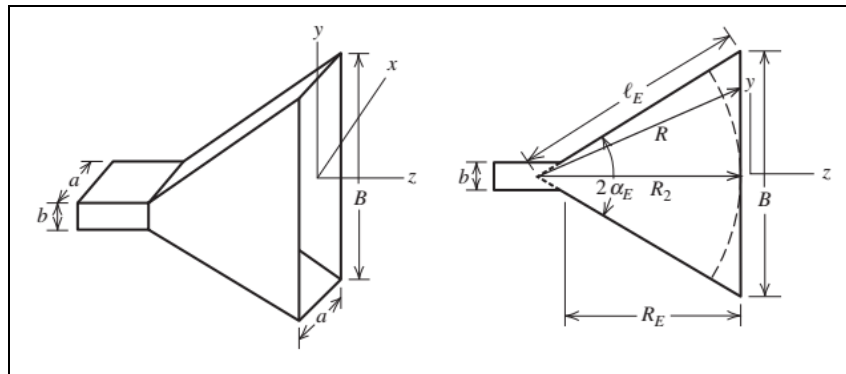
Figure 3.2. E-plane horn geometry (copied from [24])
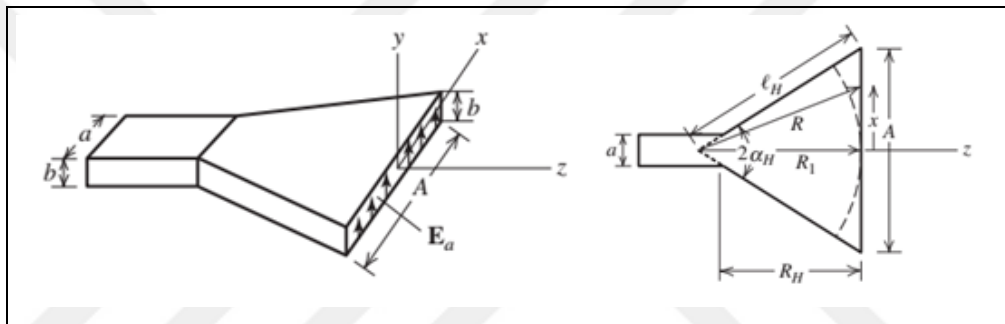
Figure 3.3. H-plane horn geometry (copied from [24])

The aperture efficiency for optimum sectoral horns with phase error parameters s=0.25 and t=0.375 was $\varepsilon_{ap} = 0.51$. Optimum aperture dimensions of the horn are given in the following equations using universal curves shown in Figure 3.4 for E- and H- plane sectoral horns. It can be seen that for a given axial length R_1 and R_2, there is an optimum aperture width, A, and optimum aperture height, B, corresponding to the peak of the appropriate curves for H- and E- plane sectoral horns, respectively. The values of A/λ corresponding to optimum operation plotted versus R_1/λ produce a smooth curve with the equation $A/\lambda = \sqrt{3R_1/\lambda}$ that results in an equation for the aperture width of the horn as follows

$$A = \sqrt{3\lambda R_1} \tag{3.13}$$

A curve corresponding to pairs of values of B/λ and R_2/λ for optimum conditions yields for the height of the aperture as

$$B = \sqrt{2\lambda R_2} \tag{3.14}$$
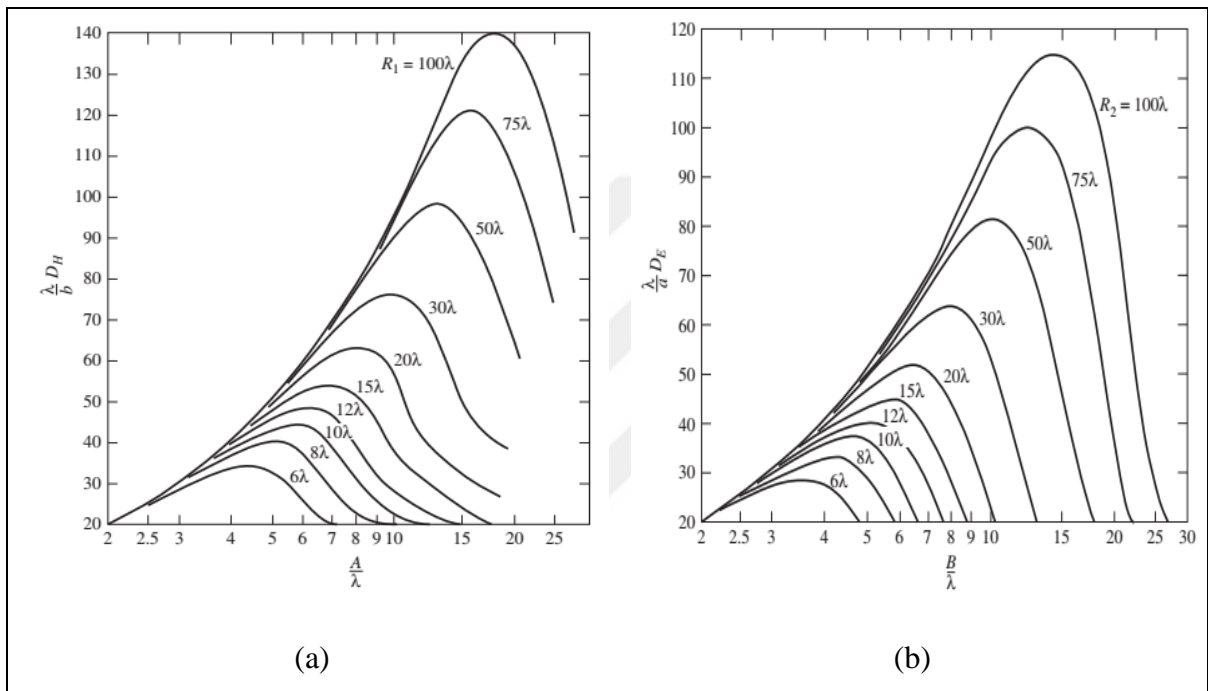
Figure 3.4. Universal directivity curves for (a) H- and (b) E-plane sectoral horns [24]

Later, we derived the design equation that provides the determination of dimensions of the horn antenna. Equation (3.15) is a *pyramidal horn design equation* obtained by observing the phase error conditions on the E- and H- planes according to the optimum gain requirement, and taking into consideration the conditions that will enable the antenna geometry to be physically feasible. The derivation of (3.15) can be found in [24], [31].

$$A^4 - aA^3 + \frac{3bG\lambda^2}{8\pi\varepsilon_{ap}}A = \frac{3G^2\lambda^4}{32\pi^2\varepsilon_{ap}^2} \tag{3.15}$$

It is possible to solve (3.15) by trial and error assuming a value as:

$$A = 0.45\lambda\sqrt{G} \tag{3.16}$$

Hence, the steps for the optimum SGHA design can be summarized as the follows:

i.   Specify the waveguide dimensions for a given operating frequency (or wavelength), and the desired gain.

ii. Solve the pyramidal design equation (3.15) for A using $\varepsilon_{ap} = 0.51$.

iii. Obtain the dimensions A, B, R_1, R_2, R_H, R_E using (3.3), (3.13), (3.14) and the similar-triangle property.

iv. Determine the solution accuracy of the results by checking whether the axis lengths, R_H and R_E, are equal and by using (3.11), (3.12), to see t=0.375 and s=0.25.

The H-plane (azimuth) and E-plane (elevation) HPBWs for optimum performance can be determined from the universal radiation patterns of an H- and E- plane sectoral horns for t=0.375 and s=0.25 using Figure 3.5.

The 3-dB points for H- and E-planes are $\left(\frac{A}{\lambda}\right)sin\theta_H = 0.68$ and $\left(\frac{B}{\lambda}\right)sin\theta_E = 0.47$ for optimum values of t and s, respectively. Thus, the HPBW relationships for optimum SGHA are found using the below equations for $A \gg \lambda$ and $B \gg \lambda$.

$$HPBW_H = 2\arcsin\left(\frac{0.68}{\frac{A}{\lambda}}\right) \approx 1.36\frac{\lambda}{A} = 78°\frac{\lambda}{A} \tag{3.17}$$

$$HPBW_E = 2\arcsin\left(\frac{0.47}{\frac{B}{\lambda}}\right) \approx 0.94\frac{\lambda}{B} = 54°\frac{\lambda}{B} \tag{3.18}$$
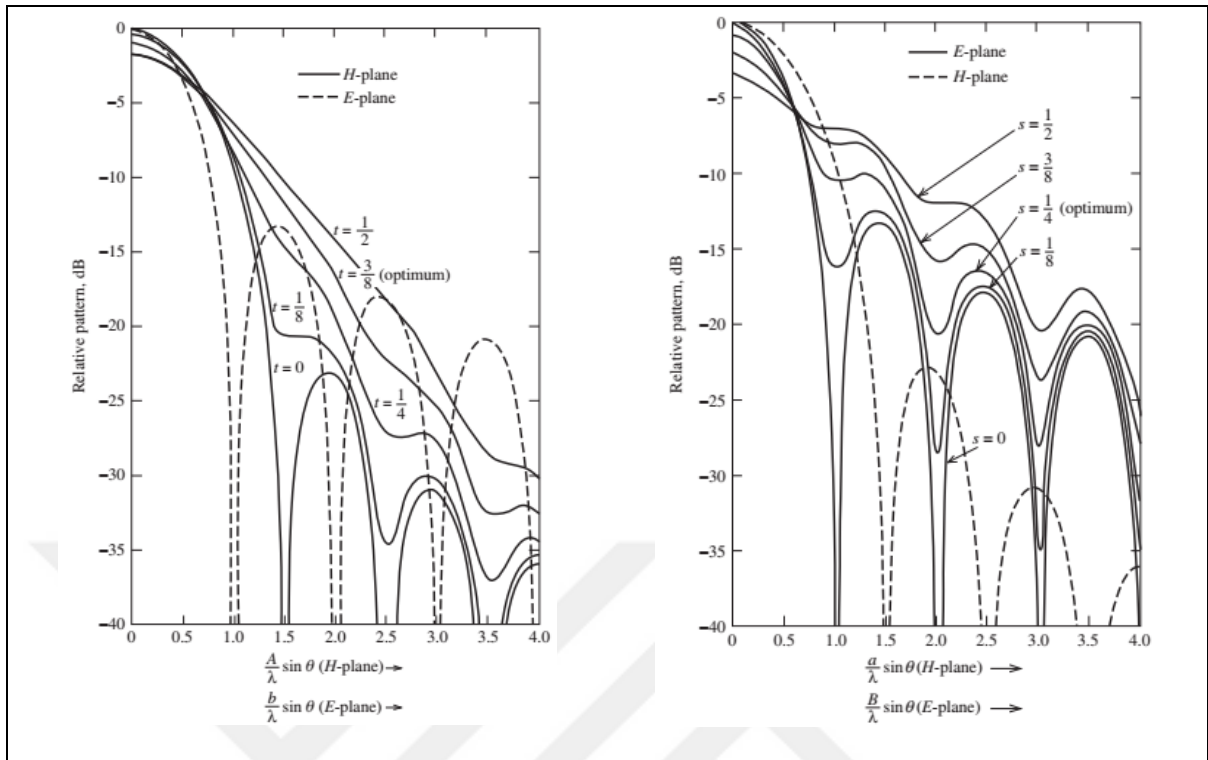
Figure 3.5. Universal radiation patterns for the principal planes of H- and E- plane sectoral horns [24]

There is a design method in which all the dimensions of the antenna are given by equations without the need to solve quadratic equation (3.15). The details of the design procedure are given in [22], [32], [33] and the equations are presented according to notations given in Figure 3.2 and Figure 3.3 below

$$G_{linear} = 10^{G_{dB}/10} \tag{3.19}$$

$$A = 0.096 a G_{linear}{}^{0.232} + 0.42 \lambda G_{linear}{}^{0.503} - 0.193 b \tag{3.20}$$

$$l_H = A \sqrt{\frac{1}{4} + \left(\frac{A}{3\lambda}\right)^2} \tag{3.21}$$

$$R_H = (A - a)\sqrt{-\frac{1}{4} + \left(\frac{l_H}{A}\right)^2} \qquad (3.22)$$

$$R_1 = \sqrt{l_H^2 - \left(\frac{A}{2}\right)^2} \qquad (3.23)$$

$$B = \frac{1}{2}\left[b + \sqrt{b^2 + 8R_H\lambda}\right] \qquad (3.24)$$

$$l_E = \frac{B}{2}\sqrt{1 + \left(\frac{B}{\lambda}\right)^2} \qquad (3.25)$$

$$R_E = (B - b)\sqrt{-\frac{1}{4} + \left(\frac{l_E}{B}\right)^2} \qquad (3.26)$$

$$R_1 = \sqrt{l_E^2 - \left(\frac{B}{2}\right)^2} \qquad (3.27)$$

Since the latter design method including equations (3.19) to (3.27) is more straightforward, this technique is used to design X-band SGHA with 15 dBi gain at center frequency, 10 GHz. It should be noted that although horn antennas operate over a bandwidth of 1.5:1, since the aperture efficiency decreases with frequency due to increasing phase errors, the performance is optimum only at the design frequency. The aperture radiated fields and pattern equations of the horn antenna can also be found in [9].

The dimensions of the proposed SGHA are calculated using the equations (3.19) – (3.27) and the antenna is first modelled in the CST program. The various angled views of the modelled antenna are shown in Figure 3.6.
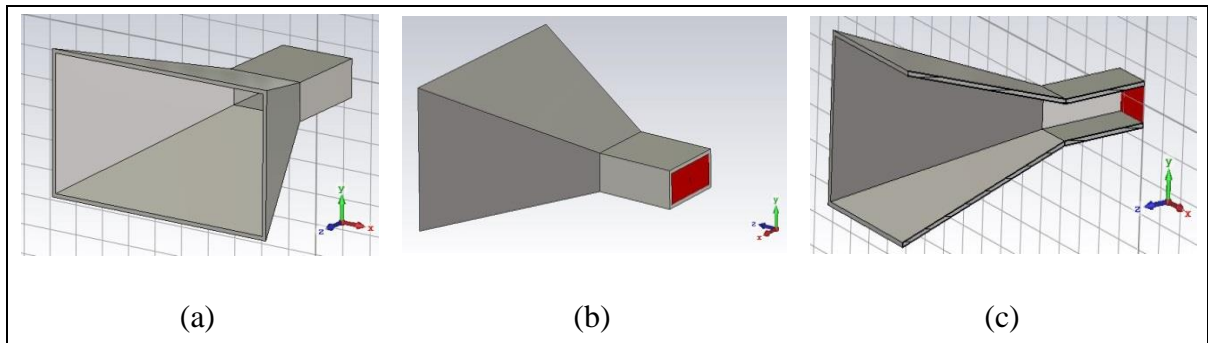
Figure 3.6. Different views of modelled X-band SGHA

Note that the waveguide section of modelled SGHA were analysed in Chapter 2, and the same waveguide, WR-90 was also used here. Thus, the propagating modes were evaluated and their field distributions were determined in Chapter 2. Only dominant mode propagation occurs in the frequency range 8 − 12 GHz with a safety margin below and above this range.

The dimensions were calculated as aperture width=74.5 mm, aperture height=56 mm and flare length=42.8 mm using the equations from (3.19) to (3.27). On the other hand, it was noticed after the first simulation that it was possible to make an antenna design that performed better on other parameters such as VSWR and SLL, while abandoning a small amount of gain with some changes on the initial values. The compared results are shown in Figure 3.7 and Figure 3.8.
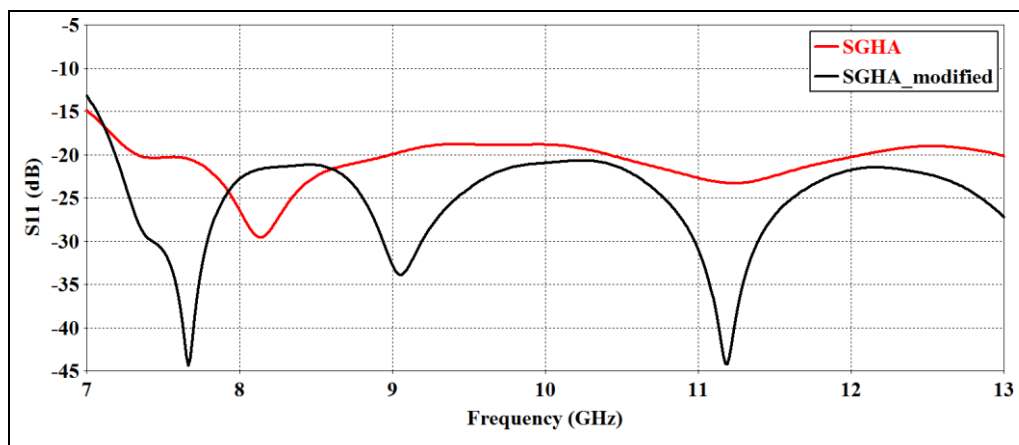
Figure 3.7. The return loss (S_{11}) comparison of SGHA and modified SGHA
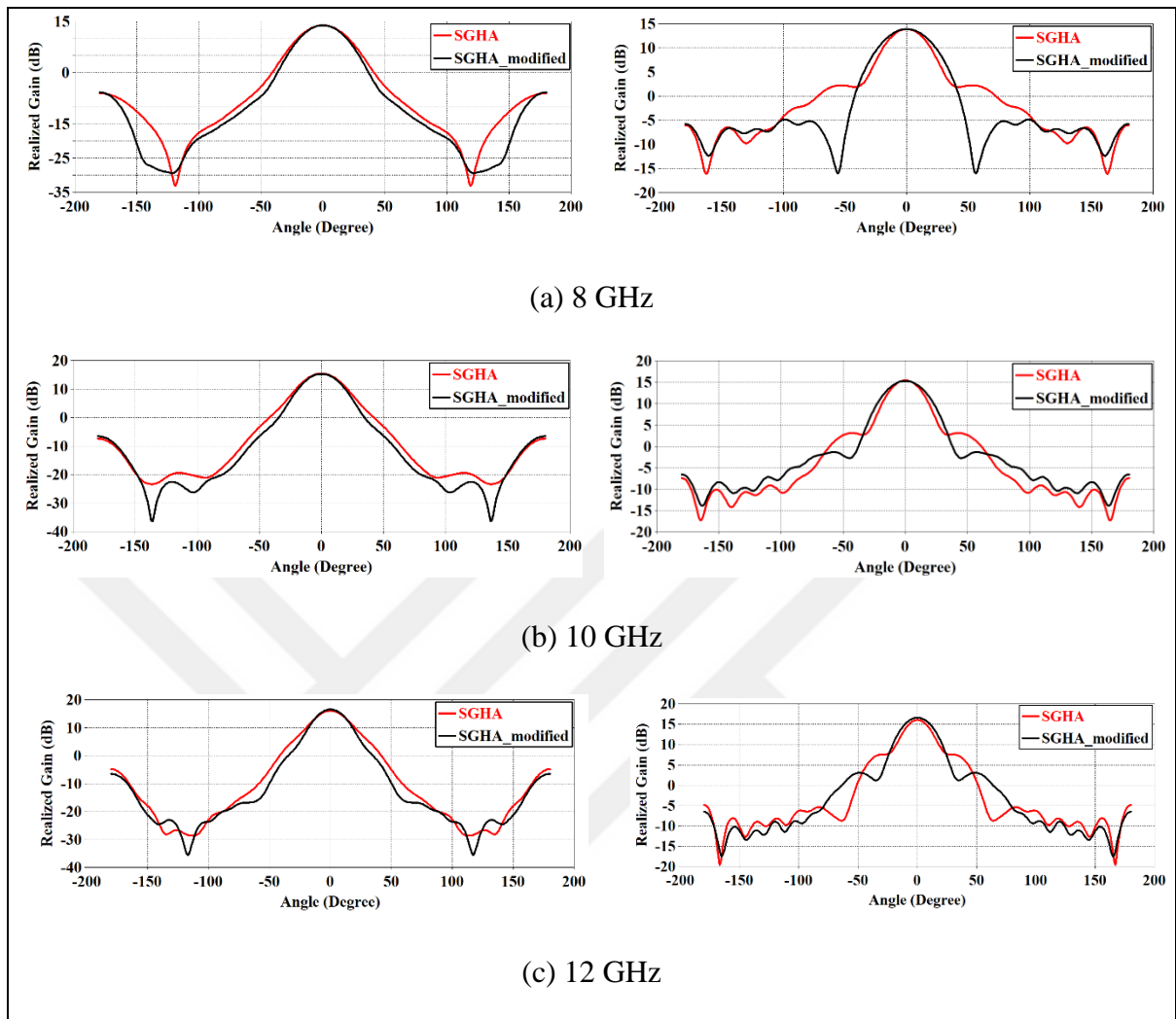
Figure 3.8. The comparison of azimuth and elevation patterns of SGHA and modified
SGHA at (a) 8 GHz (b) 10 GHz (c) 12 GHz

As it can be obviously seen from Figure 3.7 and Figure 3.8, we decided to continue this study with the modified SGHA design because especially side-lobe levels (SLLs) of elevation patterns and S_{11} have better performance. The model was simulated using the time domain solver between $4.5 - 18$ GHz that covers X band, $8 - 12$ GHz. The characteristics of the designed antenna according to the simulation results are given in Table 3.1.

Table 3.1. The specifications of the modified SGHA

Frequency band (GHz)	8 - 12
Polarization	Linear (Vertical)
Gain (dBi)	13.9 – 16.6
HPBW (Azimuth) (Degree)	33.6 – 24.2
HPBW (Elevation) (Degree)	41.2 – 28.7
Aperture Dimensions (Flare Length x Width x Height) (mm)	60 x 75 x 45

The propagation of modes can be observed by comparing the S_{11} parameters corresponding to each mode. The result is presented in Figure 3.9. Since the wave propagation along the waveguide from port is very low before the cut-off frequencies of each mode, return loss levels are also very poor. The places where the curves peak are the points corresponding to the cut-off frequency of the relevant mode. The 3D far-field radiation patterns according to simulation results were given in Figure 3.10.
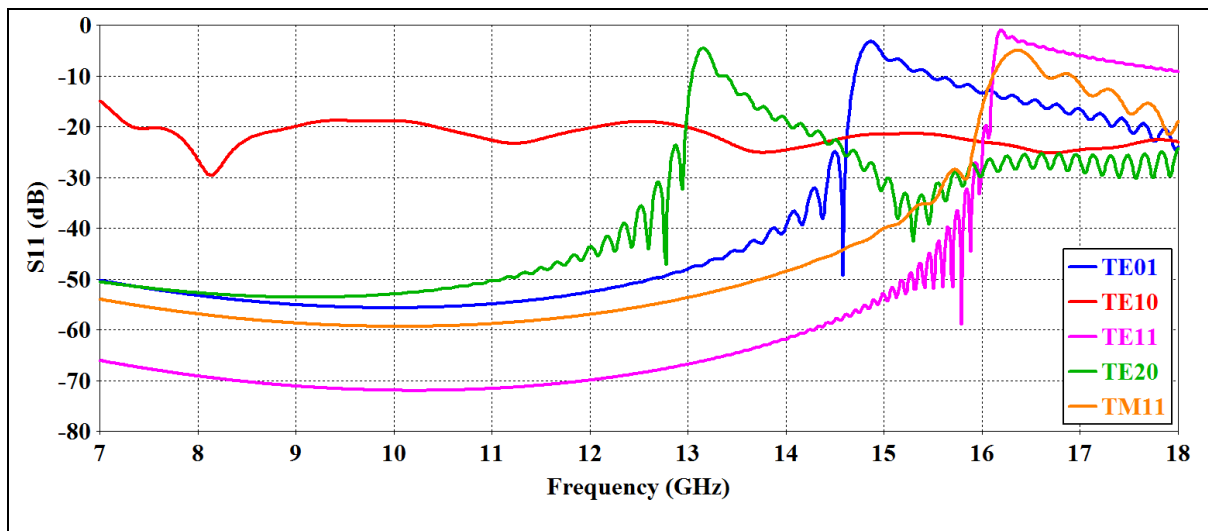
Figure 3.9. The comparison of S_{11} parameters for the first 5 modes in SGHA

(a) 8 GHz   (b) 10 GHz   (c) 12 GHz
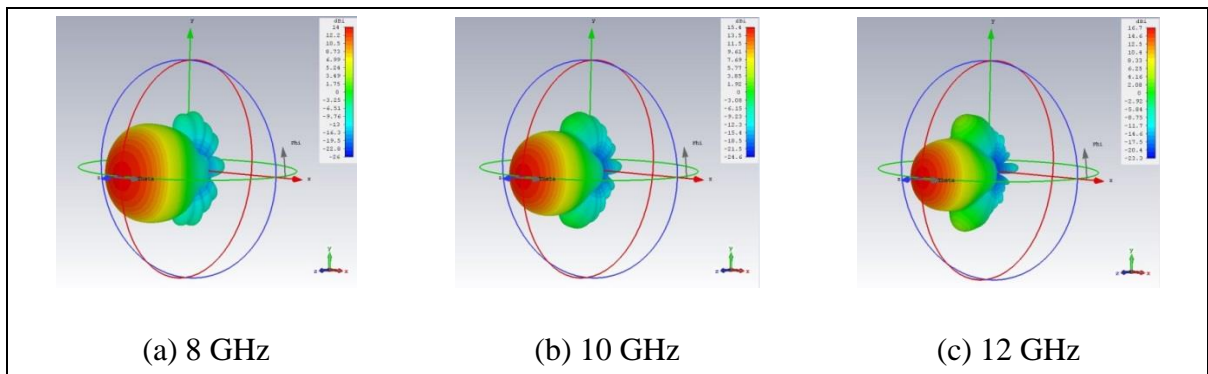
Figure 3.10. 3D far-field radiation patterns of the designed SGHA

In order to see the deteriorating effect when multiple modes are excited, it is necessary to examine the radiation patterns obtained at the frequency of 18 GHz where 5 modes are propagated.

(a) Mode 1   (b) Mode 2   (c) Mode 3

(d) Mode 4   (e) Mode 5   (f) All modes
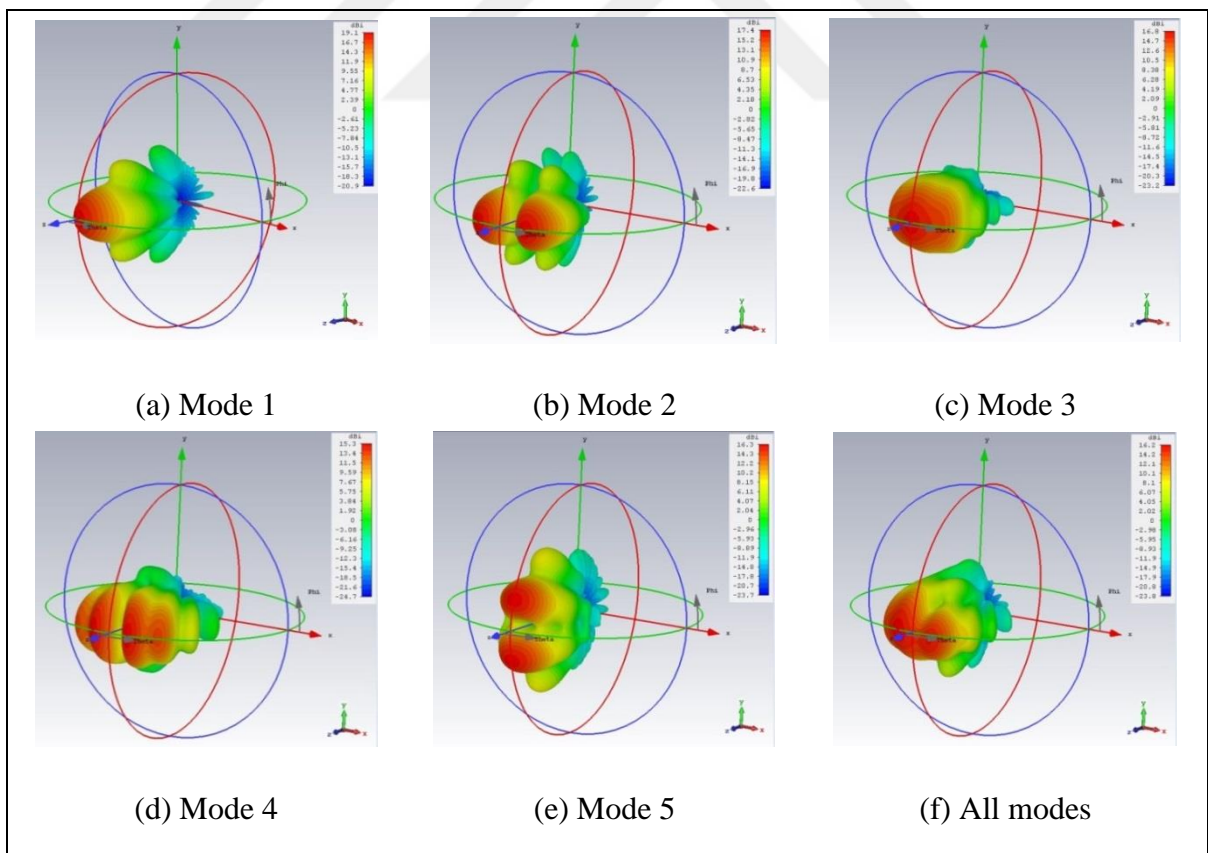
Figure 3.11. 3D far-field radiation patterns of the designed SGHA at 18 GHz

It is evident from Figure 3.11 that the far-field radiation diagrams are beginning to deteriorate with the dominant mode TE_{10} as well as the other modes (TE_{20}, TE_{01}, TE_{11}, TM_{11},) starting to propagate. Thus, the frequency range where no other modes are propagated and the radiation diagrams are not distorted can be evaluated as the operating frequency band of the antenna that is X-band for our application.

One of the parameters that can be considered to understand how the beamwidth of the antenna changes with frequency is the directivity-beamwidth product which is denoted by Dbw. Dbw is defined as

$$Dbw = DxHPBW_{az}xHPBW_{el}$$
(3.28)

where, D is directivity (linear), $HPBW_{az}$ and $HPBW_{el}$ are half power beamwidths of azimuth and elevation respectively in degrees. Dbw is similar to the gain-bandwidth product that is commonly used in electronic circuits. It is relatively constant under a variety of operating circumstances. Dbw product was examined and the results are given in Table 3.2 for various commonly used aperture distributions [34].

Table 3.2. The directivity-beamwidth products of different aperture distributions

Antenna Type	Dbw [deg^2]
No side-lobe pattern, rectangular beam	41253
No side-lobe pattern, conical beam	52525
Uniform rectangular aperture	32383
Cosine-uniform rectangular aperture, such as open ended waveguide	35230
Uniform circular aperture	33709
General use for practical antennas	26000

It could be seen from (3.28) that either Dbw should be increased in direct proportion to the directivity of the antenna or the directivity of the antenna must remain constant along the frequency band to obtain constant beamwidths.

The variation of gain and Dbw product across the azimuth and elevation beamwidth values of the designed SGHA according to the frequency are given in Figure 3.12.
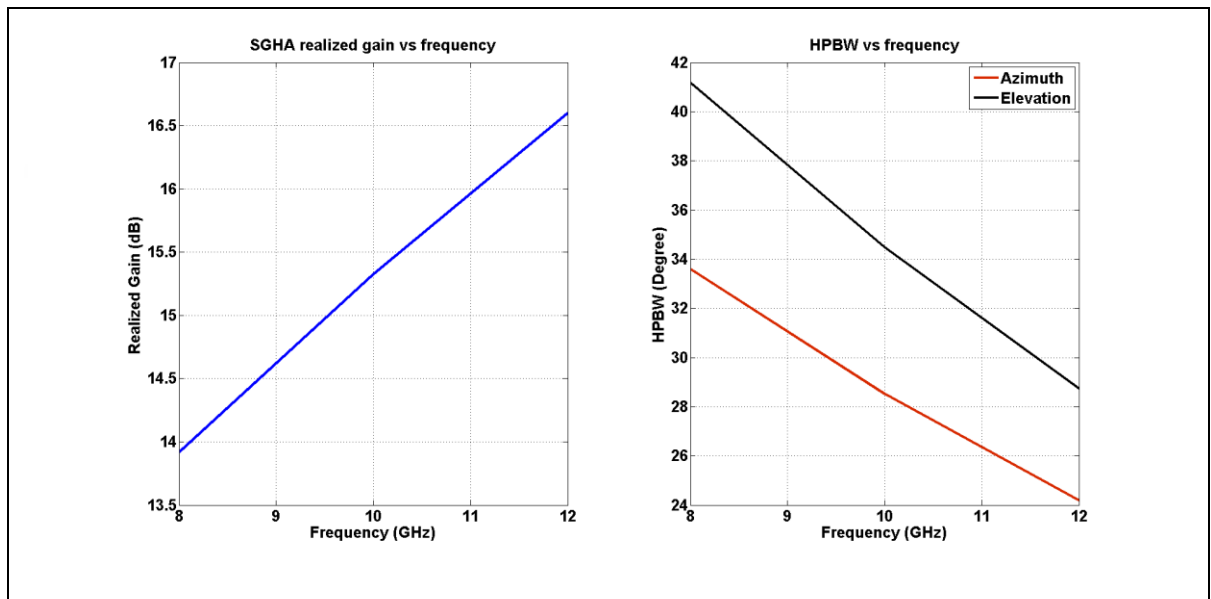
Figure 3.12. The simulated gain of the SGHA and the comparison of HPBWs in E- (elevation) and H- (azimuth) planes

Table 3.3. Dbw product of the designed SGHA

Frequency (GHz)	Directivity (Linear)	H-plane HPBW (Degree)	E-plane HPBW (Degree)	Dbw (Degree^2)
8	24.95	33.59	41.17	34506
10	34.51	28.51	34.48	33938
12	46.34	24.18	28.73	32281

Table 3.3 shows that the frequency along the operating band of the antenna increase by 1.5 times (8 to 12 GHz), while half power beamwidths on the H- and E-plane varied by 1.39 and 1.43 times, respectively. Thus, the beamwidth-frequency change of a horn antenna can be interpreted as close to the linear as expected.

3.2. DOUBLE RIDGED HORN ANTENNA

In Section 3.1, SGHA was designed to understand the frequency-beamwidth relation of horn antenna. Since the bandwidth of horn antenna is limited with a ratio of 1.5:1, there is a need for a broadband antenna. The ridged horn antenna is more desirable than other broadband antennas such as log periodic, Vivaldi or biconical because of its high gain, low VSWR, adjustable beamwidth and stable phase center characteristics. Since the bandwidth for the rectangular waveguides is defined as the ratio of the cut-off frequency of the next higher-order mode to that of the dominant, TE_{10} mode, the point we will pay attention to in DRHA design is propagating a single mode along the frequency band.

Dominant single-mode operation is achieved over the entire frequency band using the ridges in horns by lowering the cut-off frequency of the fundamental propagating mode as are in ridged waveguides. Various double or dual polarized quad ridged horn antenna designs had been carried out [35 – 40], however none of these studies explained the design procedure in detail. Previous studies on ridge waveguides determined the dimensions of the operating waveguide and the ridge geometry to include the desired frequency band as shown in Chapter 2. The same dimensions are also used in the double ridged horn antenna (DRHA) waveguide section.

In fact, DRHA is composed of three main subsections which are feed and cavity section, ridged waveguide part, and finally the ridge-loaded flare. Two different designs, mainly

  i.   without feed and cavity section (waveguide-fed)

  ii.   with feed and cavity section (coaxial-fed),

will be considered. Actually, we first design the waveguide-fed DRHA, then by modifying the ridged waveguide section and designing the feed and cavity part, coaxial-fed DRHA will be obtained. Designed models are shown in Figure 3.13. When the feed section

including the coaxial-to-waveguide adapter and cavity design is added to the antenna, the feed-cavity section interlaces with the ridged waveguide section as seen in Figure 3.13-(b).
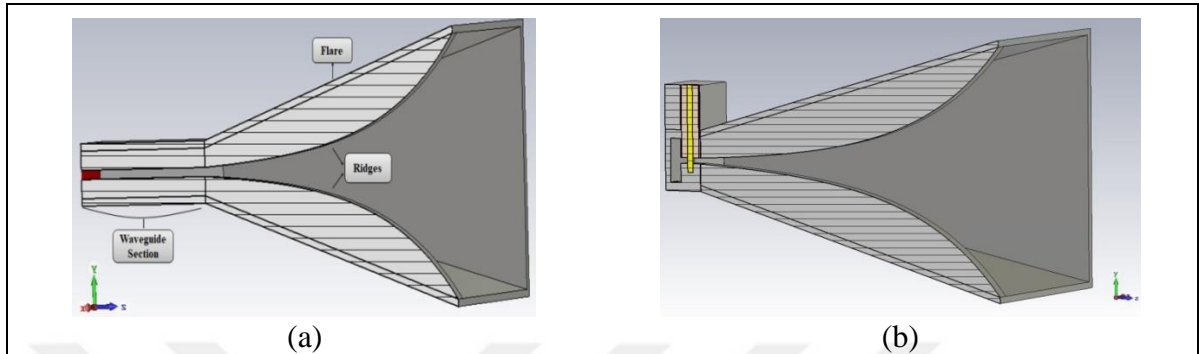
Figure 3.13. Side views of two different DRHA models: (a) With ridged waveguide section (waveguide-fed) (b) With feed and cavity section (coaxial fed)

Note that the ideal waveguide port was used to propagate modes for waveguide-fed DRHA as explained in SGHA design Section 3.2. Thus, the design of the DRHA is based on the determination of the ridged waveguide dimensions and design of the ridge-loaded flare section. Since the flare is a continuation of the waveguide, and the dimensions have already been determined in Chapter 2.3, the ridge thickness does not change initially and the main issue becomes the design of the flare.

3.2.1. Ridge-Loaded Flare

The design of ridge-loaded flare part comprises of the determination of ridge profile and flare geometry. We have explained the design of the ridged waveguide in Chapter 2.2. Now, we concentrate on the determination of how the ridge profile will be along the flare, up to the horn aperture in this Section. It is desired that ridge profile design including ridge width, and the space between the ridges provides smooth transition between the ridge impedance and the free-space impedance, 377 Ω. It is required to consider that the ridges should be extended into the flare and past the point where the horn aperture becomes sufficiently wide (half a wavelength or more in width (H-plane)) to support propagation of the TE_{10} mode at the lowest operating frequency when the ridges are designed. Note that the horn generates some higher-order modes due to an aperture width more than a half

wavelength which distorts the pattern over narrow frequency ranges unless the flare length is adjusted.

Although different ridge curvatures were extensively studied in the literature [37], [39], [41], [42], most of them were generally based on exponential tapers with an additional linear term with slope. The general equation of ridge profile can be written as follows:

$$y(z) = az + be^{cz} \qquad (3.29)$$

The linear segment in (3.29) is used as compensation to extend the frequency band. This additional linear taper term, az, has been determined experimentally and it provides a significant improvement in terms of impedance matching for the first octave of the frequency band and has little effect elsewhere [35]. It is possible to find out the values of the coefficients in (3.29) using the following equation:

$$y(z) = \frac{d}{2}e^{\beta z}, \qquad 0 \le z \le L \qquad (3.30)$$

where,

$$\beta = \frac{1}{L}\ln\left(\frac{y_{\text{aperture}}}{d}\right) \qquad (3.31)$$

z is the axial length along the horn from the straight section of the ridge, y(z) is the perpendicular distance from the center line of the horn aperture, L denotes the flare length, d is the gap between the ridges in the waveguide, and y_{aperture} represents the aperture height of the horn antenna. If we substitute β in (3.30), then applying a small algebraic simplification on (3.30), it becomes as

$$y(z) = \left(\frac{y_{\text{aperture}}}{d}\right)^{\left(\frac{z}{L}\right)} \frac{d}{2} \qquad (3.32)$$

The aperture height, flare length and ridge gap are needed to calculate (3.32). The desired flare length, aperture height and determined ridge space values are the starting points of parametric study which are used to obtain the best performance of the antenna.

The dimensions of the flare such as aperture width, height and length were obtained for X-band SGHA with 15 dBi directivity using straightforward SGHA design method described in Section 3.1. The antenna was modelled using CST Microwave Studio. The width and height of the DRHA aperture were kept same as the width and height of the designed SGHA, which are 75 and 45 mm, respectively. The parameters of a, b, and c in (3.29) were determined and the flare length were modified after parametric sweep. The simulated results of S_{11} were compared for different values of a, b and c constants as a starting point for the design of DRHA. Then, the final values of the ridge profile equation were determined. The simulation result of the designed waveguide-fed DRHA was presented in Figure 3.14.

Waveguide and ridge-loaded flare sections were combined by selecting the appropriate ridge profile after S parameter simulations. The first five propagating modes were evaluated to check the cut-off frequencies before any further continuation of the design. The port mode information was given in Table 3.4.
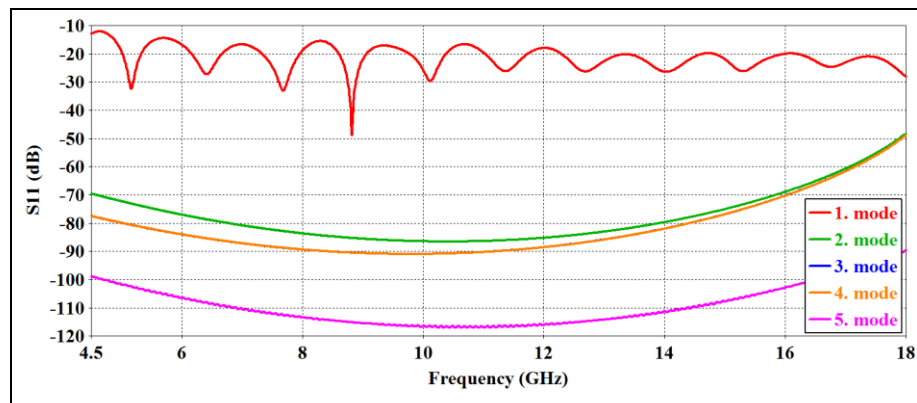
Figure 3.14. The comparison of S_{11} parameters of the first 5 modes in DRHA

Table 3.4. The cut-off frequencies and other parameters of the first 5 modes for modelled waveguide-fed DRHA at 11.25 GHz

Mode	β (1/m)	α (1/m)	Distance (-40dB) (mm)	Cut-off frequency (GHz)
1	222.66	-	-	3.70
2	-	314.80	14.63	18.77
3	-	315.33	14.60	18.79
4	-	315.33	14.60	18.79
5	-	401.54	11.47	22.22

It is evident that the designed flare section and ridges have no significant effect on the dominant mode cut-off frequency when the results are compared to the ones in Table 2.4.

The simulated model and the specifications of the waveguide-fed DRHA which was designed to have the same aperture width and height as SGHA were presented in Figure 3.15 and Table 3.5, respectively.
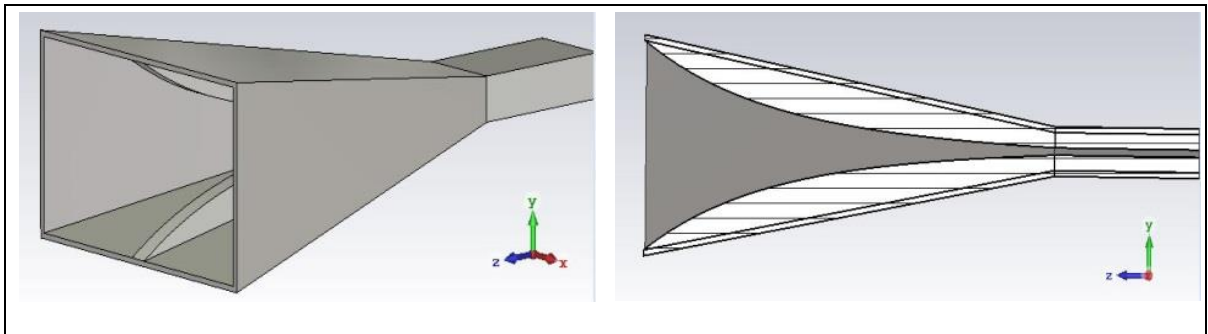
Figure 3.15. Different views of the waveguide-fed DRHA

Table 3.5. The specifications of the designed waveguide-fed DRHA

Frequency band (GHz)	4.5 - 18
Polarization	Linear (Vertical)

Gain (dBi)	9.0 – 18.3
HPBW (Azimuth) (Degree)	55.0 – 19.3
HPBW (Elevation) (Degree)	70.3 – 20.2
Aperture Dimensions (Length x Width x Height) (mm)	110 x 75 x 45
Ridge profile equation (3.29) coefficients	a=0.02, b=0.63, c=0.0316

The model was simulated using the time domain solver from 4.5 GHz to 18 GHz which corresponds to a BW ratio of 4:1. It could be understood from the S_{11} parameters and mode computation graphs that there is only one mode with a cut-off frequency below 18 GHz. The smooth transition between the antenna waveguide feed and the free-space impedance are successfully accomplished as presented in Figure 3.16.
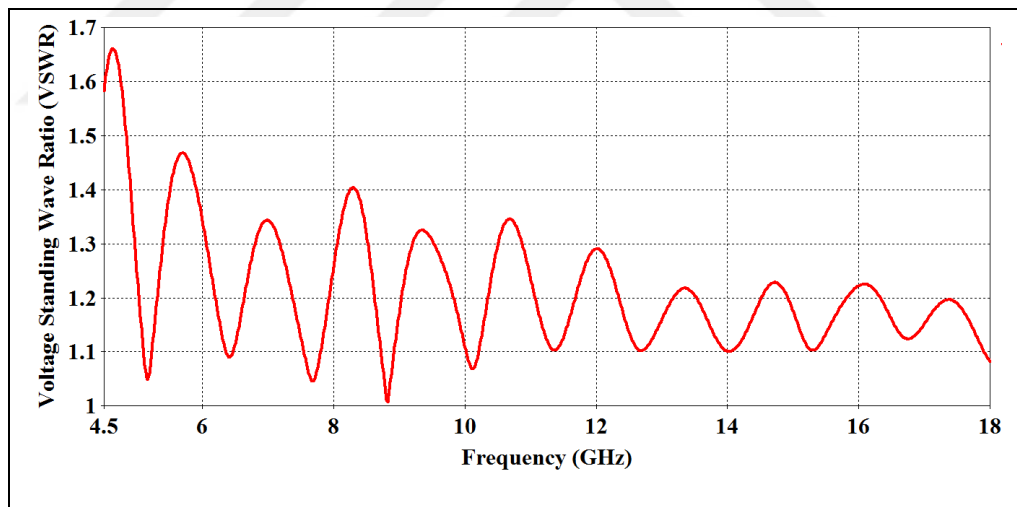
Figure 3.16. VSWR of the waveguide-fed DRHA

In fact, it was possible to design an antenna having better VSWR parameter by improving the impedance matching of the antenna, but this positive change adversely affects the antenna radiation patterns in terms of SLLs. Therefore, since the present VSWR value was acceptable, it was decided that this was the optimum design.

The E-field intensity field views and far-field radiation patterns according to simulation results were given in Figure 3.17 and Figure 3.18, respectively.

4. 5GHz

10.5 GHz

18 GHz
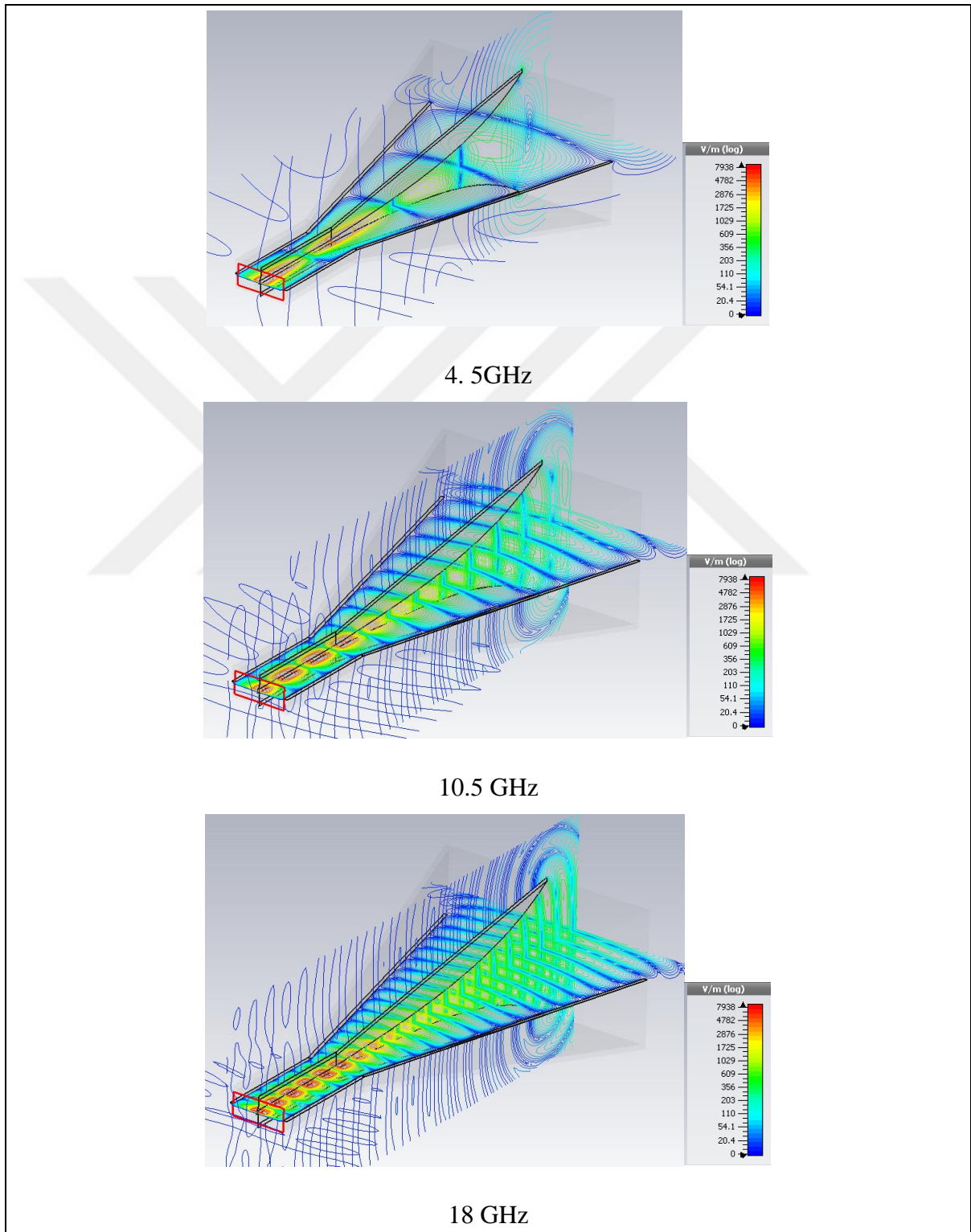
Figure 3.17. Simulated 3D E-field intensity

(a) 3D   (b) Azimuth   (c) Elevation

4.5 GHz

(a) 3D   (b) Azimuth   (c) Elevation

10.5 GHz

(a) 3D   (b) Azimuth   (c) Elevation

18 GHz
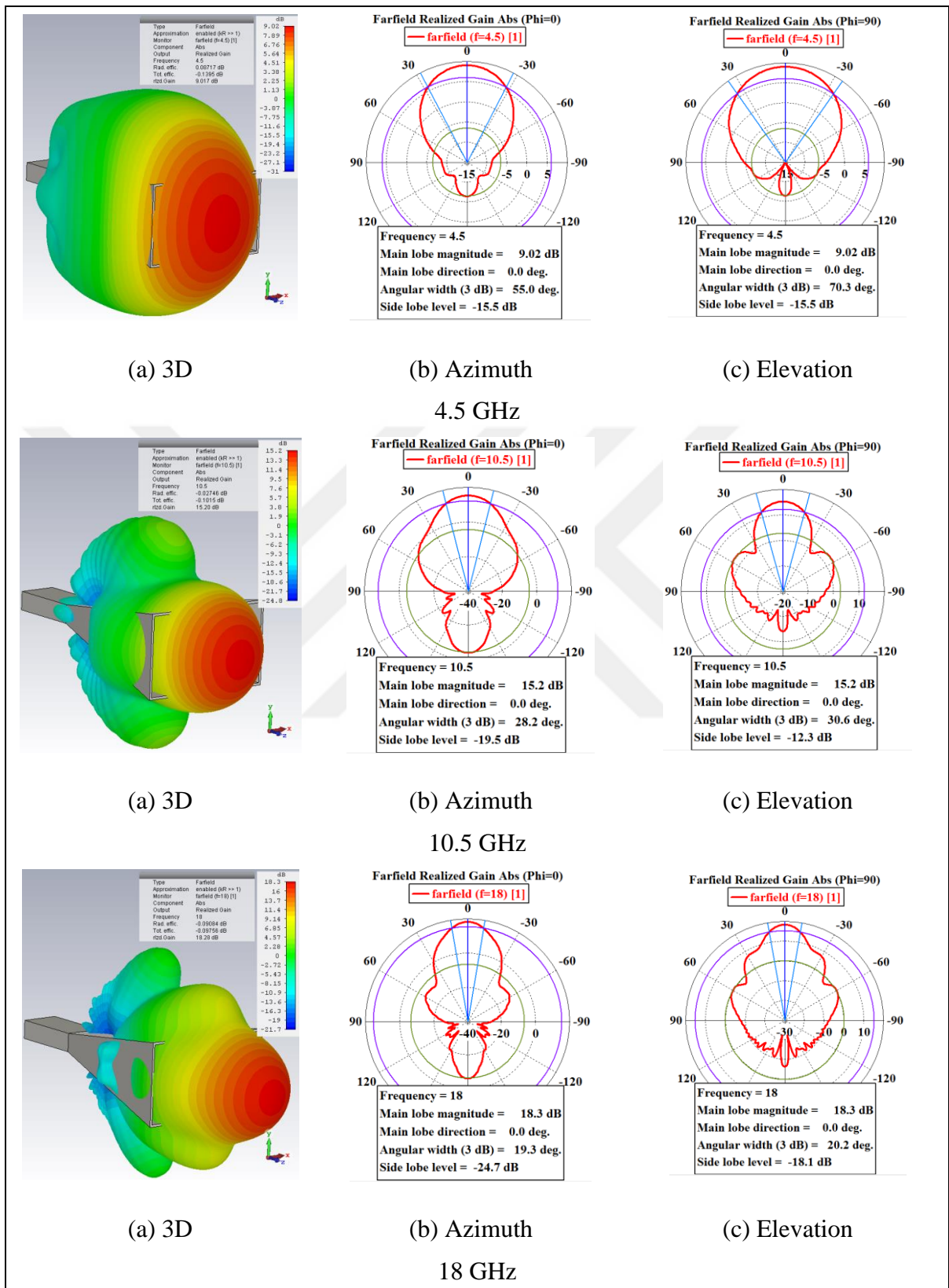
Figure 3.18. 3D, azimuth and elevation far-field radiation patterns of designed waveguide-fed DRHA.

The main advantage of the horn antenna compared to the log-periodic antenna, which is another broadband and near-constant beamwidth antenna, is that the phase center is relatively less changed with frequency. The phase center moves away from the front of the aperture to the inside of the horn with increasing the frequency, as shown in Figure 3.19. The phase center has moved 35 mm as the frequency increases from 4.5 GHz (Figure 3.19-(a)) to 18 GHz (Figure 3.19-(b)). We observe that how the horn antenna is important when the log-periodic antenna has a phase center change of approximately 80 mm between the ends of the same frequency bands.

(a) 4.5 GHz (b) 18 GHz

(c) 4.5 GHz (d) 18 GHz
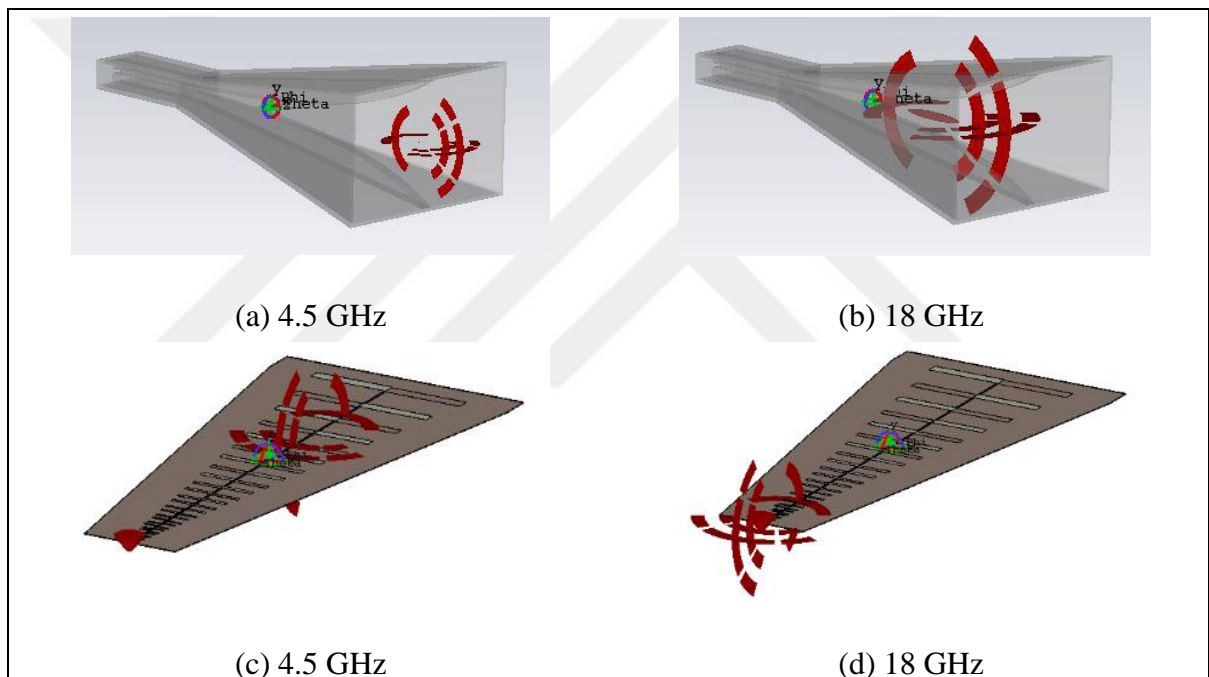
Figure 3.19. Simulated phase center movement of the DRHA and log-periodic antenna

Although there is no theoretical formula available for the estimation of gains of DRHAs as in SGHA with adequate accuracy [43], the directivity-versus-frequency characteristic of the designed waveguide-fed DRHA is observed to be similar to that of the pyramidal horn.

The variation of directivity and azimuth (H-plane), elevation (E-plane) beamwidth values of the designed DRHA with frequency are shown in Figure 3.20. Directivity and 3-dB beamwidth values of the designed DRHA are also listed in Table 3.6.
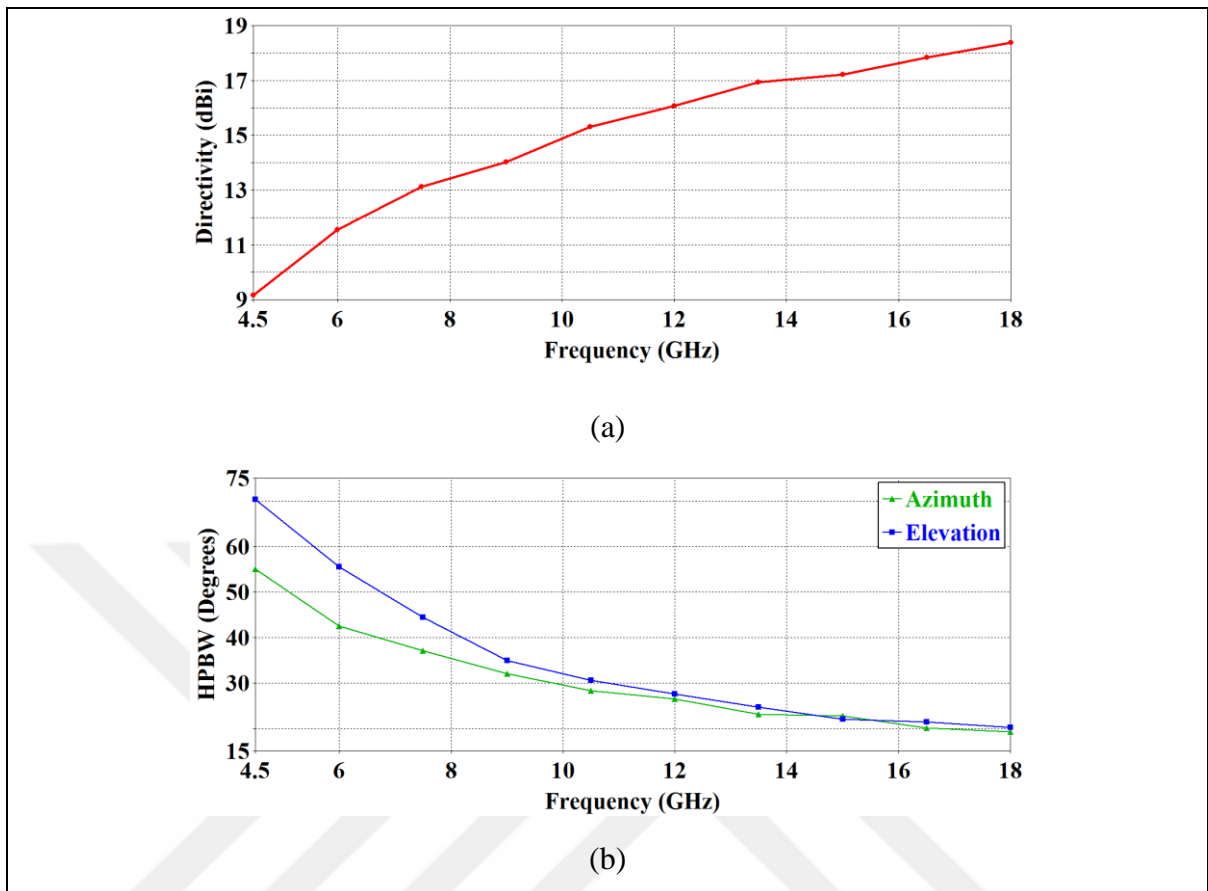
Figure 3.20. The simulated results of (a) directivity of the waveguide-fed DRHA, (b) the comparison of the HPBWs in the E- and H-planes

Table 3.6. Directivity and 3-dB beamwidth values of DRHA

Frequency (GHz)	Directivity (Linear)	H-plane HPBW (Degree)	E-plane HPBW (Degree)
4.5	8.2	55.0	70.3
7.5	20.5	37.1	44.5
10.5	33.9	28.2	30.1
12	40.4	26.5	27.5
15	52.6	22.7	22.1
18	68.8	19.3	20.2

Figure 3.20 and Table 3.6 show that HPBW's on the H- and E-plane vary by 2.9 and 3.5 times along the frequency band, respectively. Thus, it can be seen that the relationship between the beamwidth and the frequency is near-linear. Additionally, it is observed that as the frequency increases, the linear relationship begins to deteriorate.

The final part of the antenna: the coaxial-to-double ridged waveguide transformer, which allows the antenna to be fed with 50 Ω, is required to complete the DRHA design.

3.2.2. Feed and Cavity

We design the feed, that includes the design of back cavity and coaxial-to-double ridged waveguide (coax-to-rwg) transformer after the design of ridged waveguide and ridge-loaded flare. The coax-to-rwg transition is designed to suppress any higher order double ridged waveguide modes that can propagate. It should be noted that the feed and cavity part is very important for higher-order mode suppression and feed-to-free space matching performance.

The critical design goal is to provide a smooth transition between the coaxial TEM mode and the dominant TE_{10} mode in the ridged waveguide. Previous design methods for a variety of particular junctions were presented with a detailed description in [44]. The fundamental way of propagating a desired mode in a waveguide is the excitation of either the electric or the magnetic field intensity with the specific mode. This can be achieved either by means of a probe element parallel to the electric field or by means of a coupling loop in the waveguide, which the plane of loop was normal to the magnetic field. Although each type of junctions were used in different type of applications, transitions based on electric coupling are more preferred over the other.

In this study, we connect the inner conductor of the coaxial line to the opposite side of the ridge, while the other side is in contact with the outer conductor. 50-Ω SMA female connector, Huber+Suhner model 23_SMA-50-0-3/111_NE, is modelled in the simulations. The back cavity and the feed structure in a ridged waveguide are shown from different views in Figure 3.21.

(a)

(b)
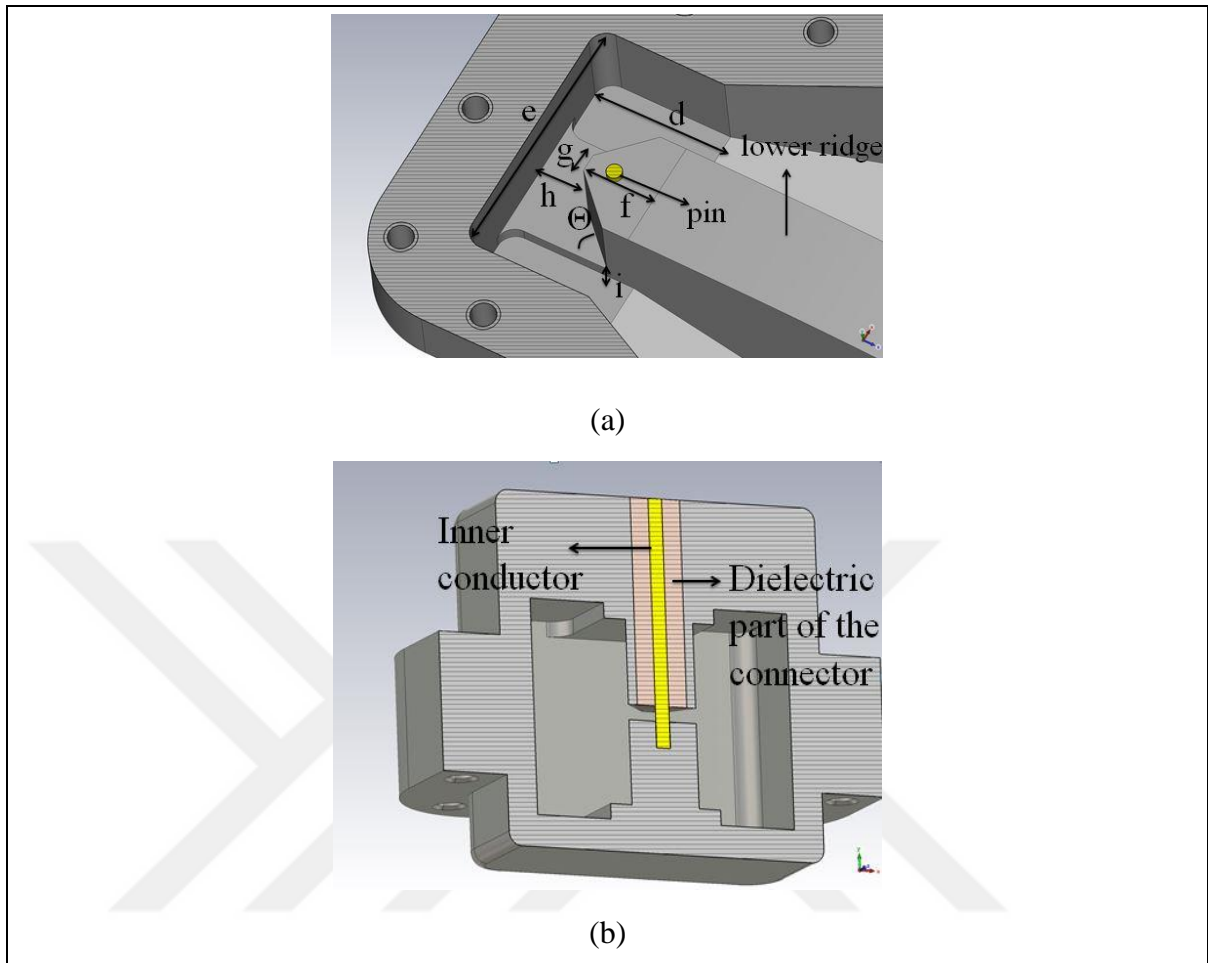
Figure 3.21. Different views of back-cavity geometry.

The major difference compared to the conventional back cavities is in the back cavity part. The width of the chamfered back ridge, g, and the chamfer angle, Θ, are the critical parameters to improve the matching and to achieve a VSWR less than 2 along the frequency band. Effects of key design parameters were previously explained in [45]. The final values of the back cavity dimensions are determined as a result of the parametric study for the whole frequency band from 4.5 GHz to 18 GHz and they are given in Table 3.7. The number of individual parts of the antenna is reduced and the production of the antenna becomes relatively simple using this back cavity design. Thus, the manufacturing cost may be also reduced. The simplicity in back cavity design also decreases the possibility of performance deterioration due to antenna manufacturing, and increases the consistence between the simulation and measurement results.

Table 3.7. Mode information for the first 3 modes of a modelled coaxial-fed DRHA at 11.25 GHz

Mode	Type	Line impedance (Ohms)	Cut-off frequency (GHz)
1	TEM	48.4	-
2	TE	-	25.0
3	TE	-	25.1

Table 3.7 shows that only dominant TEM mode propagation occurs in the operating frequency band and the line impedance of the designed feed port is calculated as 48.4 Ω which is so close to the desired impedance 50 Ω.

Table 3.8. Final dimensions of the feed and back-cavity section

Back cavity length (d) (mm)	8.2
Waveguide width (e) (mm)	20.5
Cavity ridge length (f) (mm)	3.1
Chamfered width (g) (mm)	1.7
Distance between the back of waveguide and the ridge (h) (mm)	3.3
Short ridge height (i) (mm)	0.5
Ridge width (mm)	5.3
Gap between the ridges (mm)	1.2
Chamfered angle (Θ) (degree)	45°

Finally, the corners of the cavity ridge are smoothed to improve the VSWR performance at the beginning and at the end of the frequency band in addition to the dimensions given in Table 3.8. The modified model and the effect on VSWR are shown in Figure 3.23.
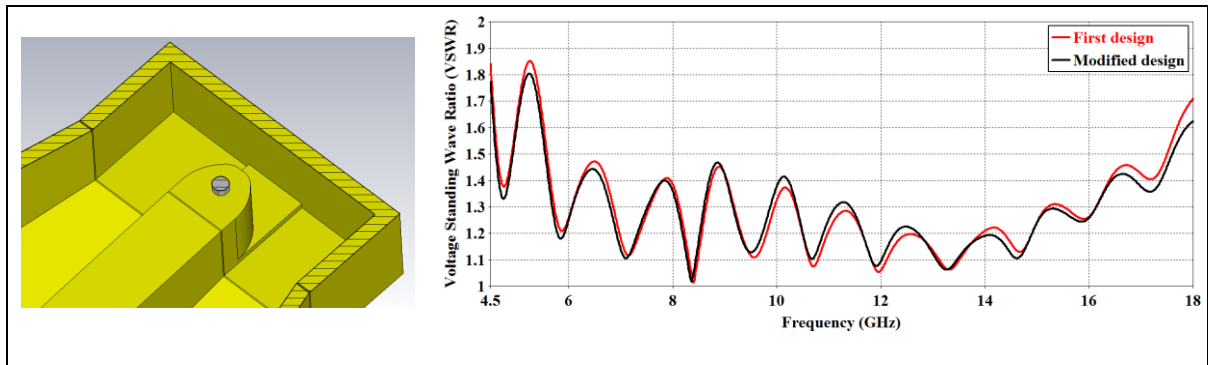
Figure 3.22. Final back-cavity geometry and VSWR comparison of two models

The specifications and the radiation patterns according to simulation results are given in Table 3.9 and Figure 3.23.

Table 3.9. The specifications of the designed coaxial-fed DRHA

Frequency band (GHz)	4.5 – 18
Polarization	Linear (Vertical)
Gain (dBi)	8.7 – 18.4
HPBW (Azimuth) (Degree)	55.4 – 18.4
HPBW (Elevation) (Degree)	72.1 – 19.8
Antenna dimensions (L x W x H) (mm)	120 x 75 x 45
Ridge profile equation (3.29) coefficients	a=0.02, b=0.63, c=0.0316

As a result, we completed the design of the coax-fed DRHA in the frequency band 4.5 – 18 GHz with smooth but frequency-varying radiation patterns. We observe that the frequency along the operating band of the antenna is increased by 4 times, HPBWs on the H- and E-plane varied with a ratio of 3.0 and 3.6, respectively. The relationship between the beamwidth and the frequency is near-linear but inversely proportional as expected. In the next chapter, we explain the details of how we can design a new antenna to ensure the constancy of the beamwidth along the frequency band.

(a) 3D   (b) Azimuth   (c) Elevation

4.5 GHz

(a) 3D   (b) Azimuth   (c) Elevation

10.5 GHz

(a) 3D   (b) Azimuth   (c) Elevation

18 GHz

Figure 3.23. 3D, azimuth and elevation far-field radiation patterns of designed coaxial-fed

DRHA

4. NEAR-CONSTANT BEAMWIDTH WIDEBAND HORN ANTENNA

In this chapter, the literature review about near-constant beamwidth horn antenna (NCBWHA) is provided. The reasons that prevent the beamwidth constancy along the frequency band, and the requirements to achieve this property will also be investigated in this chapter. Furthermore, the required changes in the new type of DRHA design will also be determined. The changes will be examined one by one and the impact of parameters on the performance of an antenna will be analysed. Additionally, the designed antenna will also be compared with coaxial-fed DRHA that we have implemented in Chapter 3.

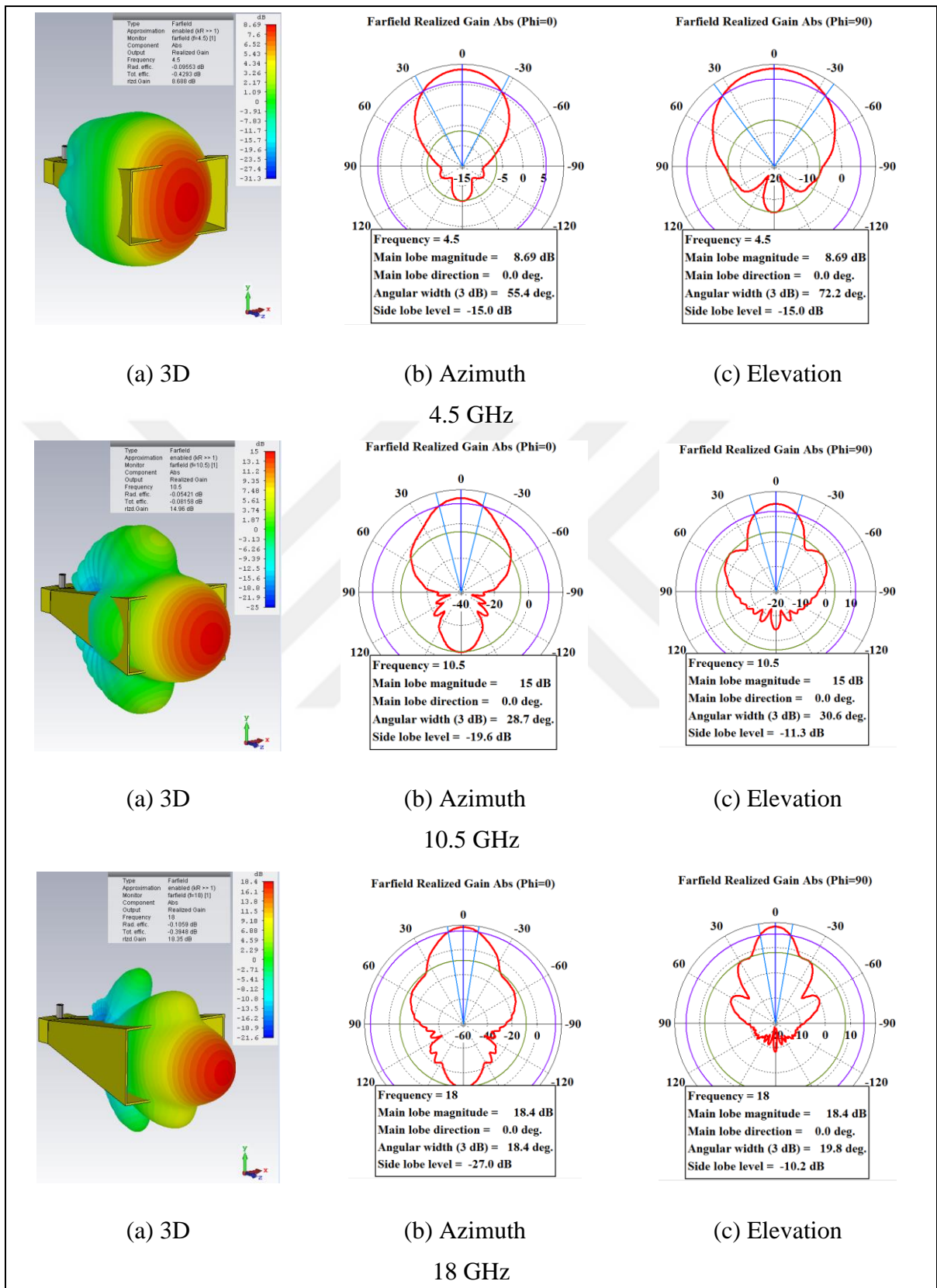Several methods were proposed to solve constant-beamwidth problem. Some of the solutions provided partial improvements, but failed to produce a complete result. The bandwidth was not sufficient in some of the previously proposed studies, and in others, the constancy of the beamwidth could not be achieved at the desired level, and the antenna radiation pattern deterioration could not be prevented along the frequency band.

Different techniques were investigated to design ultra-wideband (UWB), 10 dB-beamwidth frequency-independent feed antennas with suppressed higher order modes and low cross polarization levels to be used as a feed for novel reflector antennas (i.e. radio astronomy applications). Circular quadruple-ridged flare horns (QRFHs) achieving near-constant 10 dB-beamwidth was designed using different types of feed sections and exponentially profiled sidewalls. The quad ridged horn achieved near-constant beamwidth supporting multiple modes at the horn aperture that had appropriate magnitude and phase relationships. These multiple modes were generated by the curvatures of ridge and sidewall profiles [46]. Balanced excitations were realized to achieve UWB performance using a balun (balance to unbalance transformer), which was also considered as bulk, and led to power dissipation losses [47]. However, its H-plane 10 dB-beamwidth varied with as much as a factor of 3 over the frequency band with a ratio of 6:1. This strong variation resulted from rapid narrowing in the beam at high frequencies, where the contribution of the high-order modes increased. A metal ring structure, which was introduced in the design of QRFH in [48] to suppress the TE_{12} mode in the throat part, was shown to improve the E-plane beam performance however it did not make a contribution to the H- plane pattern.

The concepts of constant H-plane beamwidth horns were first investigated by Dewey [1]. Dewey considered the cylindrical apertures and horns fed by sectoral waveguide type flares. An H-plane sectoral horn had an almost constant H-plane radiation pattern over a very wide frequency range, if only excited by the fundamental TM_{01} mode [49]. On the other hand, it should not be forgotten that the TM_{01} mode does not exist in a rectangular waveguide. A new type of differential feed called a quadraxial feed, which was excited by two orthogonal differential modes, was used in another UWB QRFH that removed the need for balun. It was shown that the quadraxial feed improved the modal content in the throat part of QRFH compared with the conventional coaxial feed when strongly exciting the fundamental TE_{11} mode during the suppression of the unwanted higher-order modes. The far-field patterns of the coaxial-fed horn exhibited larger ripples, as compared to that of the twinax-fed horn, which was expected because of the presence of higher-order modes in the throat part with the coaxial excitation [50]. A decade bandwidth DRHA with a coaxial to double ridged waveguide launcher was designed from 10 to 100 GHz [51]. Half-cosine transition into a linear taper for the outer waveguide dimensions and ridge width was used to achieve stable beamwidth over the frequency band [51]. On the other hand, it was shown that the elliptical sidewalls affected the radiation pattern positively, decrease the pattern degradation, and provide relatively constant beamwidth [52]. Additionally, lens designs were also applied to conventional horn antennas to improve the radiation patterns. Radiation pattern distortion occurs in the high frequency band of conventional ridged horn antennas because of the larger phase error at the antenna aperture as the frequency increases. Dielectric lens loading had been introduced to reduce the phase error, which helped to improve high frequency band radiation patterns in the antennas and to increase the gain in the entire frequency band [42], [53 – 56]. However, no contribution had been made to the beamwidth constancy of the antennas. Relatively wideband antennas, polyrod radiators which were more broadband radiators of end-fire antennas, were also investigated but they could produce a constant beamwidth over only 2:1 band [3].

Since the application areas (generally designed as reflector feed for radio astronomy) of the antennas mentioned above were different, the priorities in design were also different. These antennas did not meet our requirements and the characteristics such as HPBW, smoothness of the radiation pattern, and the most important parameter, bandwidth were insufficient.

Thus, the need for a different design had emerged considering different priorities. We focus on these requirements in this dissertation.

As it is previously mentioned, the design of the DRHA in the frequency band $4.5 - 18$ GHz is performed in Chapter 3 with smooth but frequency-varying beamwidth radiation patterns. In this chapter, we will design a new type of horn antenna to provide near-constant beamwidth over the desired frequency band. The main reasons for beamwidth variation, the solutions that were tried in the literature, the designed antennas, and their deficiencies are explained up to now in general. The applied solutions with designed antennas and simulation results will be given by comparing with previous antennas in this chapter.

4.1. PINWALL (GRID) ANTENNA

We have first studied on the dimensions of the flare (i.e. flare length and aperture size) of the designed coaxial-fed DRHA and ridge taper to improve constant beamwidth. Note that the horn aperture becomes sufficiently wide (half a wavelength or more in width (H-plane)) to support propagation of the TE_{10} mode at the lowest operating frequency. However, an aperture more than a half wavelength wide at the lowest frequency means more wavelengths wide at higher frequencies which causes large phase errors across the aperture unless the horn is extremely long. At the same time, when the pins are inserted, the flare must be over a certain length when considering the number of pins to be used and the distance between the pins. Thus, the aperture height and flare length are also enlarged as the aperture width of the antenna is expanded. It is known that use of a large H-plane flare angle may improve the frequency independence of H-plane radiation pattern over a wide bandwidth. It was previously provided by producing a sufficient phase difference between the edge and the center of the aperture with increasing frequency that counteracted the beam narrowing [57].

The beamwidths of the antenna in both E- and H-plane depend on the electric field distribution across the aperture. The relationship between frequency and 3-dB beamwidth is linear as expressed using the following equation regardless of the aperture field distribution type, i.e. uniform, cosine, Gaussian, etc. [24] as

$$\text{HPBW}_{E(H)} = k_{E(H)} \frac{\lambda}{A(B)} \; rad \qquad (4.1)$$

where, $A(B)$ is the aperture width (height), and $k_{E(H)}$ is beamwidth factor associated with the E-field aperture distribution in E(H)-plane. Since the horn is fed by a rectangular waveguide, the dominant mode is TE_{10}. Thus, the aperture phase is uniform in H-plane and amplitude distribution is a cosine taper in E-plane. The aperture electric field distribution of this type of horn antenna is obtained by combining the fields for H- and E-plane sectoral horns. The E-field distribution across the aperture and H-plane power pattern of the H-plane sectoral horn are given in the following equations so that the flare design can start from this plane [58] as

$$E_y(x) = C_x \cos\left(\frac{\pi x}{A}\right) \frac{\sqrt{L_H}}{\sqrt[4]{(L_H{}^2 + x^2)}} e^{\left\{-jk\left[\sqrt{(L_H{}^2 + x^2)} - L_H\right]\right\}} \qquad (4.2)$$

$$P(\Theta) = \cos^2\Theta \left| \frac{\int_{-A}^{A} E_y(x) e^{(jkx\sin\Theta)} dx}{\int_{-A}^{A} E_y(x) dx} \right| \qquad (4.3)$$

where, C_x is a constant, L_H represents the throat length according to geometry that was in Figure 3.1 and $k = 2\pi/\lambda$ is the free space phase constant. The mean value of constant beamwidth curve is given in Figure 4.1 according to the power pattern given in (4.3).
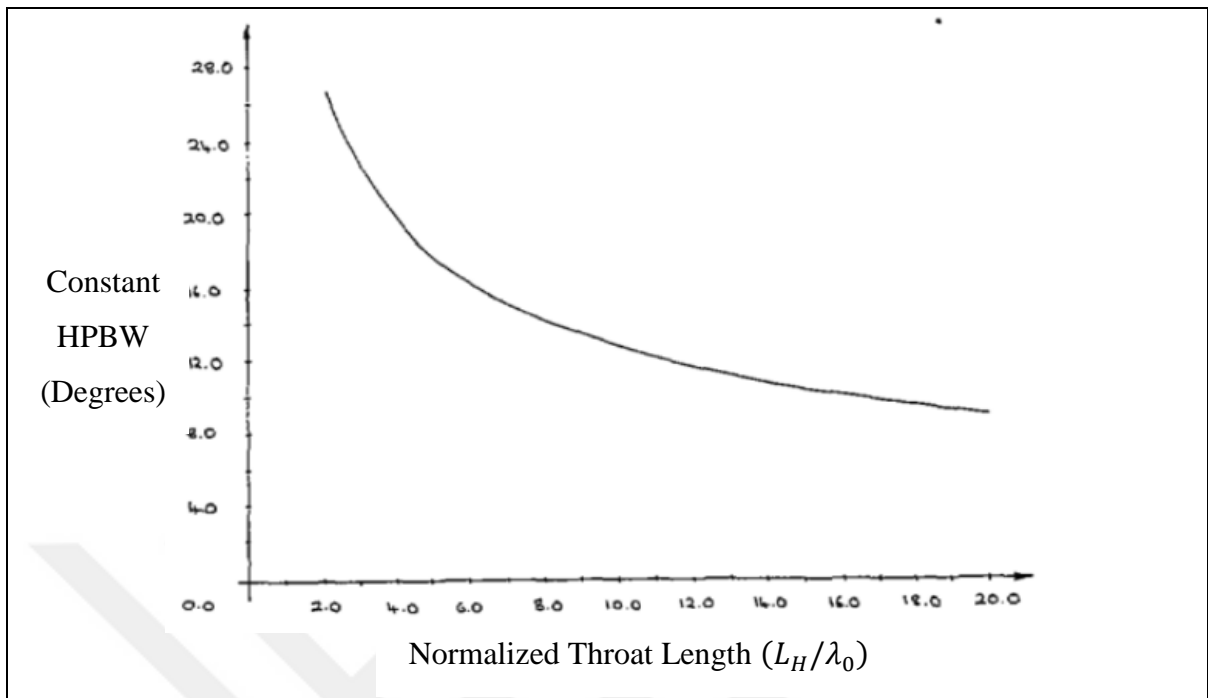
Figure 4.1. Constant beamwidth design curve for cosine aperture distribution (i.e. aperture phase taper=0.37λ_0 at $\lambda=\lambda_0$) (copied from [58])

Figure 4.1 shows the mean value of constant beamwidth with flare length variation for cosine aperture distribution. It can be used for the H- plane radiation pattern beam as well as determining the throat length and aperture width of the antenna to be designed. The term constant beamwidth is used to imply ± 12 per cent variation about the mean 3-dB beamwidth level over a 2.4:1 band in [58]. The aim of this dissertation is to adjust the mean value of H-plane beamwidth to be about 30 degrees, therefore, we need to extend the throat length of the DRHA between roughly 2.5 - 3 $\lambda_{4.5}$, which corresponds to 165 – 198 mm.

The physical modifications of the DRHA designed in Chapter 3 were based on two points:

i. One of the points is H-plane design, which is the determination of the flare length and aperture width that depend on the aperture phase taper and desired azimuth 3-dB beamwidth.

ii. The other point is the aperture height that depends on the ridge profile which is more related to impedance taper.

Thus, it is necessary to modify structures and dimensions which are preferred in conventional horn antenna design to change the frequency-beamwidth relationship of the horn antenna. The guidelines can be followed as follows for constant beamwidth:

- The throat length (L_H) in terms of wavelength corresponding to the desired 3-dB beamwidth value is required to be found in Figure 4.1.

- The phase aperture taper for the lowest frequency point should be 0.37λ which means the following equation must be satisfied

$$(L_H{}^2 + x^2)^{1/2} - L_H = 0.37\lambda \tag{4.4}$$
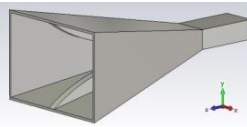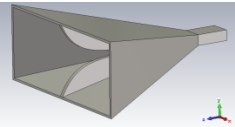
where, $x = A/2$. Hence only unknown parameter A can easily be found. Thus, the aperture width and the throat length can be determined after guidelines given above including (4.4). We evaluated the first three propagating modes to check the cut-off frequencies before we continued the design of the antenna. The ridge transition is normally a strong moding device but this can be prevented using an appropriate ridge profile. The port mode information is given in Table 4.1. It can be seen that the designed expanded flare and ridges have no negative effect on the dominant mode cut-off frequency.

Table 4.1. Mode information for the first 3 modes of a modified coaxial-fed DRHA at 11.25 GHz

Mode	Type	Line impedance (Ohms)	Cut-off frequency (GHz)
1	TEM	48.5	-
2	TE	-	25.2
3	TE	-	25.3

The revised DRHA dimensions and the specifications of the modified coax-fed DRHA are given in Table 4.2. The far field radiation patterns according to simulation results are also shown in Figure 4.2.

Table 4.2. The comparison of the designed waveguide-fed DRHA and modified DRHA specifications

Parameters	DRHA	Modified DRHA
Frequency band (GHz)	4.5 – 18	4.5 - 18
Polarization	Linear (Vertical)	Linear (Vertical)
Gain (dB)	8.7 – 18.4	12.2 – 15.7
HPBW (Azimuth) (Degree)	55.4 – 18.4	34.6 – 25.5
HPBW (Elevation) (Degree)	72.1 – 19.8	43.5 – 30.5
VSWR	< 2	< 2
Aperture Dimensions (Flare Length x Width x Height) (mm)	110 x 75 x 45	182 x 205 x 93
Ridge profile equation coefficients	a=0.02, b=0.63, c=0.0316	a=0.02, b=0.003, c=0.0525

(a) 3D   (b) Azimuth   (c) Elevation

4.5 GHz

(a) 3D   (b) Azimuth   (c) Elevation

10.5 GHz

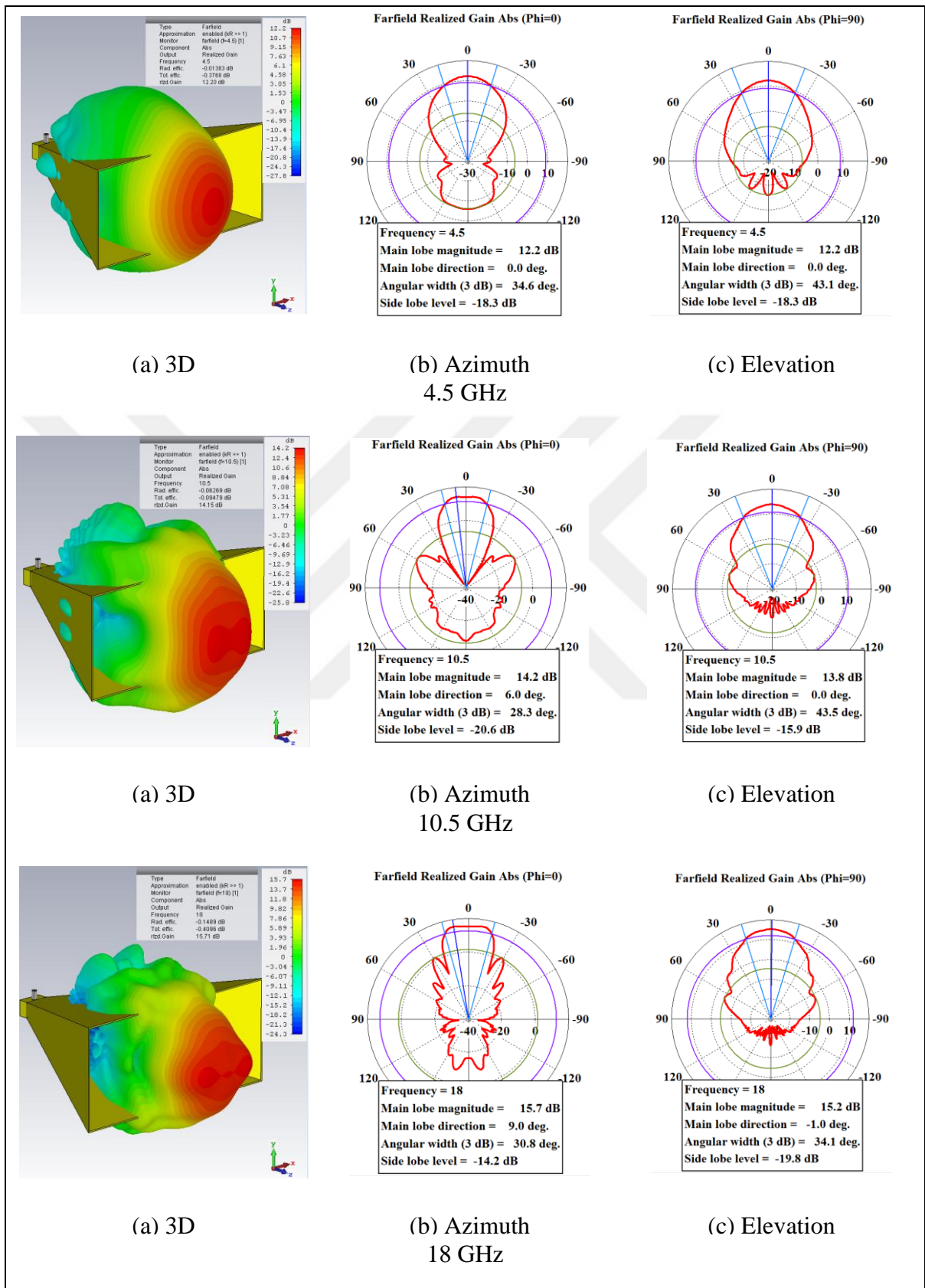(a) 3D   (b) Azimuth   (c) Elevation

18 GHz

Figure 4.2. 3D, azimuth and elevation simulated far-field radiation patterns of designed modified coax-fed DRHA

The directivity and azimuth-elevation beamwidth values of the coax-fed DRHA designed in Chapter 3.3 and its modified version are compared and the comparison results are presented in Figure 4.3.
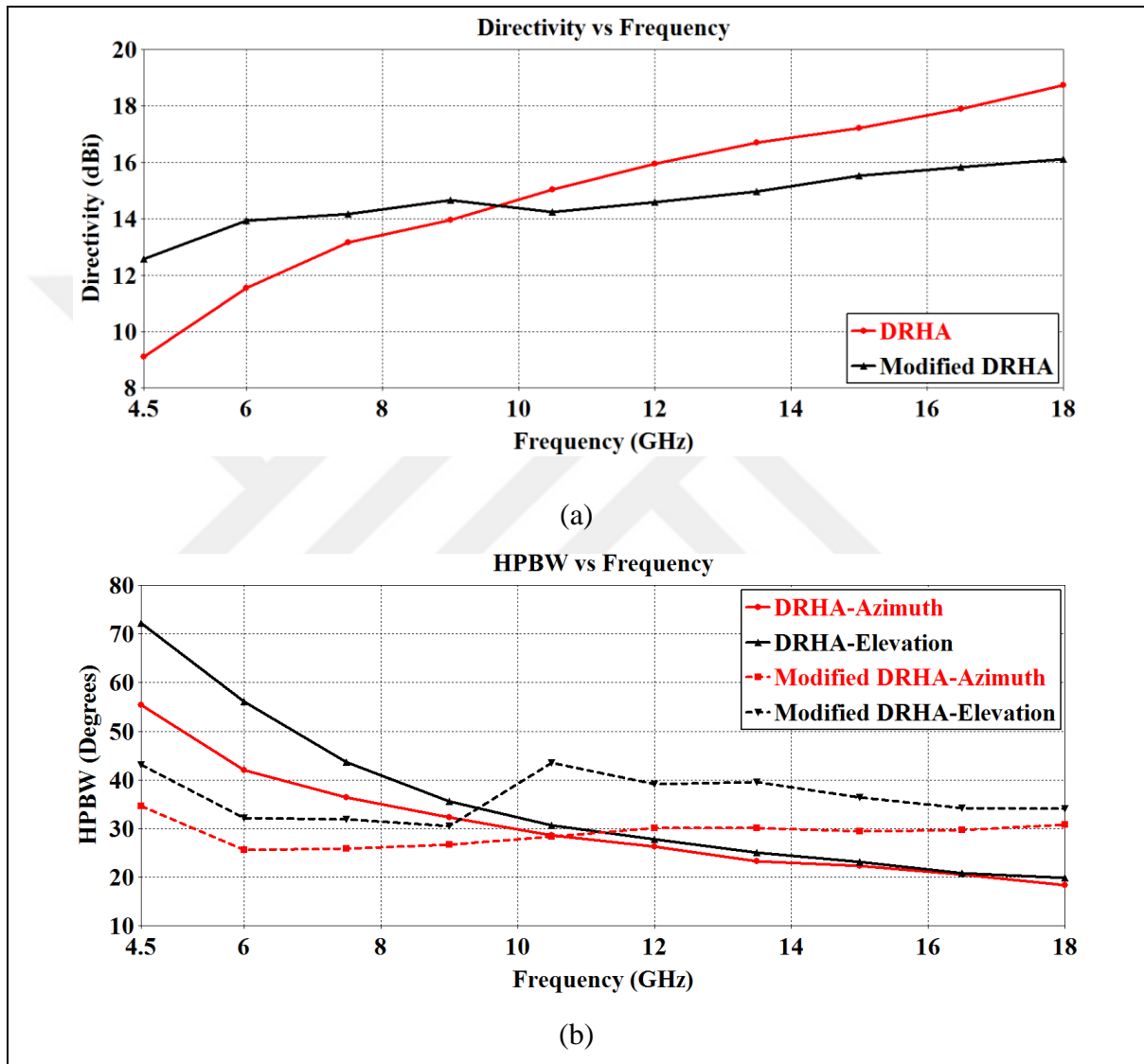
Figure 4.3. The comparison of simulated (a) directivity and (b) HPBWs in E- (elevation) and H-planes (azimuth)

Figure 4.3 shows that the frequency along the operating band of the antenna increase by 4 times (4.5 to 18 GHz), while HPBWs on the H- and E-plane vary by 1.36 (± 15.1 per cent variation about the mean 3-dB beamwidth) and 1.43 (± 17.8 per cent variation about the mean 3-dB beamwidth) times, respectively. We note that there is a considerable

improvement in beamwidth constancy. However, we also observe that the beginning of the band still needs to be improved.

It also appears that the desired progression cannot be achieved only by changing the flare or aperture dimensions. More structural changes are needed and the sidewalls should be redesigned.

A new type of horn antenna, called a "pinwall" [3] or "grid" antenna is introduced to provide a substantially constant beamwidth over a BW ratio of 4:1. The basic principle behind this antenna lies in the replacement of horn sidewalls by properly positioning the pins to allow higher frequencies to radiate from a small aperture while limiting lower frequencies until larger apertures are reached. Since replacing the sidewalls of the flare parallel to the E-field vector with conductive pins produces the H-plane (azimuth) pattern, pinwalls designed with applied progressive curved conductive pins give better results especially in H-sector. Unlike the study in [3], the ridges are used at the same time in our design to expand the frequency band.

The main issue in this design is to determine the number of pins required, and to decide the position of the pins. Several models with different number of pins and different distances between the pins were previously tried, and the patterns were compared to achieve the desired correct results [3]. 8, 12 and 24 pins-antennas obtained by arranging these pins in different spaces were compared, and finally an antenna design with azimuth beamwidth variation ±4 degrees from 22 degrees was obtained. However, it was noticed that the beam shapes were not very smooth and they observed a beam split in the high end of the frequency band.

Initially, the points where the pins are to be positioned is determined. For this, the distance between the pins is set to be the function of the frequency by considering the number of pins. There are two possible approaches for this decision. We can divide the frequency band linearly as well as logarithmically, which gives a uniform equal percentage increase in pin spaces. Since it was previously determined that a minimum of 8 pins were required [3], [59], we have started our design with the assumption of using 7, 8 and 10 pins. The frequency band can be divided linearly and logarithmically as calculated values are given in Tables 4.3, 4.4 and 4.5. Space-1 represents the half-wavelength distances corresponding to the respective frequency point from 4.5 GHz to 18 GHz. Space-2 distances refer

proportionally to the wavelength of the related frequency point of the total flare length. Therefore, Space-1 depends only on frequency points, i.e. the number of pins to applied, but Space-2 also depends on the flare length. Meanwhile, although the increase in performance as the thickness of the pins decreases, it is taken as 3 mm instead of 1 mm for ease of manufacturing. The distances between pins are calculated according to this thickness and 182 mm flare length.

Table 4.3. Space dimensions of an antenna with 7 pins

Pin (Space) Number	a-Linear			b-Logarithmic		
	Frequency (GHz)	Space-1 (mm)	Space-2 (mm)	Frequency (GHz)	Space-1 (mm)	Space-2 (mm)
1	4.5	33.3	36.8	4.5	33.3	41.4
2	6.75	22.2	32.2	5.67	26.4	32.8
3	9	16.7	27.6	7.14	21	26.1
4	11.25	13.3	23	9	16.7	20.7
5	13.5	11.1	18.4	11.34	13.2	16.4
6	15.75	9.5	13.8	14.29	10.5	13.1
7	18	8.3	9.2	18	8.3	10.4

Table 4.4. Space dimensions of an antenna with 8 pins

Pin (Space) Number	a-Linear			b-Logarithmic		
	Frequency (GHz)	Space-1 (mm)	Space-2 (mm)	Frequency (GHz)	Space-1 (mm)	Space-2 (mm)
1	4.5	33.3	31.6	4.5	33.3	35.6
2	6.42	23.3	28.2	5.49	27.3	29.2
3	8.35	17.9	24.8	6.69	22.4	23.9
4	10.29	14.6	21.4	8.15	18.4	19.7
5	12.21	12.3	18.1	9.94	15.1	16.1

6	14.14	10.6	14.7	12.11	12.4	13.2
7	16.07	9.3	11.3	14.77	10.2	10.9
8	18	8.3	7.9	18	8.33	8.9

Table 4.5. Space dimensions of an antenna with 10 pins

Pin (Space) Number	a-Linear			b-Logarithmic		
	Frequency (GHz)	Space-1 (mm)	Space-2 (mm)	Frequency (GHz)	Space-1 (mm)	Space-2 (mm)
1	4.5	33.3	24.3	4.5	33.3	27.6
2	6	25	22.3	5.25	28.6	23.7
3	7.5	20	20.3	6.12	24.5	20.3
4	9	16.7	18.3	7.14	21	17.4
5	10.5	14.3	16.2	8.33	18	14.9
6	12	12.5	14.2	9.72	15.4	12.8
7	13.5	11.1	12.2	11.34	13.2	11
8	15	10	10.1	13.23	11.3	9.4
9	16.5	9.1	8.1	15.43	9.7	8
10	18	8.3	6.1	18	8.3	6.9

The number of pins is determined by looking at the first and the last pin spaces. As the number of pins increased, the final distance at Space-2 got smaller and smaller (18 GHz), that should be at a certain minimum level, approximately half-wavelength of the related frequency point. When the number of pins is too small, the first Space-2 distance (4.5 GHz) got bigger and the difference between the half-wavelength of the corresponding frequency is increasing, however there must be a limit. Thus, by dividing and comparing the operating frequency band linearly and logarithmically, natural boundaries on the number of pins are determined by the wavelengths of the lower and upper frequency points to start the design.

The antenna design is based on the 8-pin system where the lengths of space-1 and space-2 distances are closest to each other, and then this is compared with the designs made by considering other pin numbers. Since the logarithmic distribution gives a uniform equal percentage increase between the spaces, this approach is chosen. Meanwhile, the width of the aperture at the location where the pins are located is adjusted to achieve the desired beamwidth.

The simulated model and the specifications of the coax-fed pinwall DRHA are given in Figure 4.4 and Table 4.6, respectively.
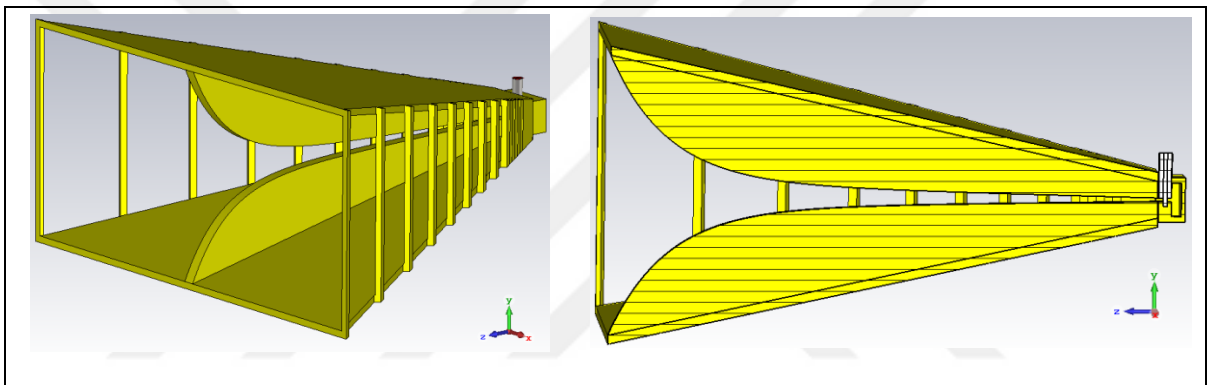

Figure 4.4. Different views of the coax-fed pinwall DRHA

Table 4.6. The specifications of the designed coax-fed pinwall DRHA

Frequency band (GHz)	4.5 - 18
Polarization	Linear (Vertical)
Gain (dBi)	11.9 – 15.4
HPBW (Azimuth) (Degree)	35.1 – 28.1
HPBW (Elevation) (Degree)	40.5 – 32.2
Space dimensions (mm)	1: 35, 2: 28, 3: 23, 4: 18, 5: 15, 6:13, 7: 11, 8: 9

The similar coaxial-to-double ridged waveguide transformer as the feed structure of the antenna designed in the previous Chapter 3.3 is used and the smooth impedance matching is successfully accomplished. VSWR of the antenna is obtained less than 2 over the desired frequency band, 4.5 - 18 GHz. The far-field radiation patterns according to simulation results are given in Figure 4.5.

The variation of directivity and azimuth-elevation beamwidth values of the designed pinwall DRHA according to the frequency are shown in Figure 4.6. The frequency along the operating band of the antenna increases by 4 times, while 3-dB beamwidths of the pinwall DRHA on the H- and E-plane vary by 1.25 and 1.26 times, respectively. These ratios were 3.0 and 3.6 for DRHA designed in Chapter 3, 1.36 and 1.43 for the modified DRHA. Thus, it can be noticed that the linear relationship (inverse proportion) between the frequency and beamwidth is broken and a more stable constant beamwidth is obtained with pinwall DRHA than the modified antenna.
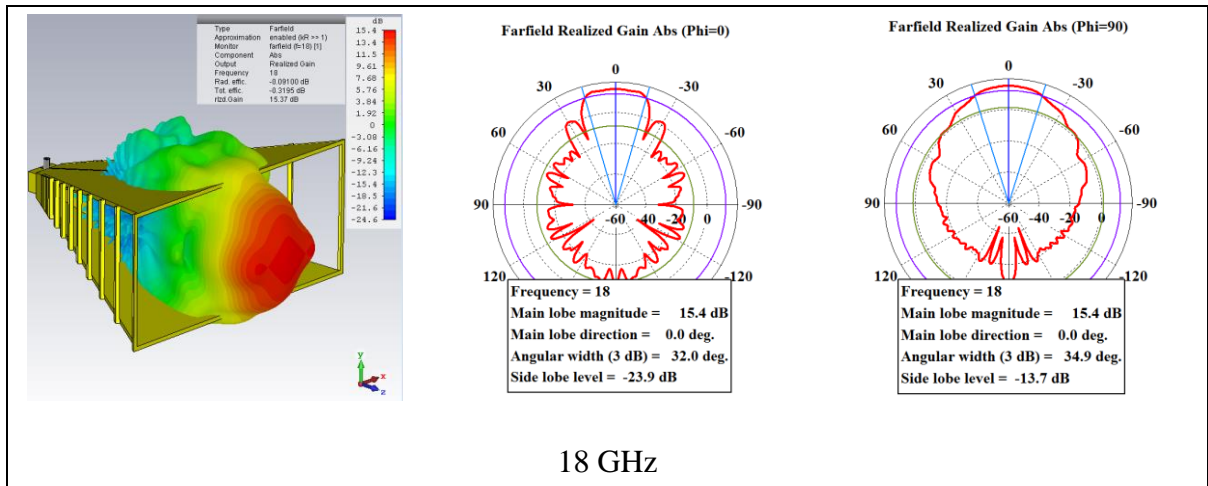

4.5 GHz

10.5 GHz

18 GHz
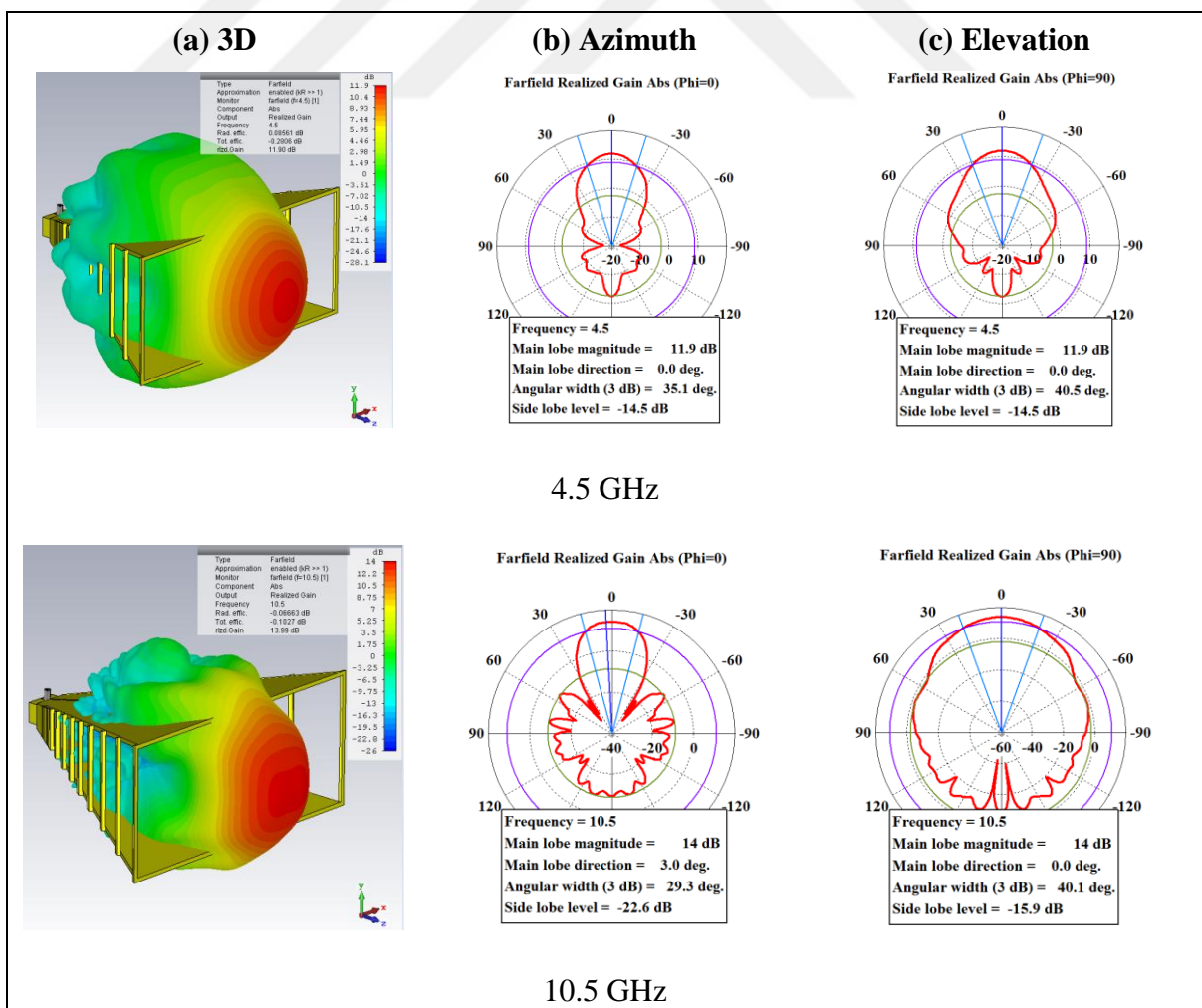
Figure 4.5. 3D, azimuth and elevation simulated far-field radiation patterns of designed modified pinwall coax-fed DRHA
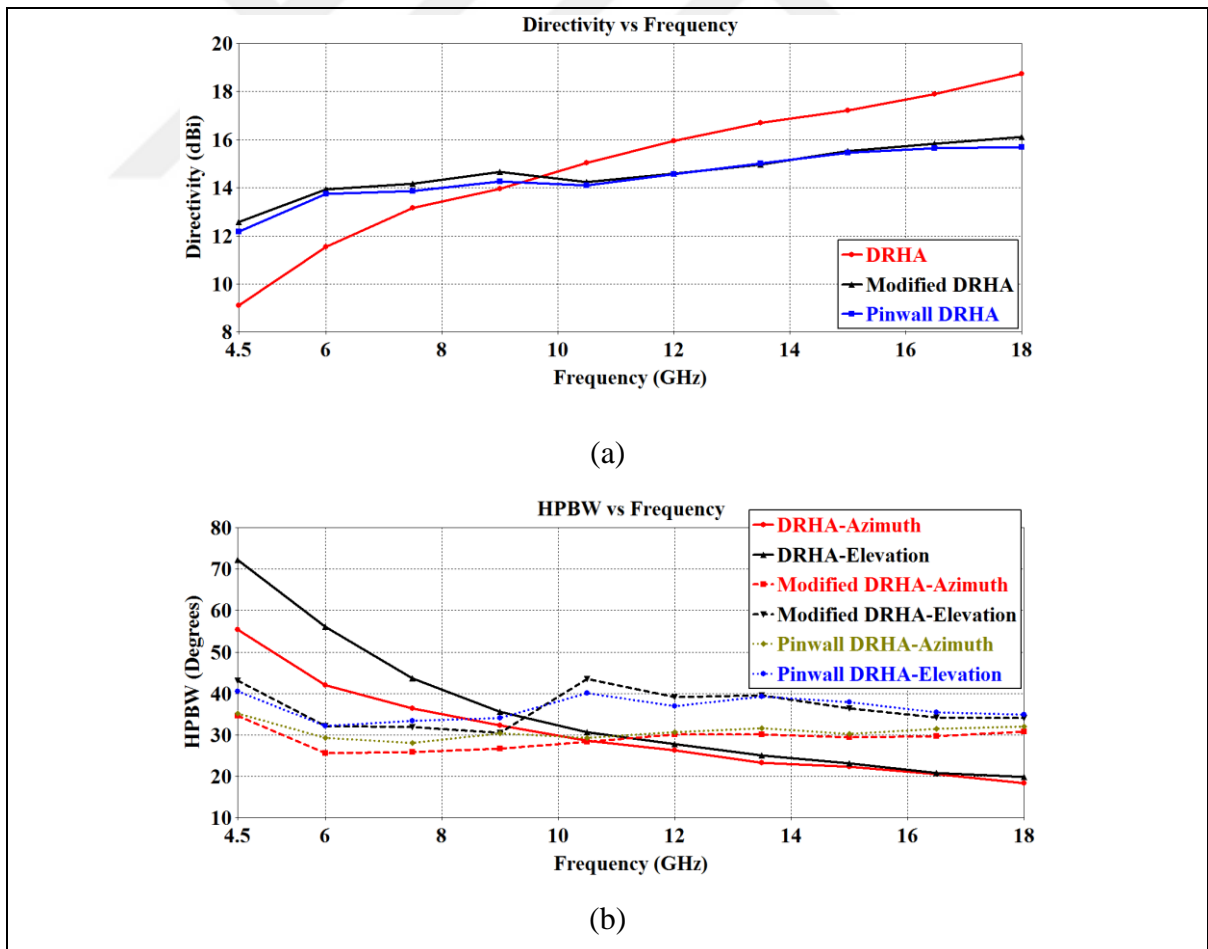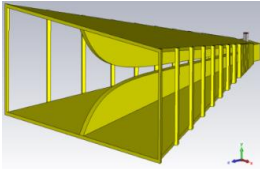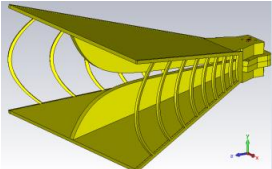

(a)

(b)

Figure 4.6. The comparison of simulated (a) directivity and (b) HPBWs in the E-(elevation) and H-planes (azimuth)

As a summary of this section, first, the width of the aperture where the pins are located is adjusted to achieve the desired beamwidth. The distance between the two pins is half-wavelength of the corresponding frequency. The frequency points are chosen according to number of the pins and this number is determined considering the result of comparisons in the Table 4.3, 4.4 and 4.5. 8 pins are selected after examining the results and the simulations. The arrangement is chosen as a logarithmic instead of linear, so that the distances are equal in per cent, and the pins are placed at these points accordingly.

In addition to this pinwall design, it is possible to make a further improvement in H- plane pattern. The improvement can be made by introducing a curved mouth that ensures the wave-fronts for the short wavelengths radiation are as curved as those of longer ones [49]. However, since the sidewalls are not solid, the pins can be designed as curved instead of straight line.

The simulated model and performance of the curved pinwall antenna is given in Table 4.7. The curved pinwall antenna gives better results in the azimuth radiation pattern and slightly worse results in the elevation pattern in terms of beamwidth constancy. The HPBW variations of straight and curved pinwall antennas are compared in Figure 4.7. However, since we will work on another structure to improve beamwidth constancy in E-plane, we have decided to continue with this curved pinwall design due to its significant development in H-plane. The curved pinwall antenna has perfect azimuth beamwidth constancy with 31.0 ± 1.6 degrees over the whole frequency band 4.5 to 18 GHz.

Table 4.7. The comparison of the parameters of straight and curved pinwall DRHAs

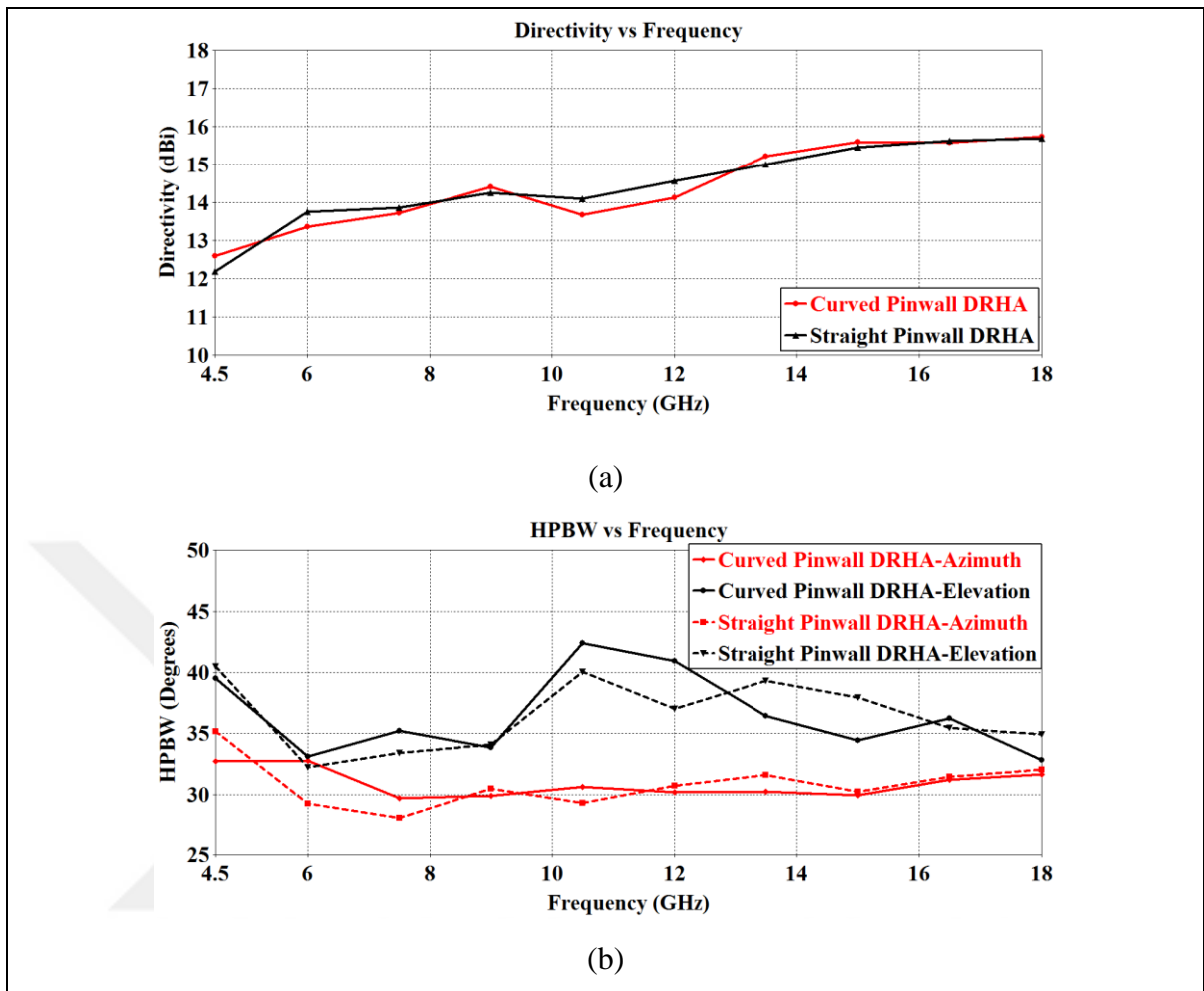|	Straight pinwall	Curved pinwall
Gain (dBi)	11.9 – 15.4	12.2-15.3
HPBW (Azimuth) (Degree)	35.1 – 28.1	32.9 – 29.5
HPBW (Elevation) (Degree)	40.5 – 32.2	42.8 – 32.4

Figure 4.7. The comparison of simulated (a) directivity and (b) HPBWs in the E-
(elevation) and H- (azimuth) planes

Replacing the sidewalls of the flare section parallel to the E-field with conductive pins
produces the H-plane pattern. The lowest frequencies are guided within the pinwalls to the
open end of the horn, but higher frequencies are radiated within the horn only until the
aperture is reached which produces the desired beamwidth and the energy leaks out
between the remaining pins. The flared solid metal walls parallel to the magnetic fields
produce the E-plane pattern. In fact, pinwalls designed with applied progressive conductive
pins produces good results in the elevation pattern as well as azimuth pattern. However,
another structure is needed to have more improvement. It cannot be possible to use pins in
these walls, thus another solution is needed to improve E-plane pattern. This solution will
be examined in the next section which can improve the phase error and pattern beamwidth
constancy.

4.2. CORRUGATED ANTENNA

In this section, a novel structure is presented to improve radiation patterns, especially E-plane pattern for the design of wideband near-constant beamwidth rectangular horn antenna. Therefore, the structure called corrugation which has been known and used to support hybrid modes is used. They are the structures that are designed in a succession of slots and ridges or teethes shown in Figure 4.8.
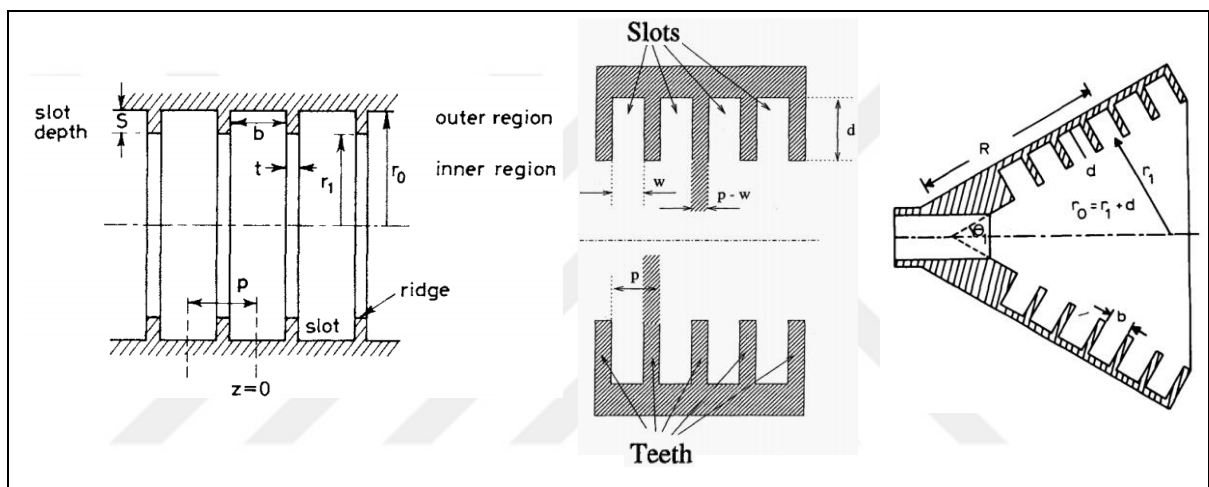

Figure 4.8. Typical corrugation geometries (copied from [60 – 62])

Corrugations are usually applied to cylindrical or conical horns, which have relatively simple boundary conditions due to their axial symmetry. The rectangular corrugated geometries have received less attention because of the difficulty in satisfying the four walls-corrugated boundary conditions. On the other hand, the rectangular corrugated geometries present flexibility because of their radiation pattern variety [63]. The purpose of the corrugated surface is to support the propagation of hybrid modes within the cylindrical horn. Hybrid modes are basically a combination of TE and TM modes. The horn must have anisotropic surface-reactance properties for this combination to provide propagation with a common velocity. Corrugated horns can produce radiation patterns having a characteristic properties such as very good axial symmetry, low cross-polarization levels, low side-lobes, low return loss and high beam efficiency over a 1.5:1 frequency band [13], [60], [64], [65]. These good features come from the balanced-hybrid mode,

HE_{11}. The surface reactance presented by the slots must be capacitive to generate this mode [64], [66]. The corrugated surface inside the antenna produces equal boundary conditions for all polarizations. The resulting pattern is very close to a Gaussian-pattern characteristic that satisfies aforementioned outstanding features [62]. Detailed information and theoretical analysis on corrugated waveguides and antennas are found in many sources [60], [62 – 64], [67 – 72].

We use corrugations only on the top and bottom walls of the flare because the pins were used on the sidewalls of our antenna. Also for the first time with this antenna, the corrugation structure will be used together with the ridges. Indeed, it should be noted that the corrugations has not been used in a pinwall antenna before.

Some of the rules that should be followed generally in the design of corrugations for conventional corrugated horn antennas are summarized as follows [22], [72]:

- Since the diffraction at the edge of the aperture in the H-plane is minimal, the corrugations are generally not placed on the walls of this plane for rectangular horns.

- For smaller flare angles, it is more convenient to open the vertical slots; while for larger angles, the corrugations are placed perpendicular to the surface. However, in general, vertical corrugation formation is preferred due to ease of production.

- Teethes of the corrugations should be as thin as possible and $\lambda/4$ deep. These structures behave as a transmission line that transform a short circuit into an open circuit at the boundary, causing a relatively zero tangential magnetic field.

- The reactance of the corrugated surface used in the walls of a horn antenna must be capacitive to minimize the tangential magnetic field parallel to the wall edges. Such a surface will not support surface waves and will reduce diffraction.

- Slot depths less than $\lambda/4$ generate inductive reactance which results in a propagating surface wave mode. This mode causes high levels of cross polarization.

- Gradual variation from a slot depth $\lambda/2$ to $\lambda/4$ from the waveguide to the aperture can prevent the excitation of surface mode waves.

Note that, the dimensions are given in terms of wavelength in here. Thus, normally corrugated structures can be used in narrowband applications. Some extra structures are needed to expand the useful bandwidth of the corrugations. Different design approaches for broadband corrugated horns were examined in [60], [61], [73]. In most of the designs, a waveguide profile at the lower end of the frequency band was proposed with a slot depth greater than one quarter of the wavelength and less than half the wavelength at the high end to obtain a BW ratio of 2:1 [74 – 76]. More complicated designs were also proposed in the literature to increase the BW of corrugated horns, such as tapered corrugations with a maximum bandwidth of 3:1 [67], a ring-loaded mode converter with a maximum BW ratio of 2.4:1 [60], [61], [74] and a variable slot-to-teeth width mode converter with a maximum BW ratio of 2.05:1 [61]. A corrugated horn antenna with a constant beamwidth over the frequency band from 8 GHz to 18 GHz was presented in [72]. All of the broadband designs mentioned above are quite complex design procedures. Moreover, mechanical complexities, the accuracy and high costs are the other important concerns to be considered. A corrugated structure design that yielded the desired bandwidth more than a ratio of 3:1 is not reported in the open literature to our best knowledge.

The input impedance of the corrugations in conventional corrugated horn antennas is given as follows

$$Z_s = jZ_o \tan(\beta d) \tag{4.5}$$

where, d is a slot depth, Z_o is the characteristic impedance of the slot and β is a propagation constant in the slot. It can be obviously seen that Z_s is continuously capacitive only in the region

$$\lambda/4 < d < \lambda/2 \tag{4.6}$$

due to the cyclic nature of the tangent function which is the reason of narrow bandwidth (less than an octave) of the conventional corrugated horn antennas. It is necessary to design

a slot shape such that Z_s is independent of the tangent function, but dependent of a function that does not change sign every quarter wavelength which makes a corrugated horn with a bandwidth greater than 2:1 possible to overcome the bandwidth limitation.

The input impedance of a line of length d is given by the relation [66]

$$Z_{in} = \frac{AZ_L + B}{CZ_L + D} \qquad (4.7)$$

where, Z_L is the load impedance, A, B, C and D are the transfer matrix parameters which are obtained [66] using Ekstorm's Z-matrix analysis [77] as

$$\begin{bmatrix} A & B \\ C & D \end{bmatrix} = \frac{2(1+md)}{\pi\beta/m} \begin{bmatrix} \frac{1}{1+md}[J_1(a)N_0(b) - J_0(b)N_1(a)] & jZ_{01}[J_1(a)N_1(b) - J_1(b)N_1(a)] \\ \frac{j}{Z_{02}(1+md)}[J_0(a)N_0(b) - J_0(b)N_0(a)] & -[J_0(a)N_1(b) - J_1(b)N_0(a)] \end{bmatrix} \qquad (4.8)$$

where, $a = \beta/m$, $b = \beta/m(1 + md)$, $d =$ length of the transmission line, Z_{01} and Z_{02} are the characteristic impedances at the input and output terminals, respectively. By substituting the (4.8) into the (4.7), Z_{in} becomes as [66]

$$Z_{in} = \frac{Z_{01}Z_{02}}{Z_L} \frac{j + \left(\frac{Z_L}{Z_{02}}\right)ct(a,b)Q(a,b)}{\left(\frac{Z_{02}}{Z_L}\right)Ct(a,b) + jQ(a,b)} \qquad (4.9)$$

where, *ct* and *Ct* are the small and large cotangent radial functions and $Q(a, b)$ is the ratio of the small and large sine radial functions which are used in the analysis of radial transmission lines [14].

For the short circuit, substituting $Z_L = 0$ into the (4.9), the short-circuit input impedance is obtained as

$$Z_{sc} = jZ_{01}\text{Tn}(a, b) \tag{4.10}$$

where, *Tn* is the large radial tangent function. The normalized values of Z_{sc} against b-a are calculated and plotted for different values of b/a in [66]. The case b/a=1 represents the uniform transmission line with m=0 and Tn(a,a) reduces to $\tan(\beta d)$ as in (4.5). As a result, the tapered slots such as b/a=10 will operate over the frequency bandwidth of 3:1. Despite having a theoretical bandwidth of 3:1, the antenna designed in practice due to the limited bandwidth of the ridged waveguide is still 2.4:1. The cross-section of tapered slot corrugation horn used in [66] and its beamwidth characteristics are shown in Figure 4.9.

(a)   (b)
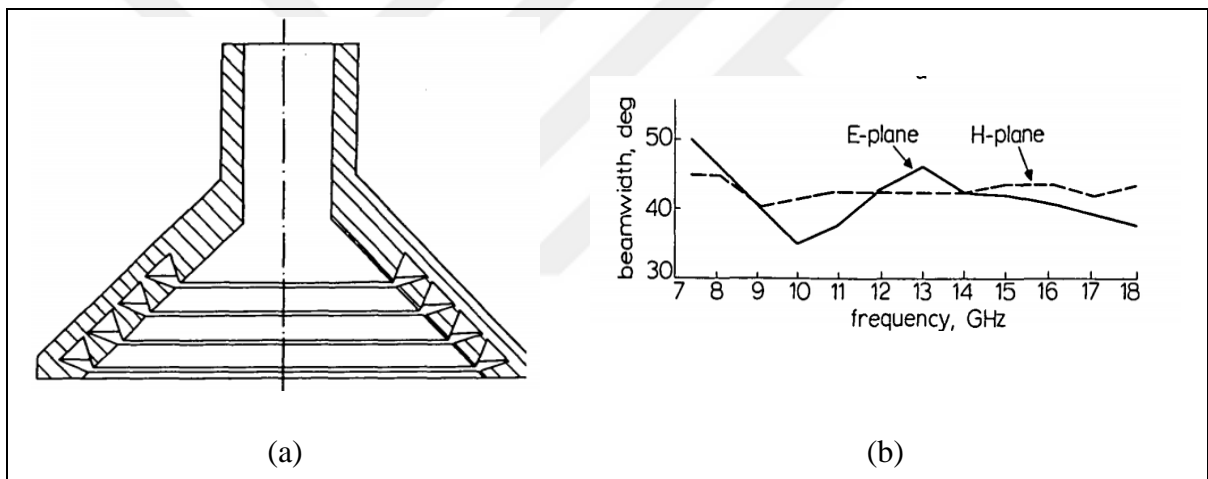
Figure 4.9. (a) Schematic cross-section of tapered slot corrugated horn and (b) beamwidth characteristics of designed antenna in [66]

The geometry of the proposed tapered slot waveguide-fed antenna based on similar theory and geometry explained above is presented in Figure 4.10 and its simulation results are given in 4.11. As can be seen from Figure 4.11, the beamwidth constancy is satisfied when the bandwidth ratio of 3:1 is taken into account, i.e. 6-18 GHz frequency band. However, the result is not particularly good at the beginning of the desired band when the operating frequency band is expanded to more than a ratio of 3:1, specifically 4:1. Therefore, a different corrugation structure design should be designed, which would further improve especially the E-plane radiation pattern.
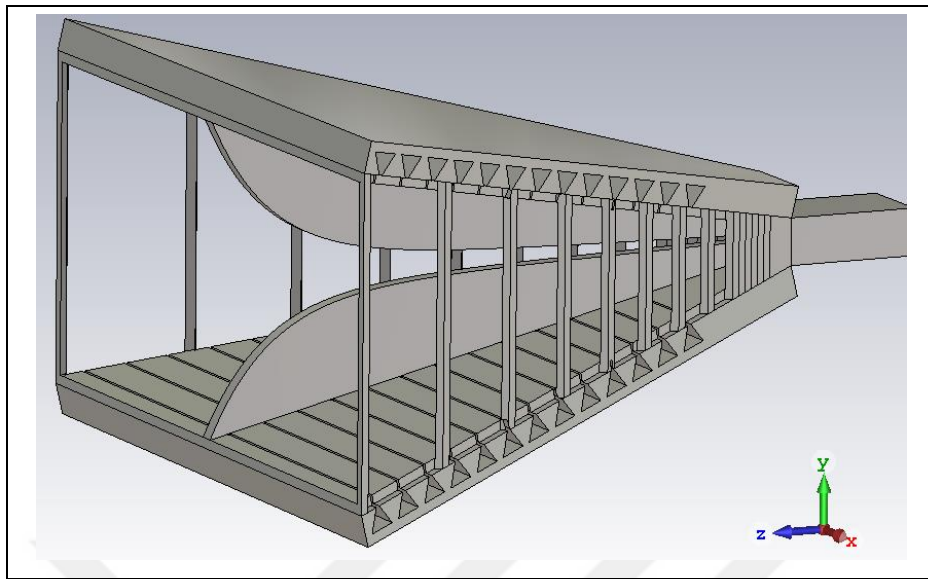
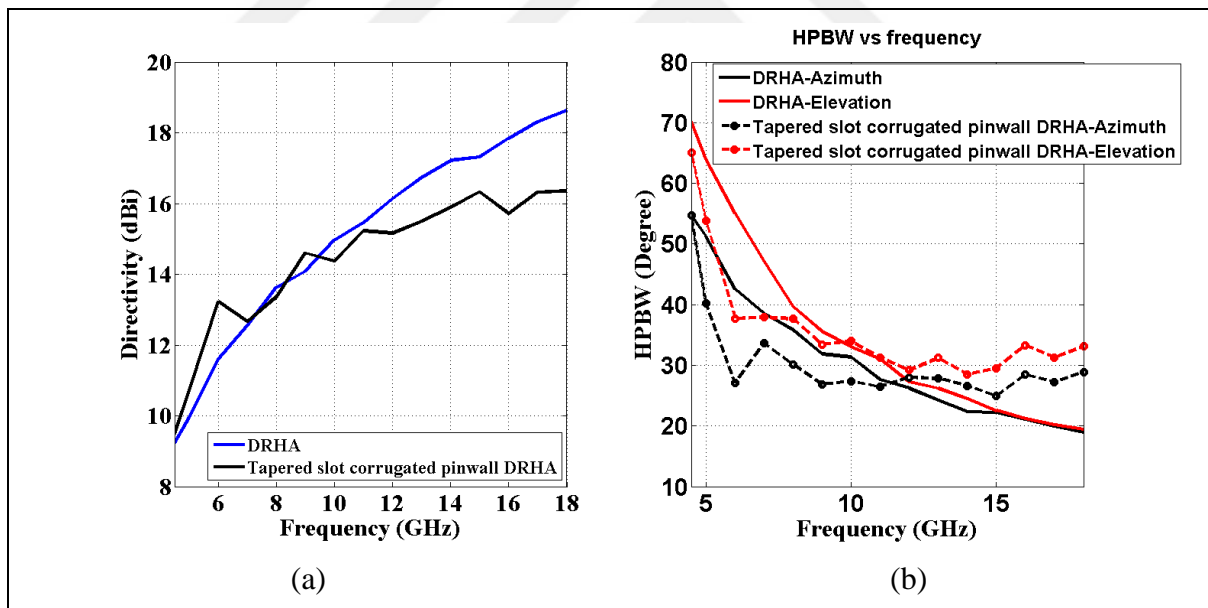Figure 4.10. The simulation model of tapered slot corrugated pinwall DRHA

Figure 4.11. The simulated (a) directivity and (b) HPBW results of tapered slot corrugated pinwall DRHA

Ring-loaded corrugation structure is another option to broaden the useful frequency bandwidth of corrugated waveguides and horns. A precise analysis of the RLCW was made for circular waveguides [78]. The field components of RLCW and the field distribution of the ring-loaded corrugated horns with small flare angle were derived in [78].

Consequently, the useful frequency bandwidth was broadened 1.35 times than that in the conventional corrugated horns which had a bandwidth of 2.55:1 by keeping the slot admittance capacitive over an extended bandwidth by ring-loaded structure.

If the corrugated surface is suitable, then the antenna is capable of propagating hybrid modes which means that the aperture field distribution previously considered in determination of the H-plane dimensions can also be considered with a similar process to be implemented for E-plane dimensions, i.e. aperture height. Our antenna is more wideband when it is compared with the one given in [78]. Additionally, it is double ridged horn, so aperture taper cannot be only determinant in this matter. Ridge profile is at least as important as aperture taper. Thus, the procedure applied for the determination of H-plane dimensions at the beginning of the pinwall antenna section, cannot be used to find aperture height. However, if the wideband corrugation design is achieved for desired frequency band, then these structures are used to improve the elevation pattern.

Use of simple conventional rectangular slots is restricted to octave bandwidth. The application of the "L-shaped" slots to the E-plane walls is thought to be adaptation of ring-loaded corrugations to the rectangular horn antenna [58]. This slot may be considered as a combination of two rectangular slots that one slot with a depth d_1 and width w_1 and loaded by another slot of depth d_2 and width w_2. The form can also be in a different shape such as "T-shaped". This change does not affect the theory, but it can provide ease of manufacture (Figure 4.12).
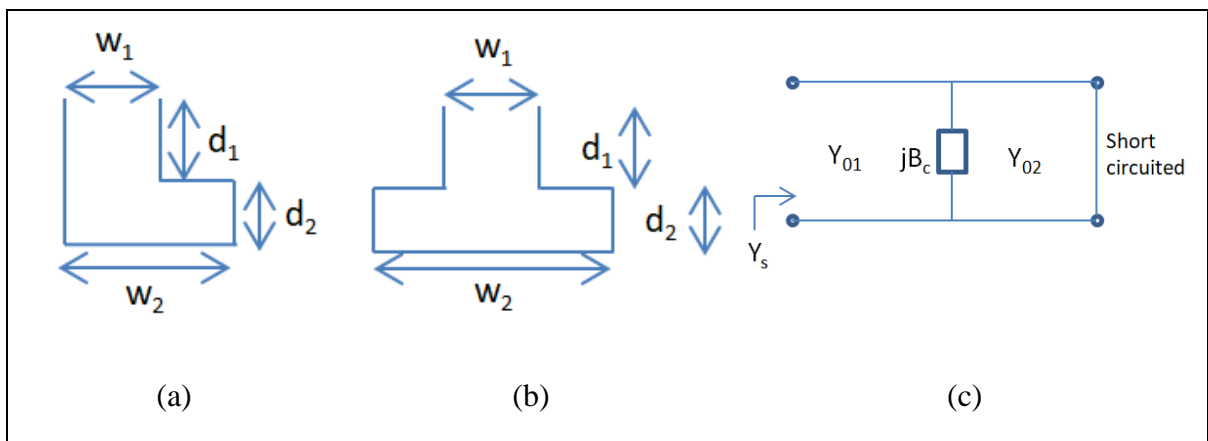

Figure 4.12. (a) L-shaped slot (b) T-shaped slot (c) Equivalent circuit

The input admittance of the slot was calculated using the equivalent circuit shown in Figure 4.12-(c). Y_{01}, Y_{02}, Y_s represent the characteristic admittance of the upper section, the characteristic admittance of the lower section and the slot input admittance respectively. B_c is a susceptance to represent the step discontinuity between slot sections. Applying transmission line theory to the equivalent circuit and using rectangular waveguide step model given in [78], the slot line input admittance parameter was derived as

$$\frac{Y_s}{Y_{01}} = j\frac{[Y_{01}\tan(2\pi d_1/\lambda_s)tan\left(\frac{2\pi d_2}{\lambda_s}\right)-Y_{02}-B_c\tan(2\pi d_2/\lambda_s)]}{\left[Y_{01}\,tan\left(\frac{2\pi d_2}{\lambda_s}\right)+Y_{02}tan(2\pi d_1/\lambda_s\,)+B_c\,tan(2\pi d_1/\lambda_s)\tan(2\pi d_2/\lambda_s)\right]} \tag{4.11}$$

where,

$$Y_{02} = Y_{01}\frac{w_1}{w_2} \tag{4.12}$$

λ_s is the wavelength in the slot section that is presented by

$$\lambda_s = \frac{2b\lambda}{(4b^2-\lambda^2)^{0.5}} \tag{4.13}$$

b is a transverse slot length and the step discontinuity susceptance, B_c, for the TE_{10} mode is given as

$$B_c = -\frac{2w_2Y_{02}}{\lambda_s}\left[ln\left\{\left(\frac{1-\alpha^2}{4\alpha}\right)\left(\frac{1+\alpha}{1-\alpha}\right)^{0.5\left(\alpha+\frac{1}{\alpha}\right)}\right\}+\frac{2}{Q}\right],\alpha<1 \tag{4.14}$$

where,

$$\alpha = w_1/w_2 \tag{4.15}$$

$$Q = \left(\frac{1+\alpha}{1-\alpha}\right)^{2\alpha} \left[\frac{1+\{1-(w_2/\lambda_s)^2\}^{0.5}}{1-\{1-(w_2/\lambda_s)^2\}^{0.5}}\right] - \frac{(1+3\alpha^2)}{(1-\alpha^2)} \tag{4.16}$$

For $\alpha > 1$, B_c is given by replacing w_2 by w_1.

The T-shaped corrugation design of the E-plane walls of the corrugated horn antenna with a BW ratio of 2.4:1 was implemented using these equations and the principle that the width of the slots must be about one tenth of the wavelength which the detailed design process could be accessed from the study in [58]. However, our desired frequency range is still not reached.

Therefore, a new corrugation design called "stepped-shape" is planned with the addition of one more section shown in Figure 4.13 to expand the frequency band in a similar manner.

In the final version, the slot input admittance Y_{in} is obtained using transmission line theory in terms of the input admittance of T-shaped corrugation equivalent circuit with a notation used in Figure 4.13 as

$$\frac{Y_{in}}{Y_{01}} = \frac{Y_L + jY_{01}\tan(2\pi d_1/\lambda_s)}{Y_{01} + jY_L\tan(2\pi d_1/\lambda_s)} \tag{4.17}$$

and

$$Y_{02} = Y_{01}\frac{w_1}{w_2} = Y_{03}\frac{w_1}{w_3} \tag{4.18}$$

where, Y_{01}, Y_{02}, Y_{03} are the characteristic admittances; w_1, w_2, w_3 are the widths of the slot sections respectively, Y_L is the input admittance while looking the circuit just before the top section including the step discontinuity between the top and middle sections, B_{c1}, and Y_s is the input slot admittance of the bottom 2 sections which is given in (4.11).
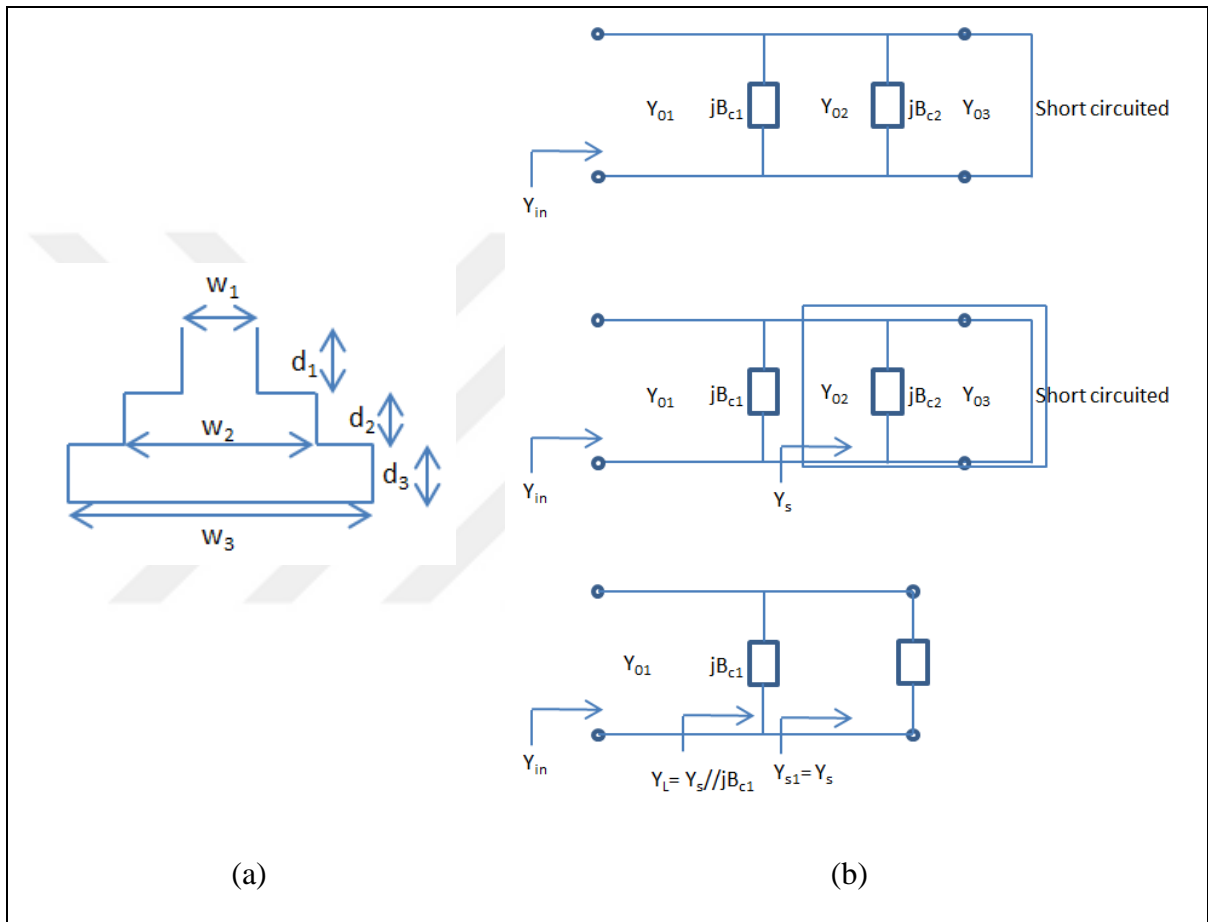

Figure 4.13. (a) Stepped-shape slot (b) Equivalent circuits in progressive steps

It should be noted that the indices of the parameters used in (4.11), (4.12) and (4.14) should be changed from 01 to 02, 02 to 03 which correspond to the following equations

$$B_{c2} = -\frac{2w_3 Y_{03}}{\lambda_s}\left[ln\left\{\left(\frac{1-\alpha_2{}^2}{4\alpha_2}\right)\left(\frac{1+\alpha_2}{1-\alpha_2}\right)^{0.5\left(\alpha_2+\frac{1}{\alpha_2}\right)}\right\} + \frac{2}{Q_2}\right], \alpha_2 < 1 \qquad (4.19)$$

$$Q_2 = \left(\frac{1+\alpha_2}{1-\alpha_2}\right)^{2\alpha_2} \left[\frac{1+\{1-(w_3/\lambda_s)^2\}^{0.5}}{1-\{1-(w_3/\lambda_s)^2\}^{0.5}}\right] - \frac{(1+3\alpha_2{}^2)}{(1-\alpha_2{}^2)} \tag{4.20}$$

$$\alpha_2 = w_2/w_3 \tag{4.21}$$

And (4.17) is derived as follows

$$\frac{Y_{in}}{Y_{01}} = \frac{jB_{c1}+Y_sY_{02}+jY_{01}\tan(2\pi d_1/\lambda_s)}{Y_{01}+j(jB_{c1}+Y_sY_{02})\tan(2\pi d_1/\lambda_s)} \tag{4.22}$$

$$= \frac{jB_{c1}+Y_sY_{02}+jY_{01}\tan(2\pi d_1/\lambda_s)}{Y_{01}-B_{c1}\tan(2\pi d_1/\lambda_s)+jY_sY_{02}\tan(2\pi d_1/\lambda_s)} \tag{4.23}$$

$$= \frac{jB_{c1}+Y_{02}j\frac{[Y_{02}\tan(2\pi d_2/\lambda_s)tan\left(\frac{2\pi d_3}{\lambda_s}\right)-Y_{03}-B_{c2}\tan(2\pi d_3/\lambda_s)]}{\left[Y_{02}\tan\left(\frac{2\pi d_3}{\lambda_s}\right)+Y_{03}tan(2\pi d_2/\lambda_s)+B_{c2}\tan(2\pi d_2/\lambda_s)\tan(2\pi d_3/\lambda_s)\right]}+jY_{01}\tan(2\pi d_1/\lambda_s)}{Y_{01}-B_{c1}\tan(2\pi d_1/\lambda_s)+j\frac{[Y_{02}\tan(2\pi d_2/\lambda_s)tan\left(\frac{2\pi d_3}{\lambda_s}\right)-Y_{03}-B_{c2}\tan(2\pi d_3/\lambda_s)]}{\left[Y_{02}\tan\left(\frac{2\pi d_3}{\lambda_s}\right)+Y_{03}tan(2\pi d_2/\lambda_s)+B_{c2}\tan(2\pi d_2/\lambda_s)\tan(2\pi d_3/\lambda_s)\right]}Y_{02}\tan(2\pi d_1/\lambda_s)} \tag{4.24}$$

where, B_{c1} represents the step discontinuity with the slot sections 1 and 2, which has the same equation with B_{c2} replacing w_3 by w_2, Y_{03} by Y_{02}, α_2 by α, and Q_2 by Q in (4.19). α and Q parameters are given in (4.20) and (4.21).

A top section width of $w_1 = 0.75$mm was chosen which is approximately $\lambda_{max}/20$ at higher end of the frequency band for the slot design with a new structure called "stepped-shape slot". Equation (4.24) is used to compute Y_{in} for different total slot depths $d_1+d_2+d_3$ and for each slot depth d_2, d_3, w_2, w_3 are varied independently to maximize the capacitive region over the band. The important issue in here is the total depth is $\lambda_0/4$ at midband frequencies corresponding to the range $8.5 - 9$ mm, that is about the total length required.

It is found that Y_{in} can be at capacitive region over the band by suitable combination of the parameters d_2, d_3, w_2, w_3 for each slot depth. In addition, since the result obtained from [66], the tapered slots having a ratio of b/a=10 can operate over the frequency bandwidth of 3:1, w_3 was chosen as approximately $10 - 12$ times w_1 that corresponded to interval $7 - 9$ mm. Figure 4.14 shows the variation of Y_{in}/Y_{01} over the frequency band ratio of 6:1 (4.5 $- 27$ GHz) for the chosen slot parameters and for different transverse lengths used in the E-plane wall design. It can be seen from the Figure 4.14, while the T-shaped corrugation designed in the article [58] had a ratio of approximately 2.4:1, the novel stepped-shape slot we designed can perform a capacitive effect along the desired frequency band (4.5 GHz – 18 GHz). Another important point is the distance between corrugations. This spacing was determined by mechanical and manufacturing considerations of the distance between the bottom sections of adjacent slots. The distance between the centers of two adjacent lower sections was 15.4 mm (wall thickness between them 5.9 mm).
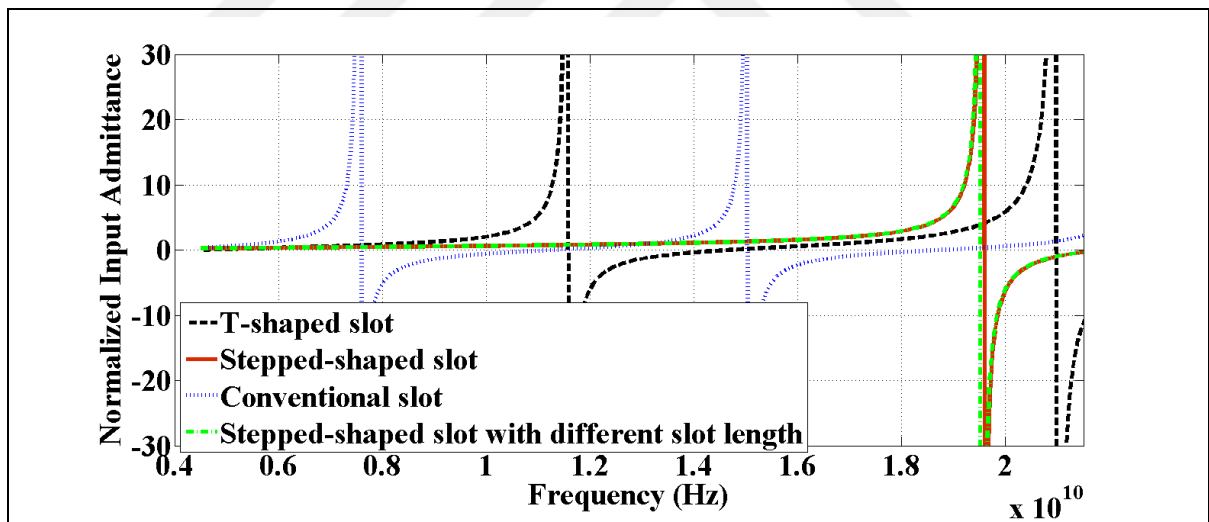
Figure 4.14. Normalized input admittances for different type of corrugations along the frequency band: 4.5 – 22 GHz

In Figure 4.14, the red and green lines are displayed using the determined slot dimension parameters of stepped-shape slot: d_1=2.5mm, d_2=3.5mm, d_3=3.5mm, w_1=0.75mm, w_2=5mm, w_3=8.5mm with different transverse lengths b= $2.5\lambda_0$ and b=$7.5\lambda_0$, respectively. It is obvious that the transverse lengths do not practically affect the capacitive region. As it

is demonstrated that the capacitive band limits do not depend on the transverse slot lengths, the length of the corrugations applied to the E- plane walls are adjusted to have the same length with flare width except ridge thickness considering the manufacturing process. The blue line represents the conventional slot with dimensions obtained according to the following equations. The conventional slot parameters are taken as $w = 0.075\lambda_0$ and $d = 0.3\lambda_0$

$$w < \frac{\lambda_0}{10} \tag{4.25}$$

With a condition (4.26)

$$\lambda_0/4 < d < \lambda_0/2 \tag{4.26}$$

The input slot admittance is found as follows

$$Y_{in-conventional} = -j\frac{1}{\tan\left(2\pi\frac{d}{\lambda_s}\right)} \tag{4.27}$$

The black line in Figure 4.14 is plotted for T-shaped slot with dimensions found in [58]. Our results also support the results of the study given in [58] and it can be noticed that the T-shaped slot only provides a bandwidth ratio of about 2.4:1. On the other hand, a novel designed geometry called stepped-shape slot satisfies wider frequency band which included approximately 4.5 – 19 GHz. In this band, this corrugation keeps the slot admittance capacitive by the addition of third section.

A reasonable corrugated wall length is determined to obtain best radiation pattern and VSWR parameter. Various numbers of slots were placed within this wall length, and the radiation pattern results were examined and optimum results in terms of beamwidth

constancy were obtained. In addition, having a smooth plane before the corrugations started at the beginning of the flare, has a positive effect on the VSWR parameter and elevation radiation patterns. According to the analysis, we have decided to use 4 stepped-shape slots. Another section called "shaped-flare" is designed on the E-plane wall and it is added beyond the corrugated and smooth plane. This section will provide the throat aperture to improve impedance matching especially at high-end points of the frequency band.

The simulation model obtained according to the design process and dimensions described in detail above is given in Figure 4.15. The VSWR parameter and the far-field radiation patterns according to the simulation results are given in Figure 4.16 and Figure 4.17.

(a)

(b)

(c)

(d)
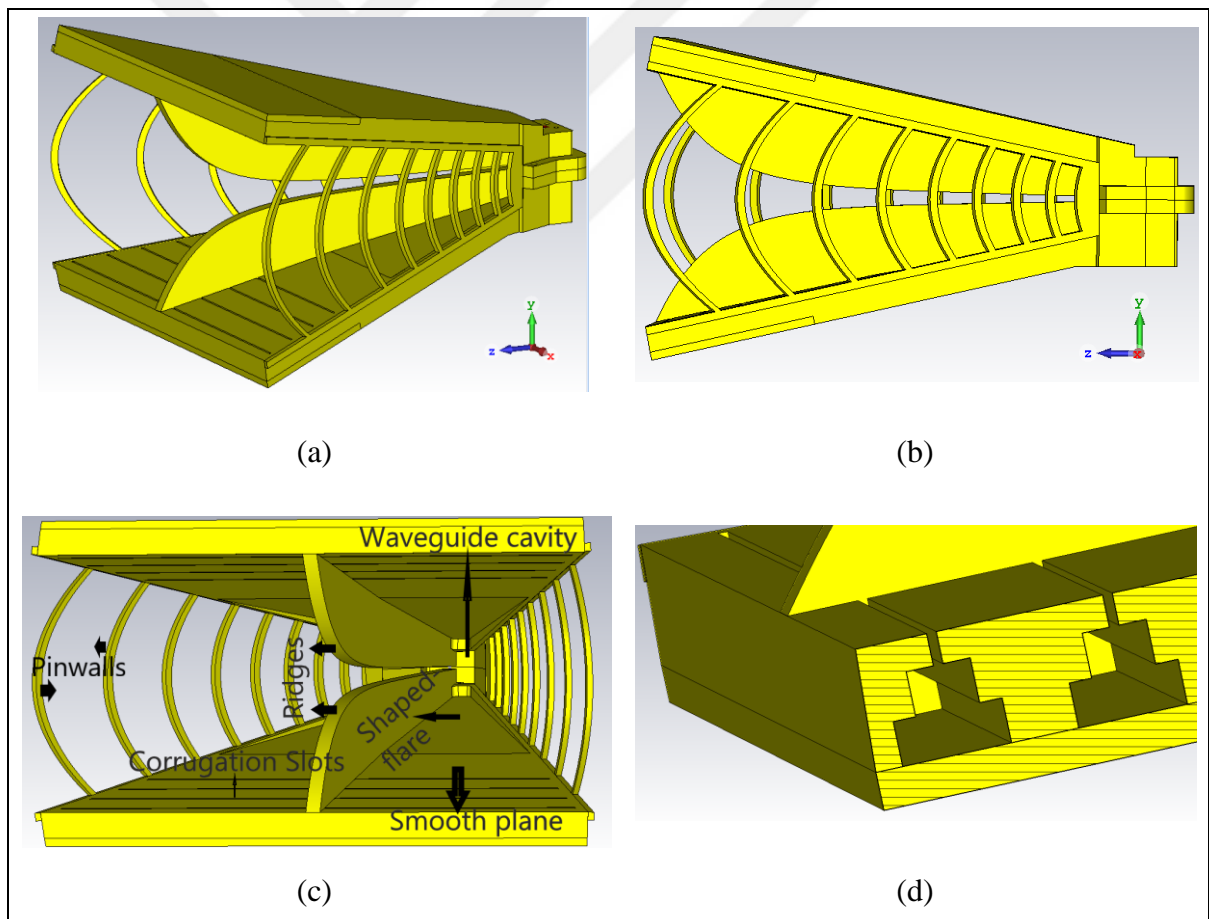
Figure 4.15. (a) Perspective (b) side (c) front view of the designed curved pinwall corrugated shaped-flare DRHA (NCBWHA) and (d) cross-section of stepped-shape slots
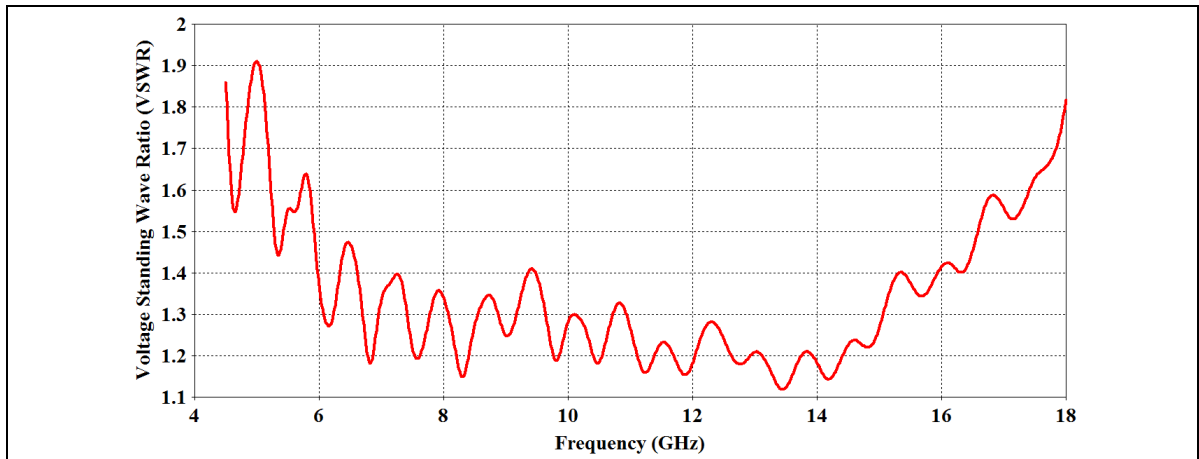
Figure 4.16. The simulated VSWR of NCBWHA

(a) 3D	(b) Azimuth	(c) Elevation

4.5 GHz

10.5 GHz
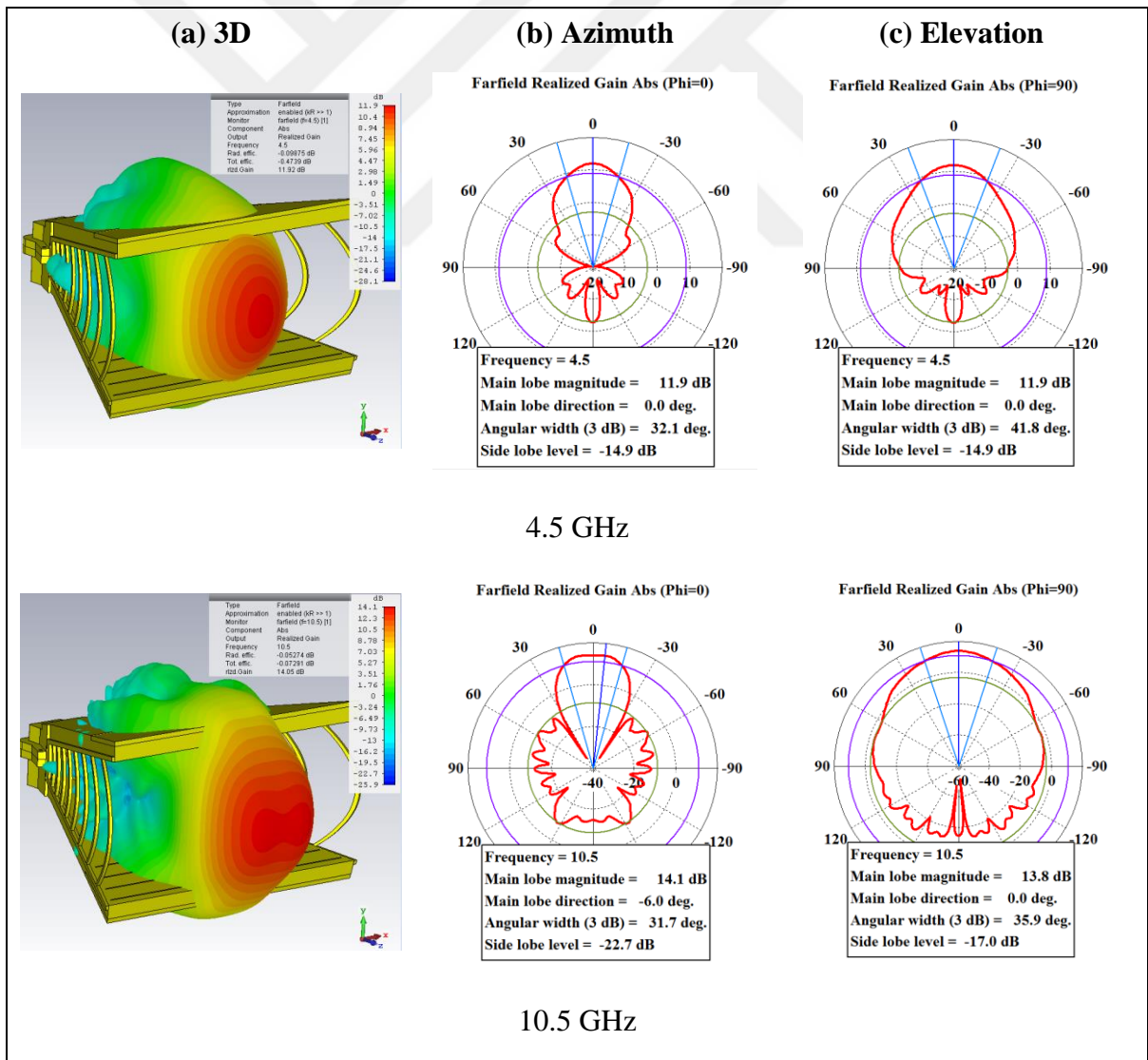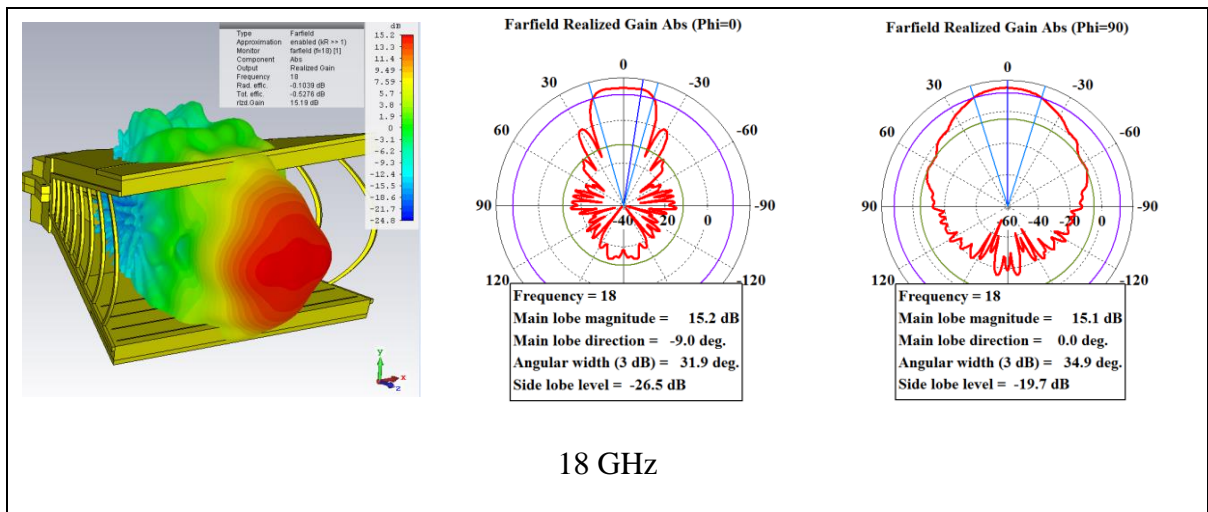
Figure 4.17. The simulated 3D, azimuth and elevation co-polarized far-field radiation patterns of NCBWHA

The directivity and azimuth-elevation beamwidth variation are given and they are compared with previously designed DRHA in Figure 4.18.

NCBWHA is a highly improved antenna in terms of the phase center variation compared to conventional DRHA given in Chapter 3. The phase center changes approximately 15 mm between the ends of the frequency bands. This value was 35 mm for conventional DRHA and 80 mm for log-periodic antenna.

(a)
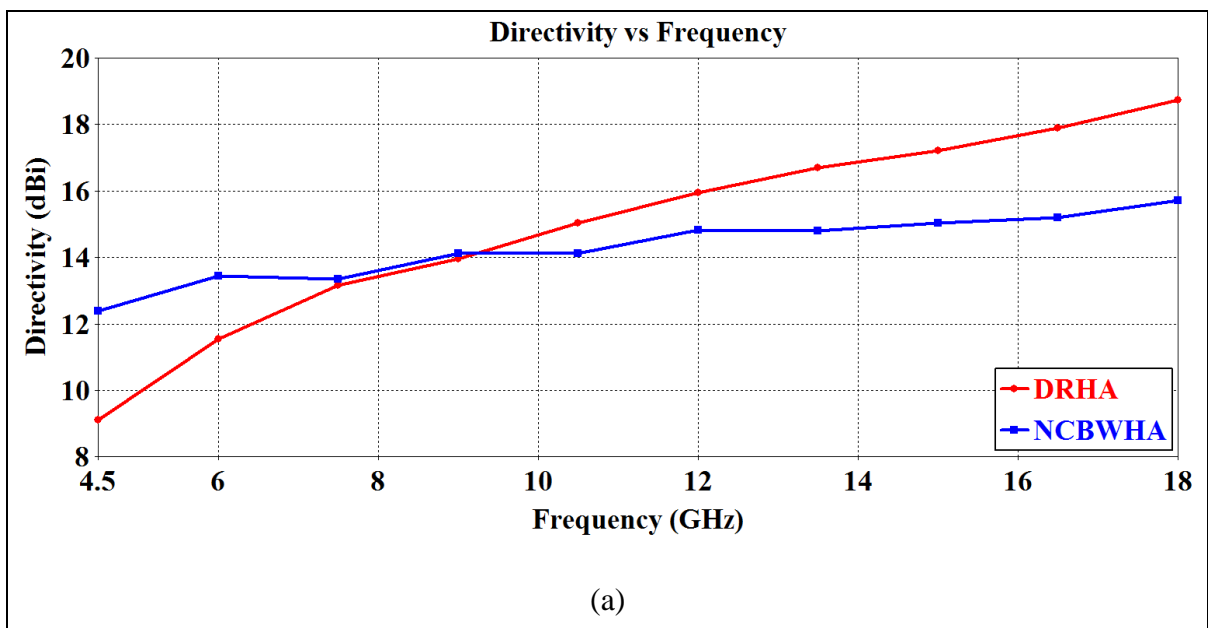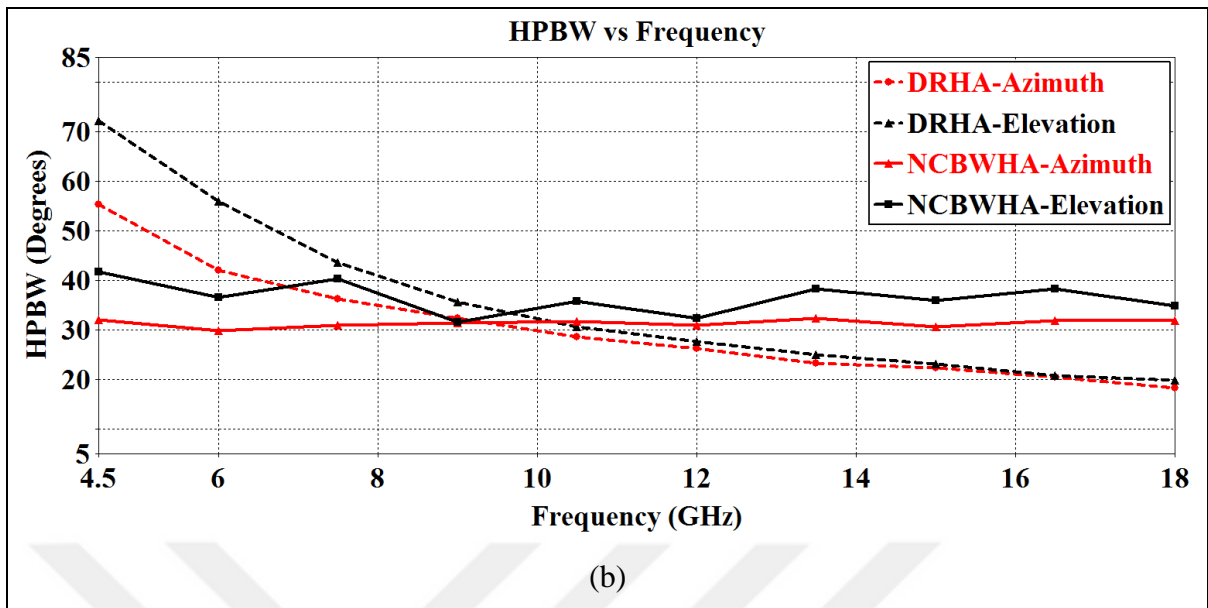
Figure 4.18. The comparison of simulated (a) directivity and (b) HPBWs in the E- and H-planes of DRHA and NCBWHA

5. ANTENNA MEASUREMENTS

Following successful simulation results, the production files of the designed antennas (coax-fed curved pinwall DRHA and NCBWHA) are prepared and the antennas are produced. The details of the production ready views are given in Appendix A and Appendix B. The manufactured curved pinwall antenna and NCBWHA are presented in Figure 5.1 and Figure 5.2, respectively.

(a)

(b)

(c)

(d)
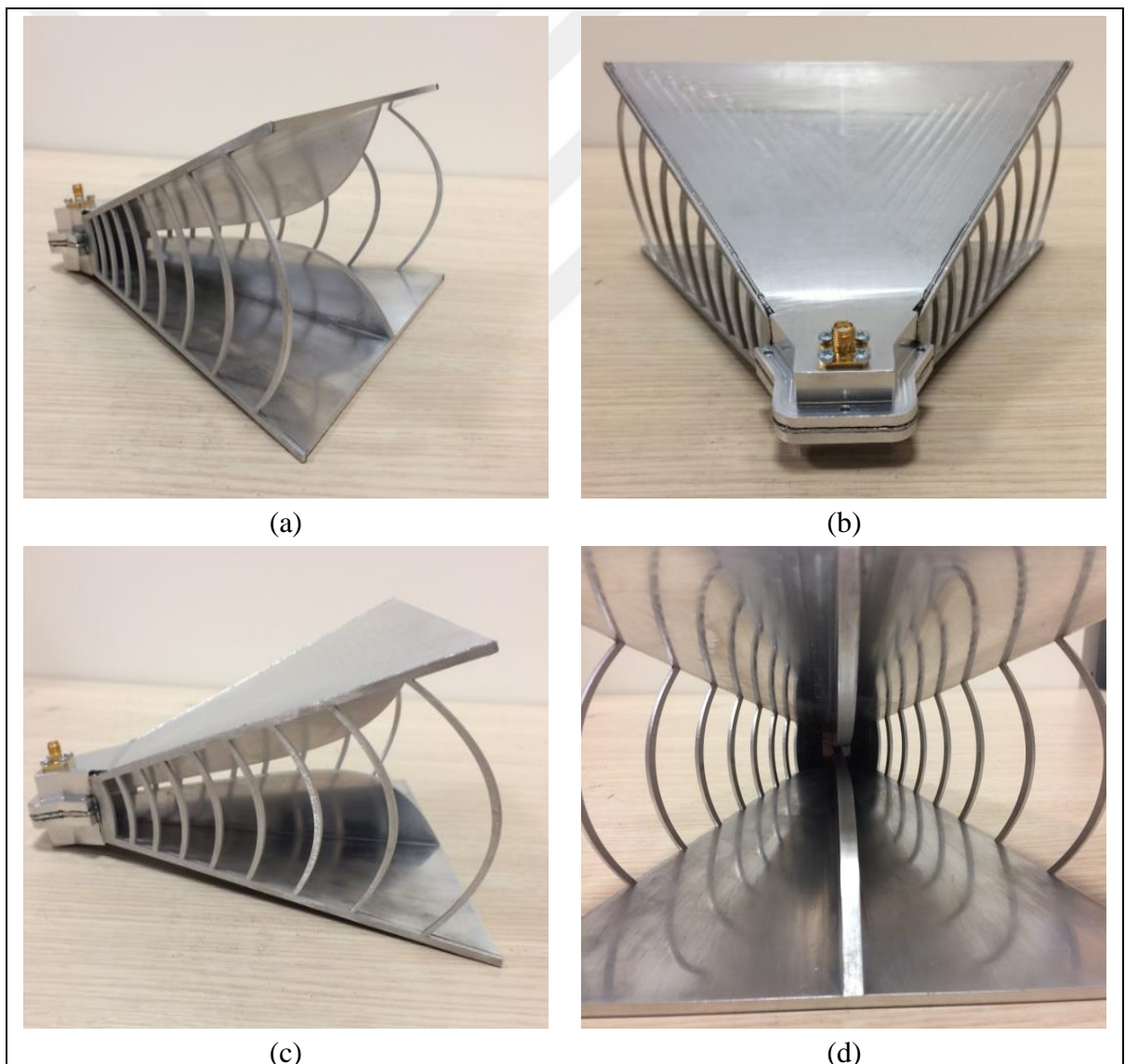
Figure 5.1. Different views of the manufactured coax-fed curved pinwall DRHA
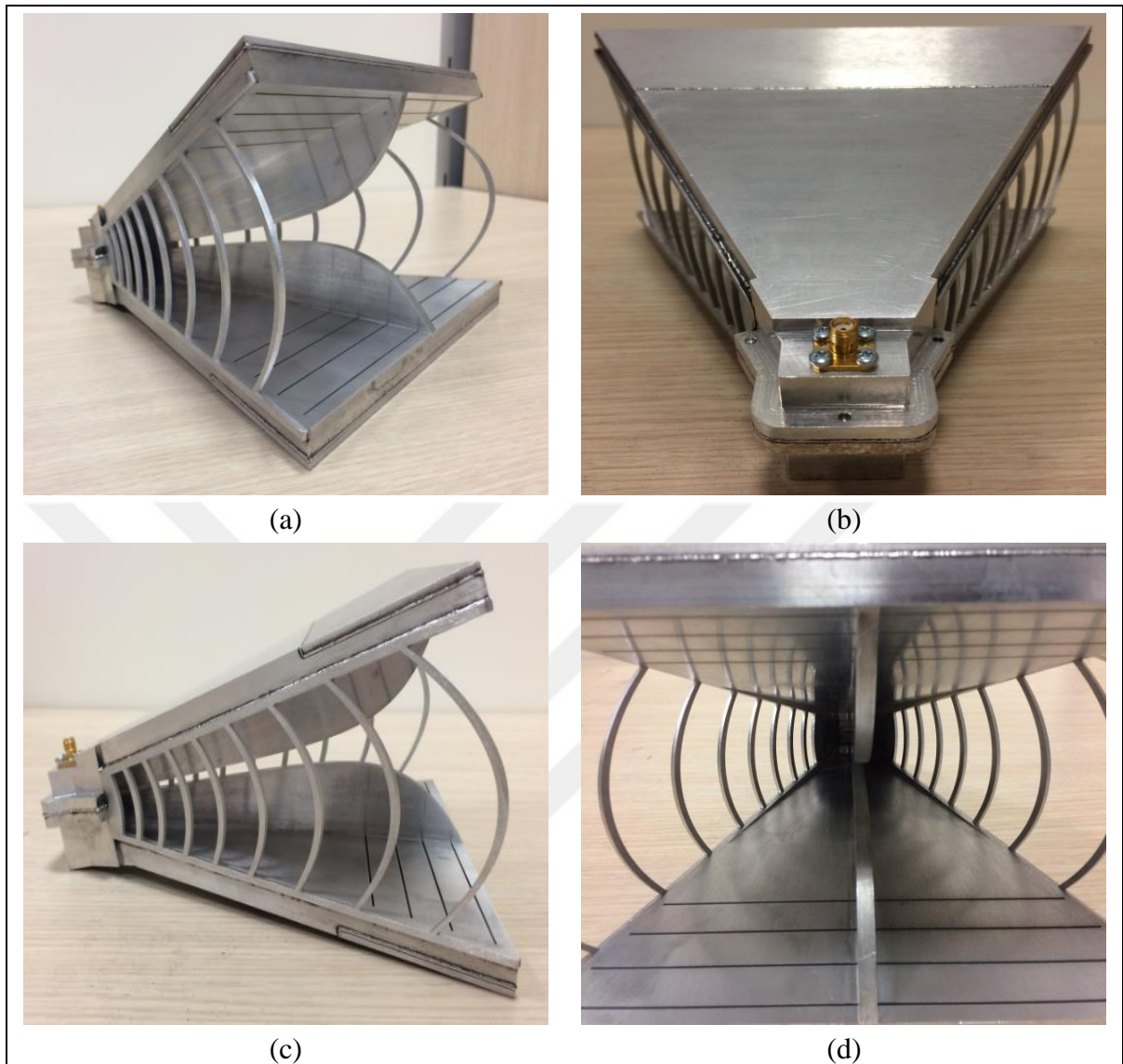
Figure 5.2. Different views of the manufactured coax-fed NCBWHA

The measurements of radiation patterns were performed in an anechoic chamber using the commercially available Spherical Near-Field (SNF) measurement system at TUBITAK, BILGEM, ATAM. The anechoic chamber is shown in Figure 5.3 and the specifications of the SNF measurement system at TUBITAK are given in Table 5.1. Near-field methods allow determining the complete characterization of the antenna performance that includes the antenna gain, 2D-3D radiation patterns, and polarization measurements with high accuracy.
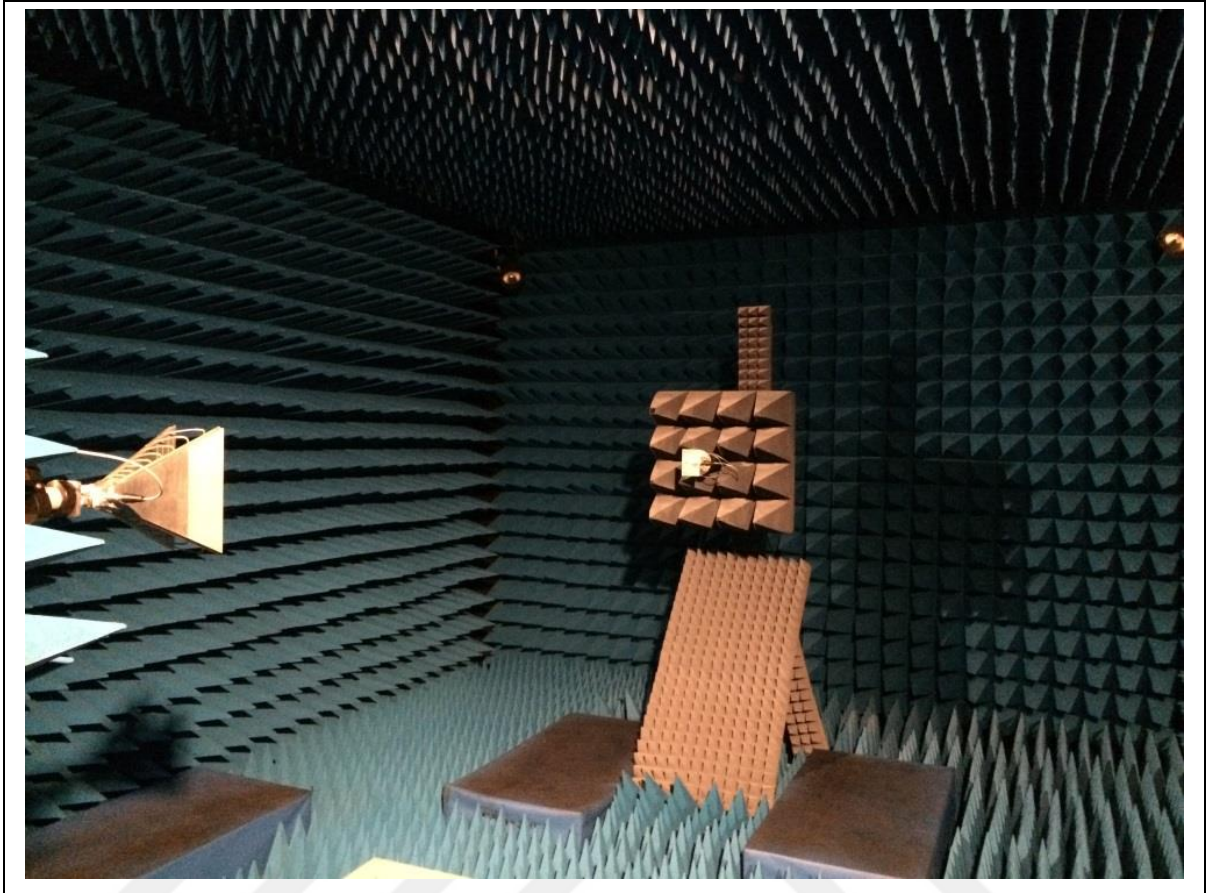
Figure 5.3. Anechoic chamber

Table 5.1. The specifications of the SNF measurement system

Parameters	SNF Measurement System
Chamber Dimensions (m) (L x W x H)	7.5 x 4.7 x 3.3
Maximum dimension of antenna under test (AUT) (m)	1.5
Maximum weight of AUT (kg)	75
Scanning type	Spherical
Frequency range (GHz)	0.75 – 40

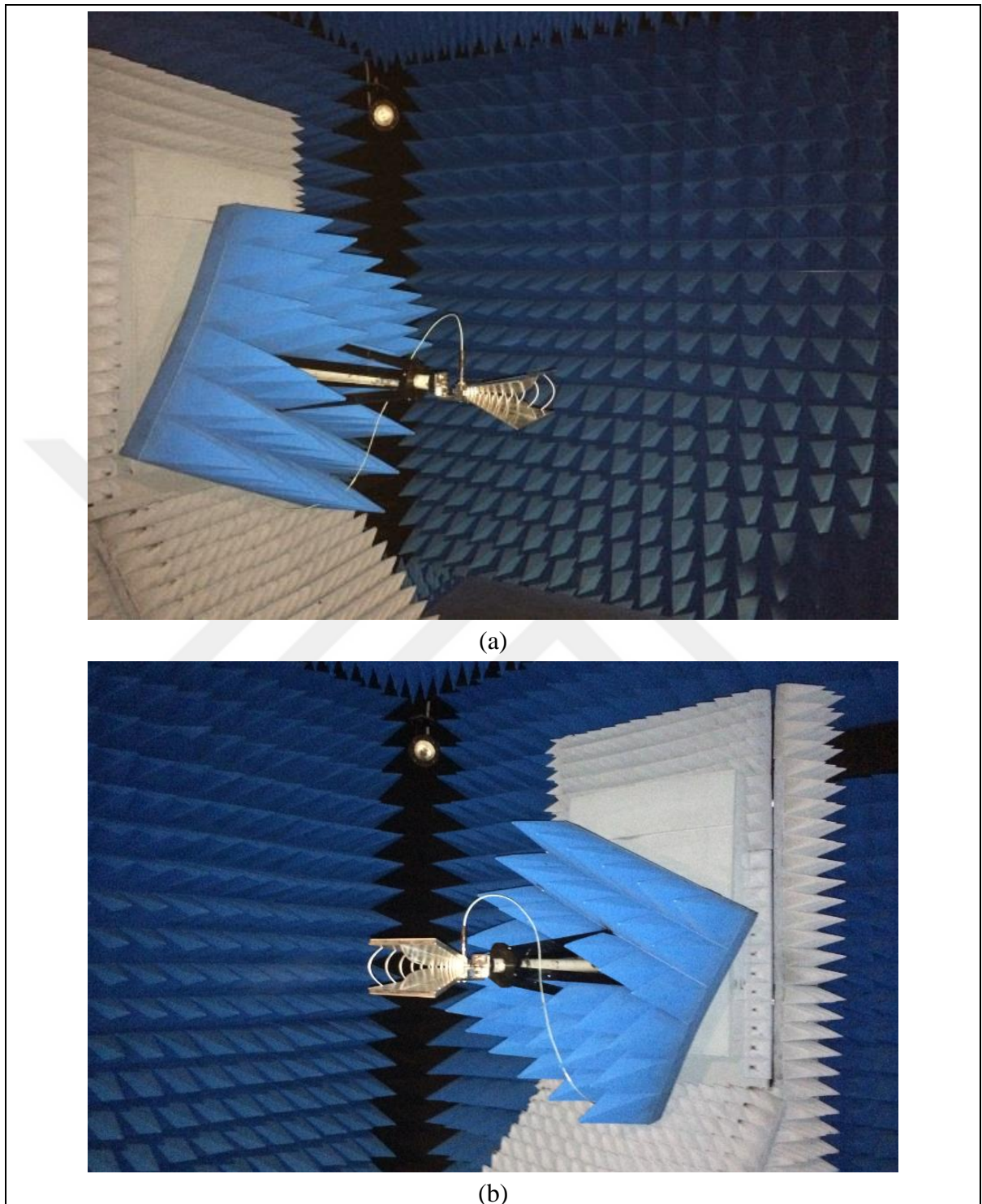3D, 2D radiation patterns and antenna gain are measured in SNF system. Antennas under test are given in Figure 5.4.

(a)

(b)

Figure 5.4. (a) Coax-fed curved pinwall DRHA (b) NCBWHA under test in anechoic chamber

Initially, the simulation and measurement results of the manufactured antennas are compared for 3 different frequency points that indicate the beginning (4.5 GHz), center

(11.25 GHz) and end (18 GHz) of the band to check the accuracy of the simulations and how the production matched the design.
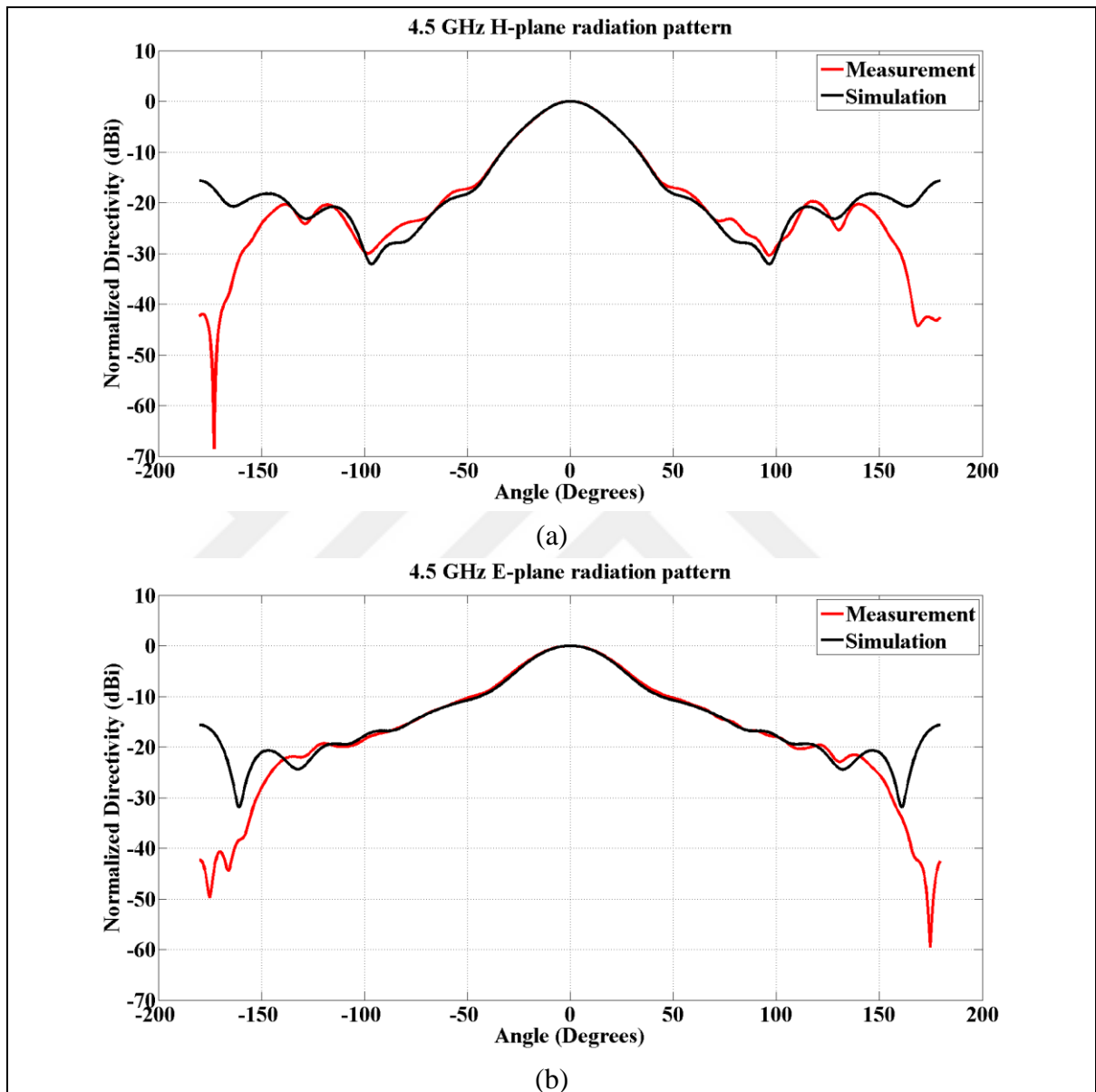

Figure 5.5. The comparison of simulated and measured 4.5 GHz radiation patterns of coax-fed curved pinwall DRHA (a) H-plane (Azimuth) (b) E-plane (Elevation)
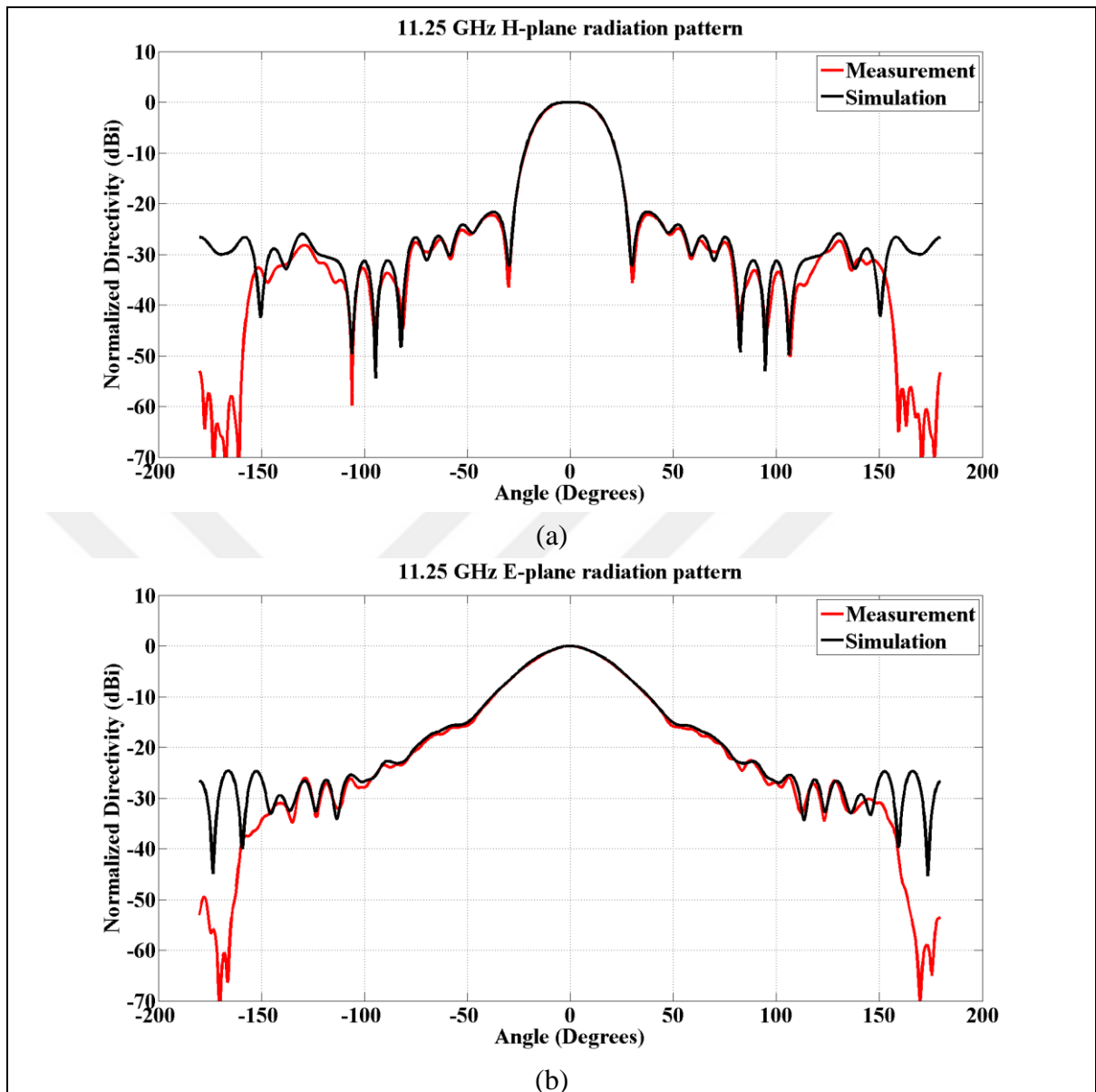
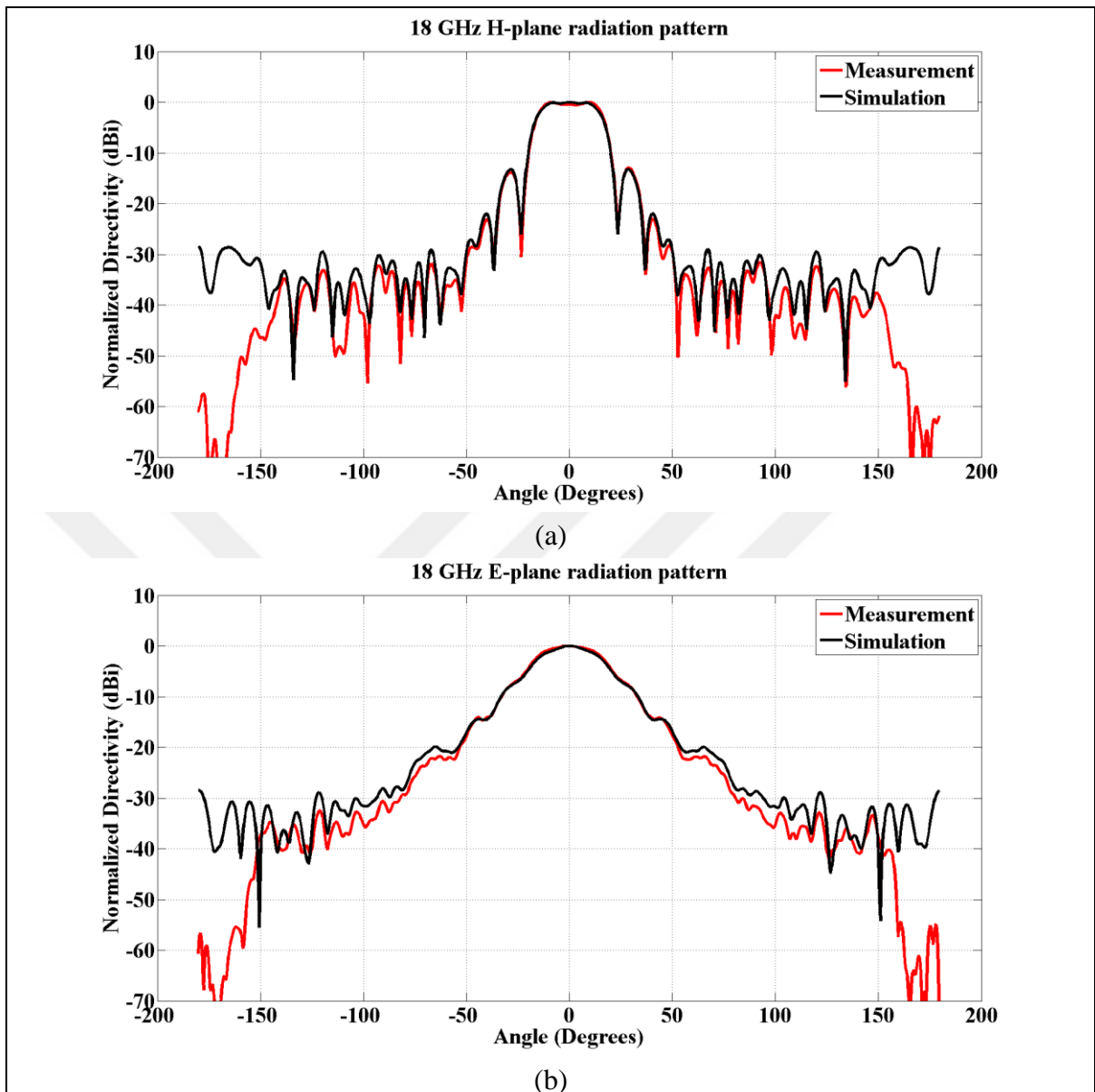Figure 5.6. The comparison of simulated and measured 11.25 GHz radiation patterns of coax-fed curved pinwall DRHA (a) H-plane (Azimuth) (b) E-plane (Elevation)

Figure 5.7. The comparison of simulated and measured 18 GHz radiation patterns of coax-fed curved pinwall DRHA (a) H-plane (Azimuth) (b) E-plane (Elevation)
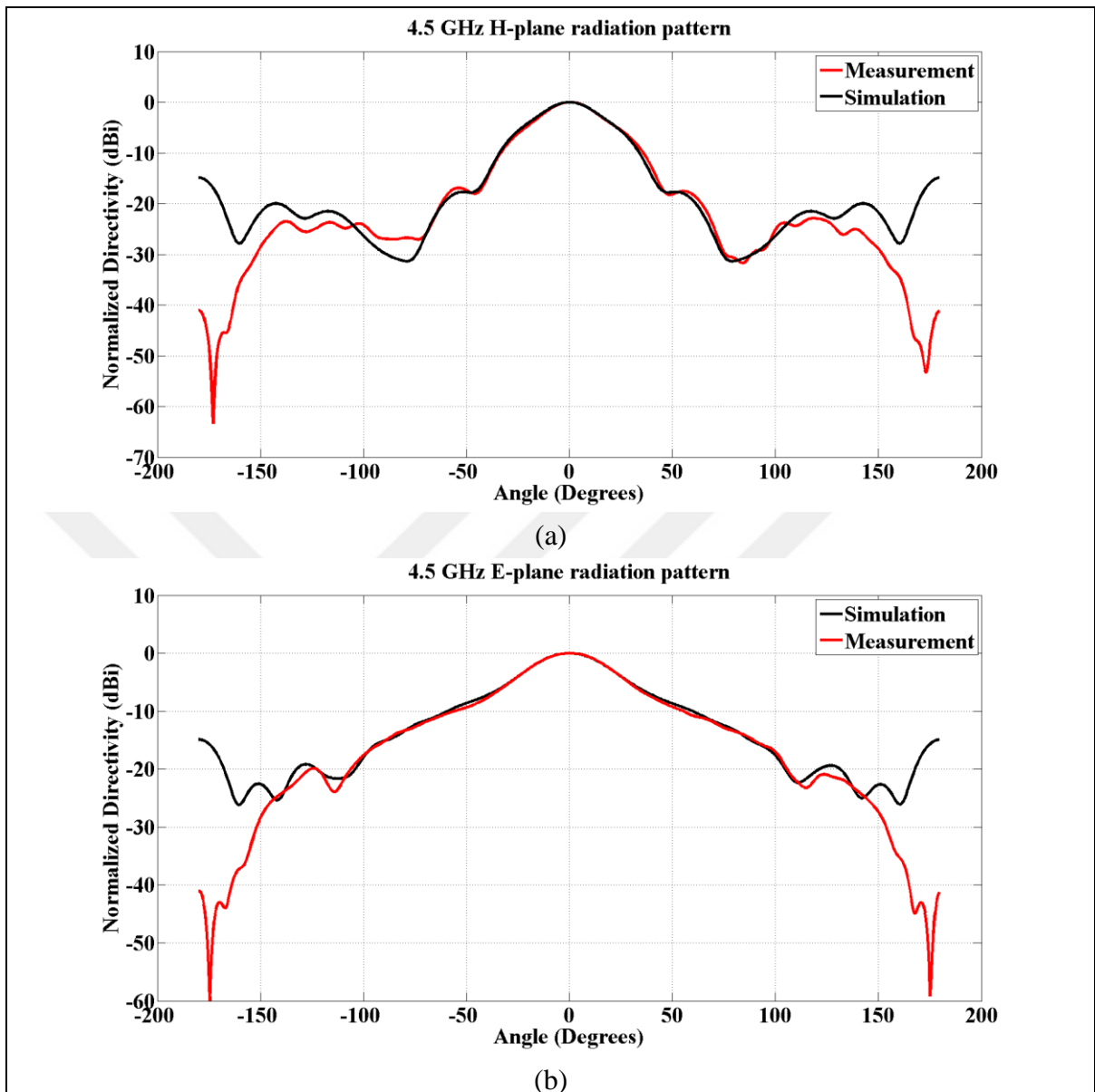
Figure 5.8. The comparison of simulated and measured 4.5 GHz radiation patterns of NCBWHA (a) H-plane (Azimuth) (b) E-plane (Elevation)
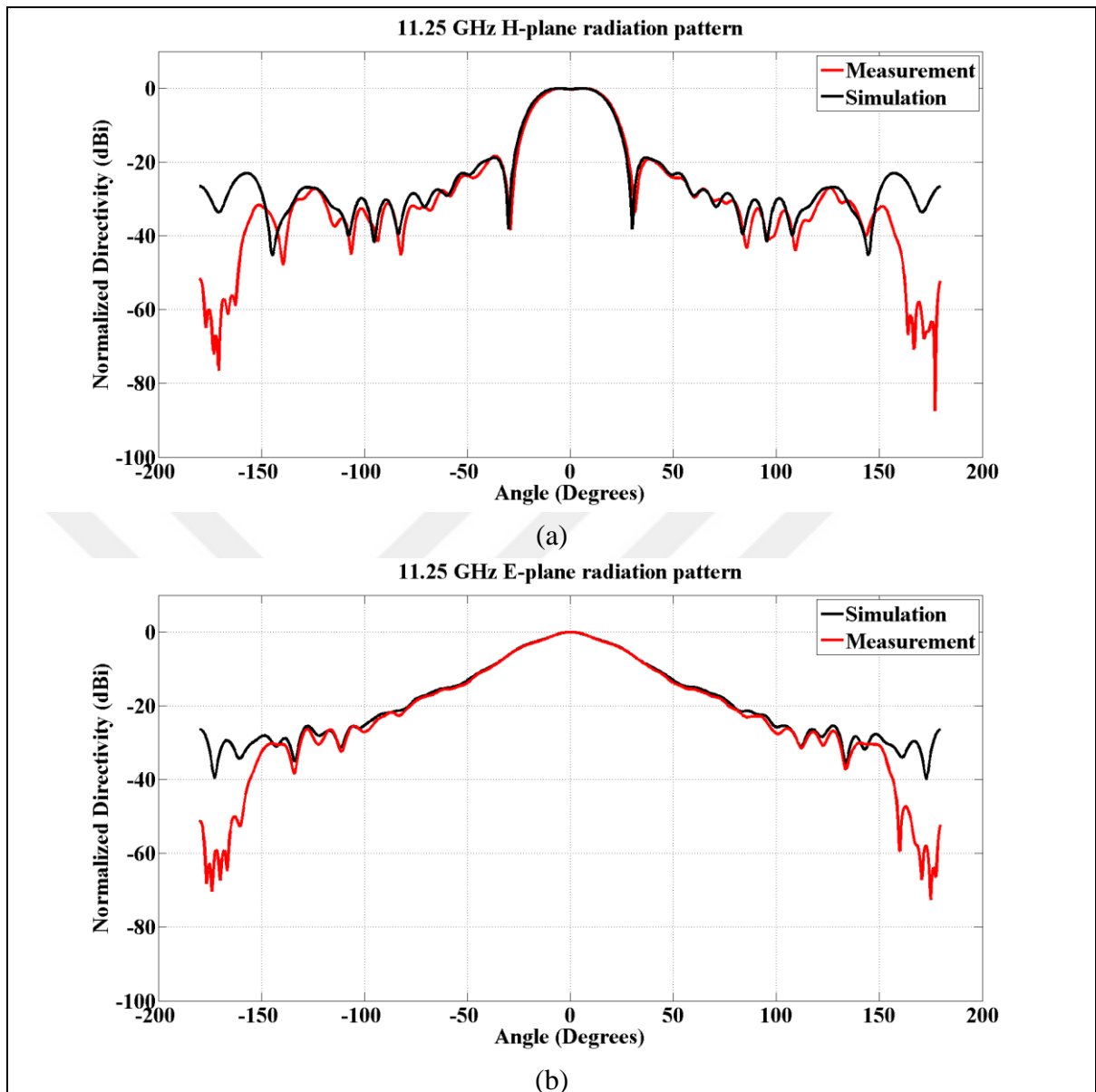
Figure 5.9. The comparison of simulated and measured 11.25 GHz radiation patterns of NCBWHA (a) H-plane (Azimuth) (b) E-plane (Elevation)
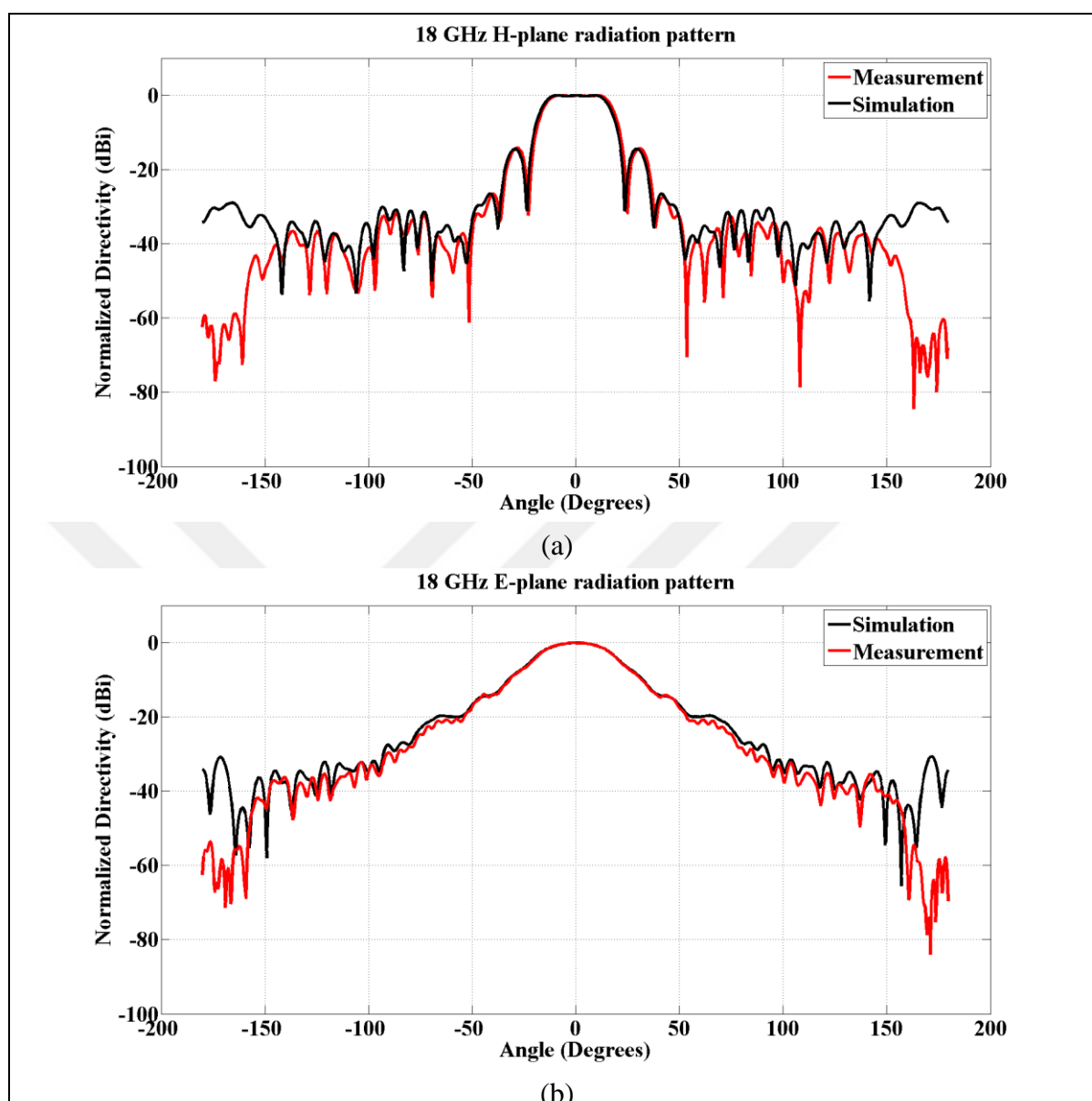
Figure 5.10. The comparison of simulated and measured 18 GHz radiation patterns of NCBWHA (a) H-plane (Azimuth) (b) E-plane (Elevation)

The comparison results of radiation patterns are presented from Figure 5.5 to Figure 5.10. It can be seen that the simulations are very successful. Although the results of the simulations and the measurements matches perfectly, a difference between the results are noticed after ±150 degrees. This is because azimuth axis rotator and mount of the antenna under test causes pattern blockage. Although the SNF measurement system can measure almost 360° coverage in azimuth and elevation, the system is not very suitable to determine the back-lobe pattern of the antenna. The back -lobe pattern is typically blocked

by the positioner/rotating system and limits the azimuth coverage to ±150° [79]. Thus, the measurement discrepancies given in Figure 5.5 to Figure 5.10 are observed after ±150 degrees, because it corresponded to the area surrounded by the absorber material in positioner and thus the antenna can not receive the signal. The mismatching between the simulated and measured back-lobe patterns results from the above-mentioned measurement system error.

The directivities and VSWR results of the manufactured antennas are given in Figure 5.11.
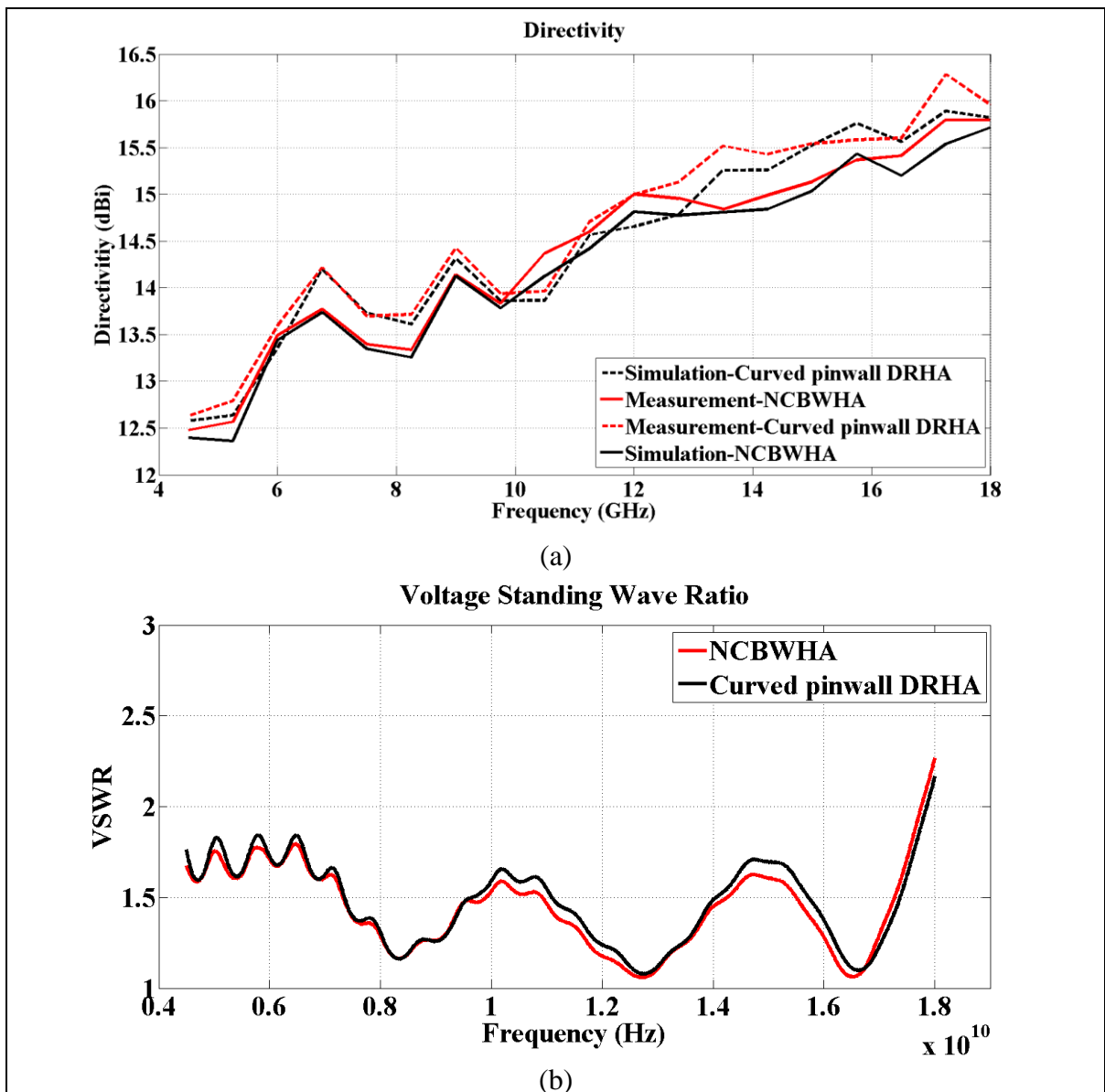

(a)

(b)

Figure 5.11. The comparison of simulated and measured (a) directivity and (b) VSWR

It can be noticed that, the simulated and measured directivity results of the antennas are very similar as in the radiation patterns. The measured VSWR results are also below the value of 2.5, providing the antenna design specification, while 40 per cent of the frequency band is less than 1.5, 59 per cent of the frequency band is less than 2 and only 1 per cent of the frequency band is between 2 and 2.3.

Co- and cross- polarized E- and H- plane radiation patterns of the curved pinwall antenna and NCBWHA are given at 10 different frequency points in the whole band (Figure 5.12 and Figure 5.13).
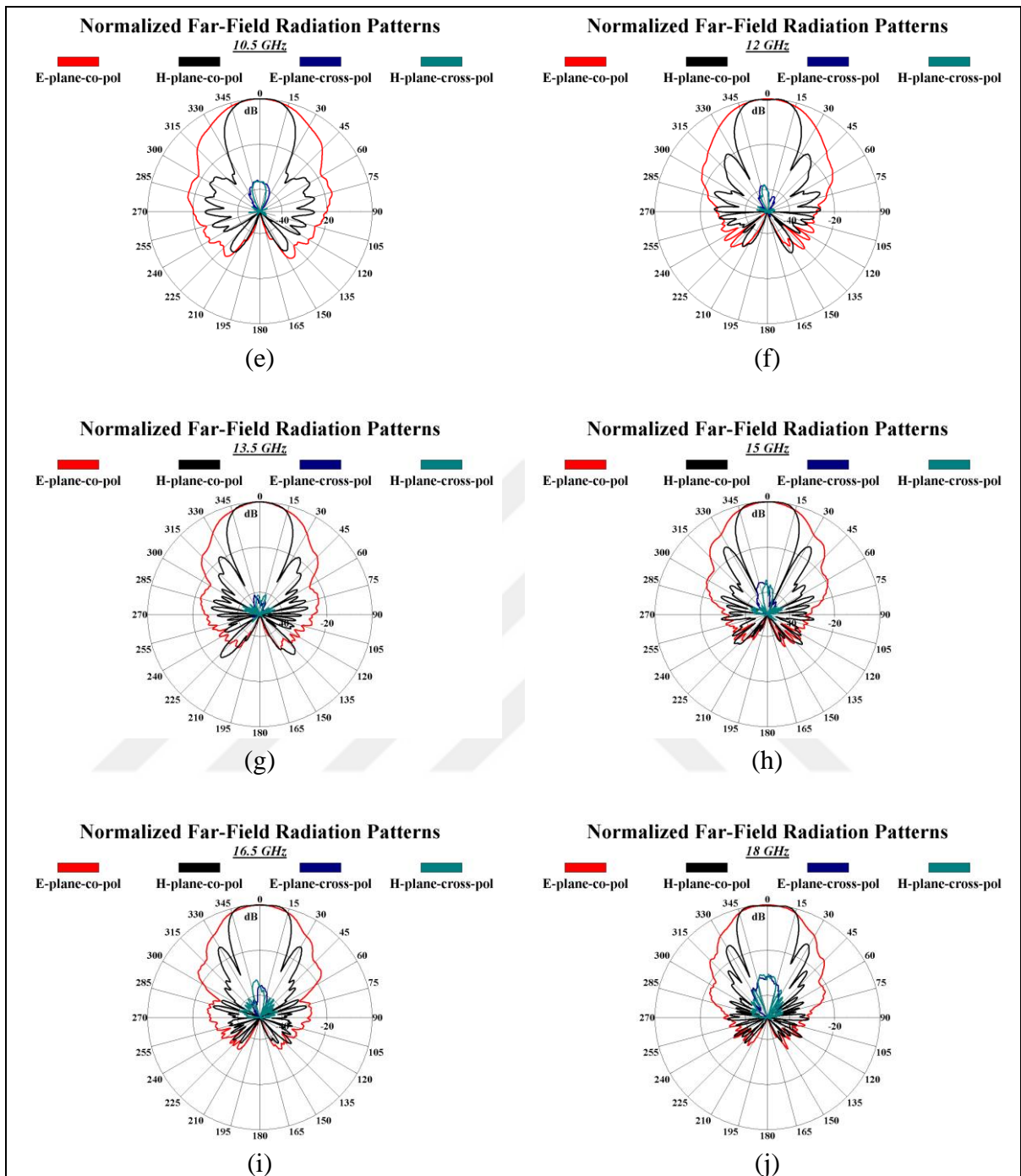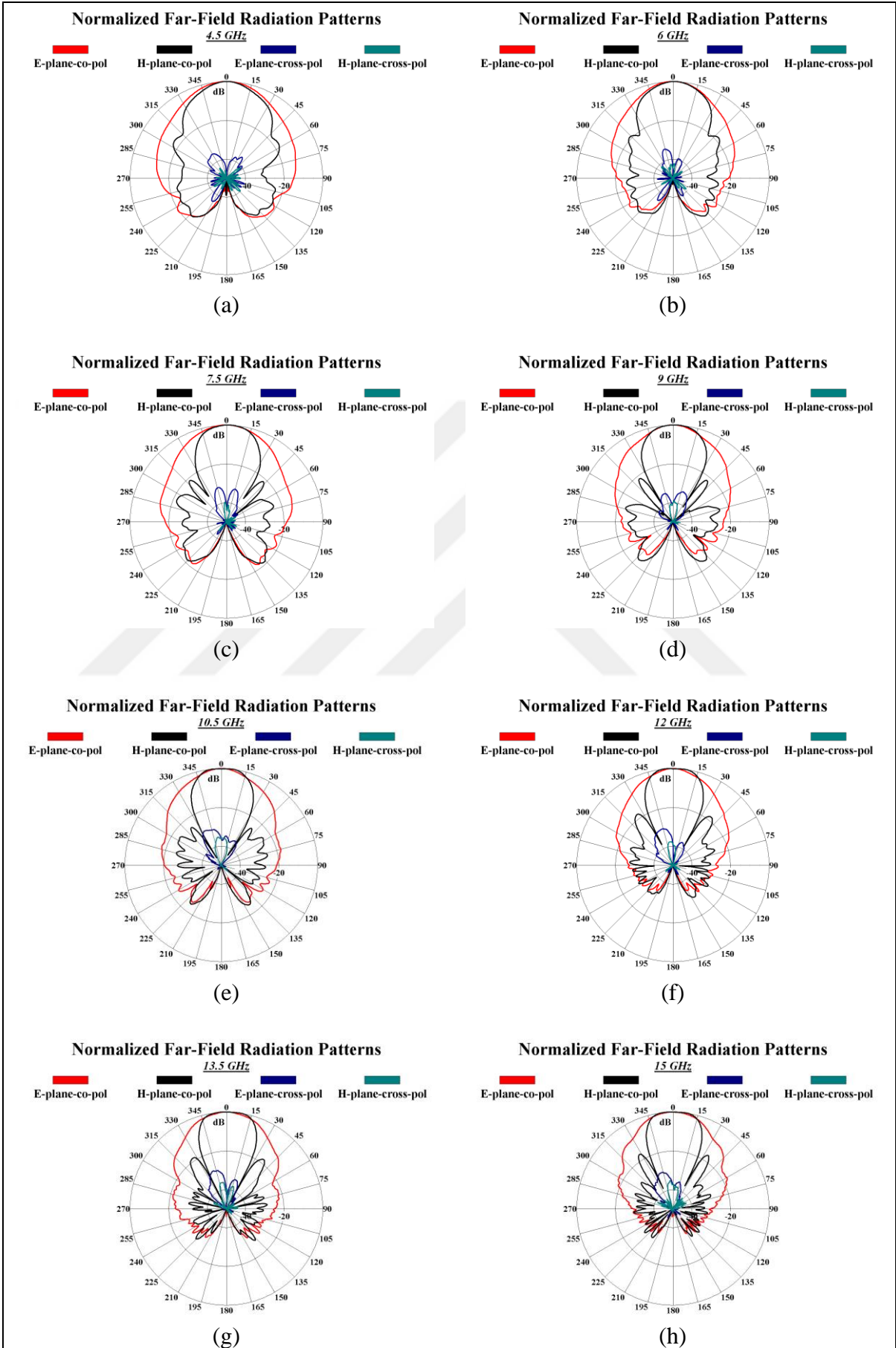

(a)

(b)

(c)

(d)
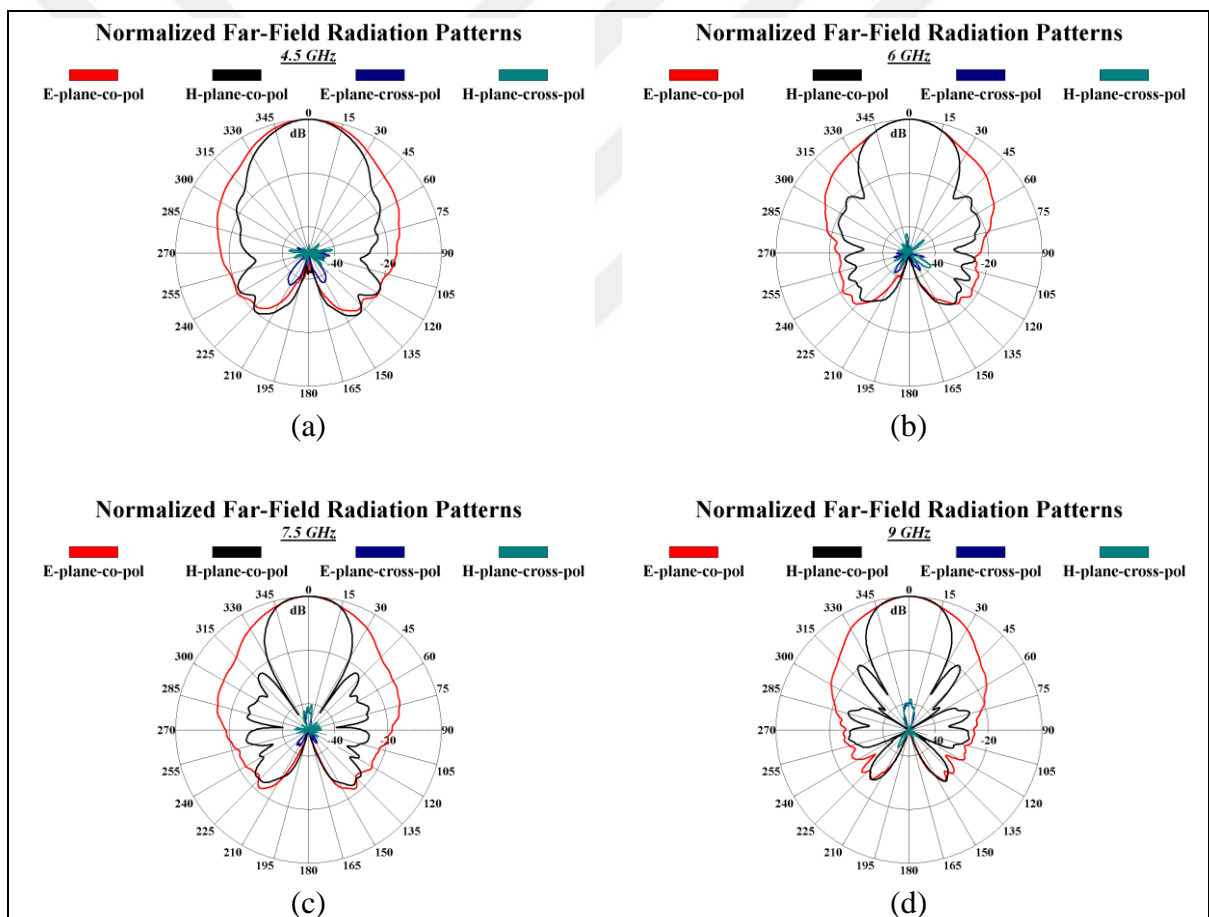
Figure 5.12. Co- and cross-polarized H- and E- plane measured radiation diagrams of coax-fed curved pinwall DRHA (a) 4.5 GHz, (b) 6 GHz, (c) 7.5 GHz, (d) 9 GHz, (e) 10.5 GHz, (f) 12 GHz, (g) 13.5 GHz, (h) 15 GHz, (i) 16.5 GHz, (j) 18 GHz
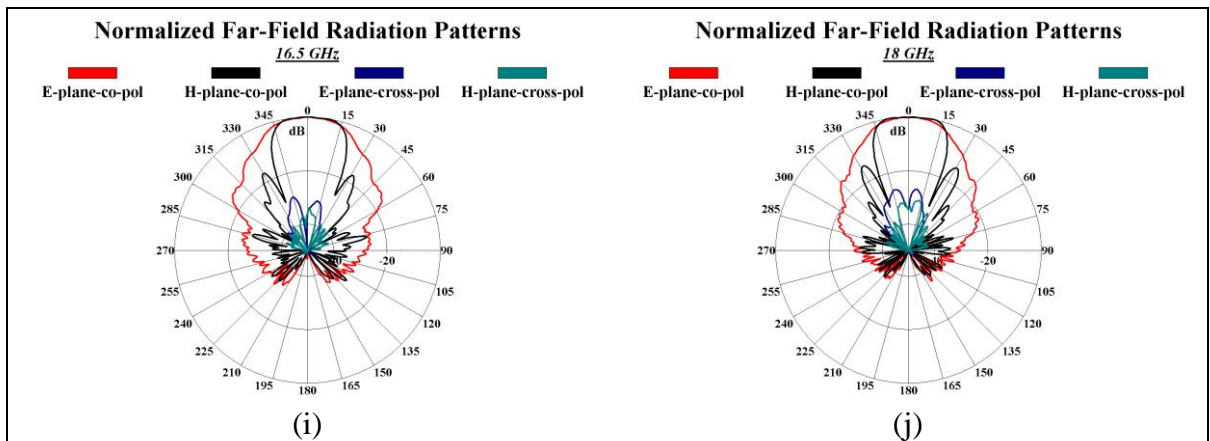
Normalized Far-Field Radiation Patterns
4.5 GHz

E-plane-co-pol   H-plane-co-pol   E-plane-cross-pol   H-plane-cross-pol

(a)

Normalized Far-Field Radiation Patterns
6 GHz

E-plane-co-pol   H-plane-co-pol   E-plane-cross-pol   H-plane-cross-pol

(b)

Normalized Far-Field Radiation Patterns
7.5 GHz

E-plane-co-pol   H-plane-co-pol   E-plane-cross-pol   H-plane-cross-pol

(c)

Normalized Far-Field Radiation Patterns
9 GHz

E-plane-co-pol   H-plane-co-pol   E-plane-cross-pol   H-plane-cross-pol

(d)

Normalized Far-Field Radiation Patterns
10.5 GHz

E-plane-co-pol   H-plane-co-pol   E-plane-cross-pol   H-plane-cross-pol

(e)

Normalized Far-Field Radiation Patterns
12 GHz

E-plane-co-pol   H-plane-co-pol   E-plane-cross-pol   H-plane-cross-pol

(f)

Normalized Far-Field Radiation Patterns
13.5 GHz

E-plane-co-pol   H-plane-co-pol   E-plane-cross-pol   H-plane-cross-pol

(g)

Normalized Far-Field Radiation Patterns
15 GHz

E-plane-co-pol   H-plane-co-pol   E-plane-cross-pol   H-plane-cross-pol

(h)

Figure 5.13. Co- and cross-polarized H- and E- plane measured radiation diagrams of NCBWHA (a) 4.5 GHz, (b) 6 GHz, (c) 7.5 GHz, (d) 9 GHz, (e) 10.5 GHz, (f) 12 GHz, (g) 13.5 GHz, (h) 15 GHz, (i) 16.5 GHz, (j) 18 GHz
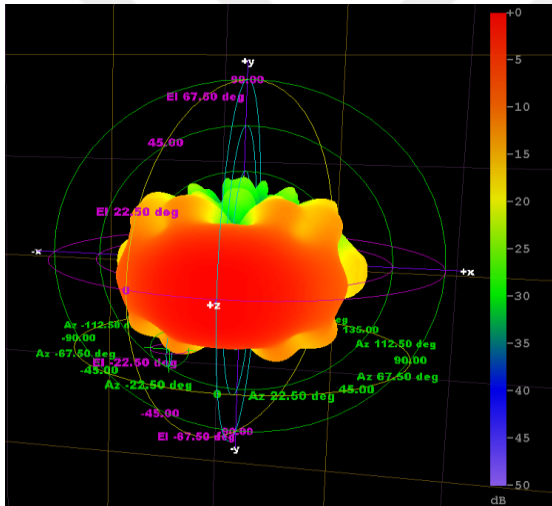
We have also looked at the 3D radiation patterns to see if there is any distortion of the pattern in any axis other than azimuth and elevation sections (Figure 5.14 and Figure 5.15).
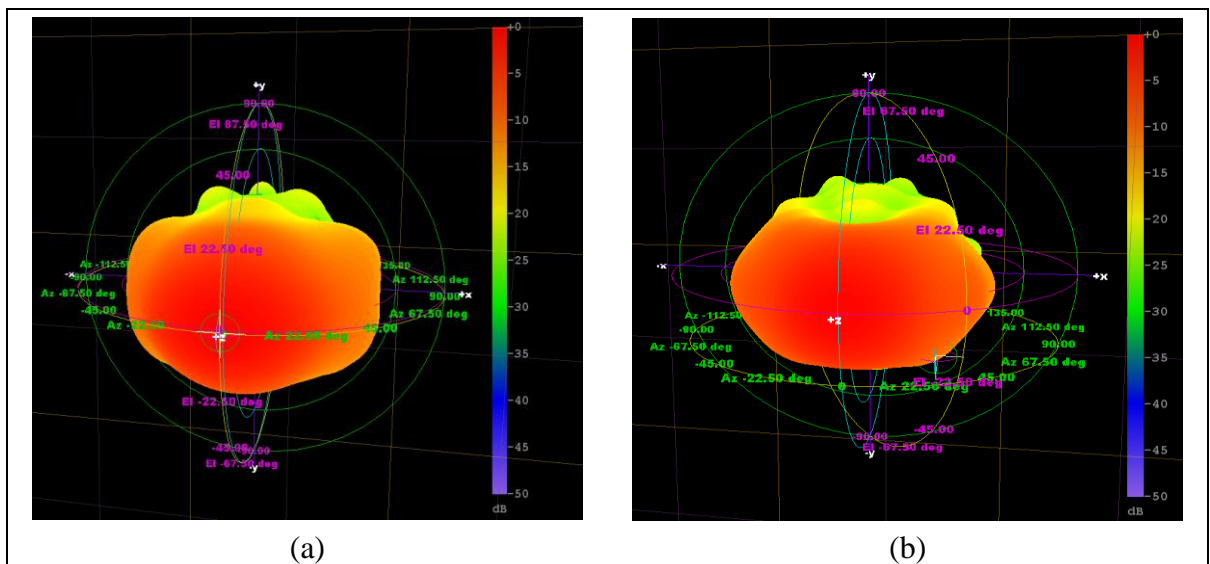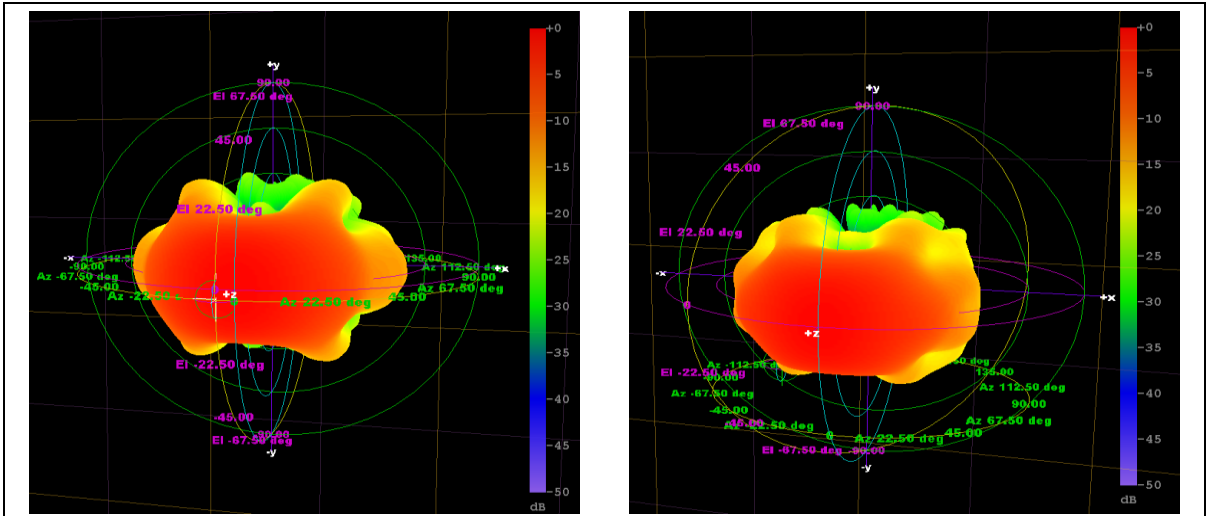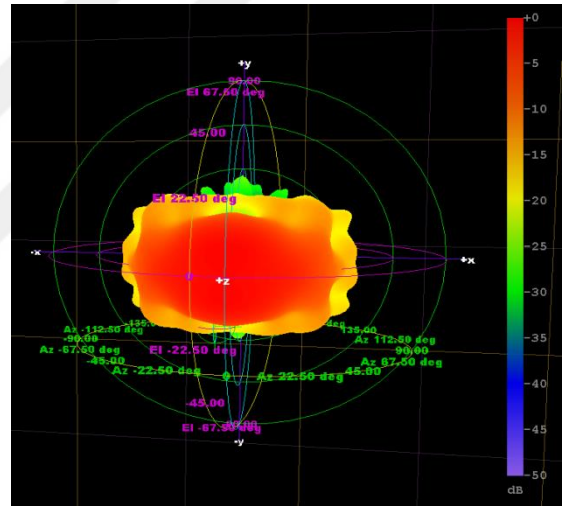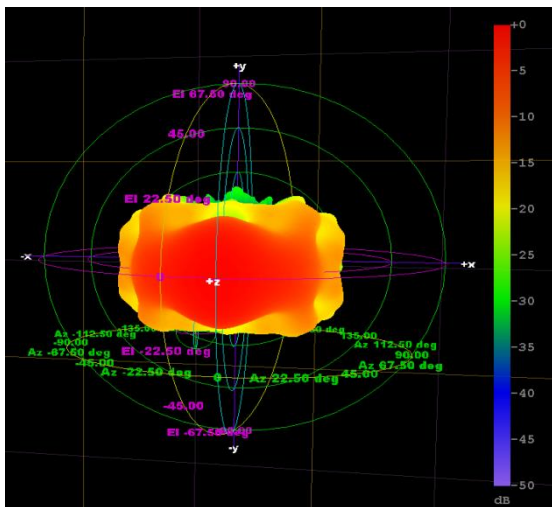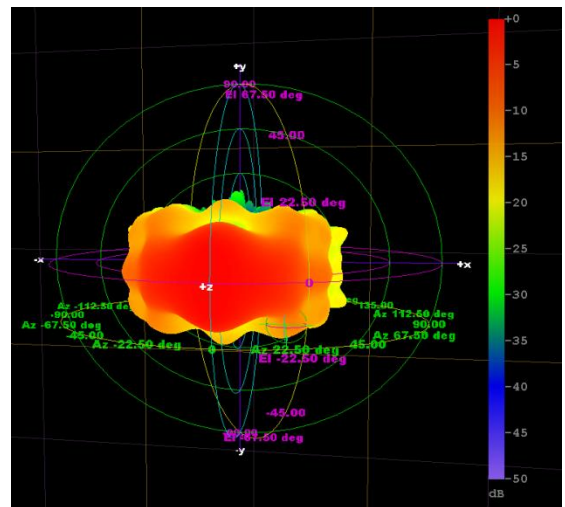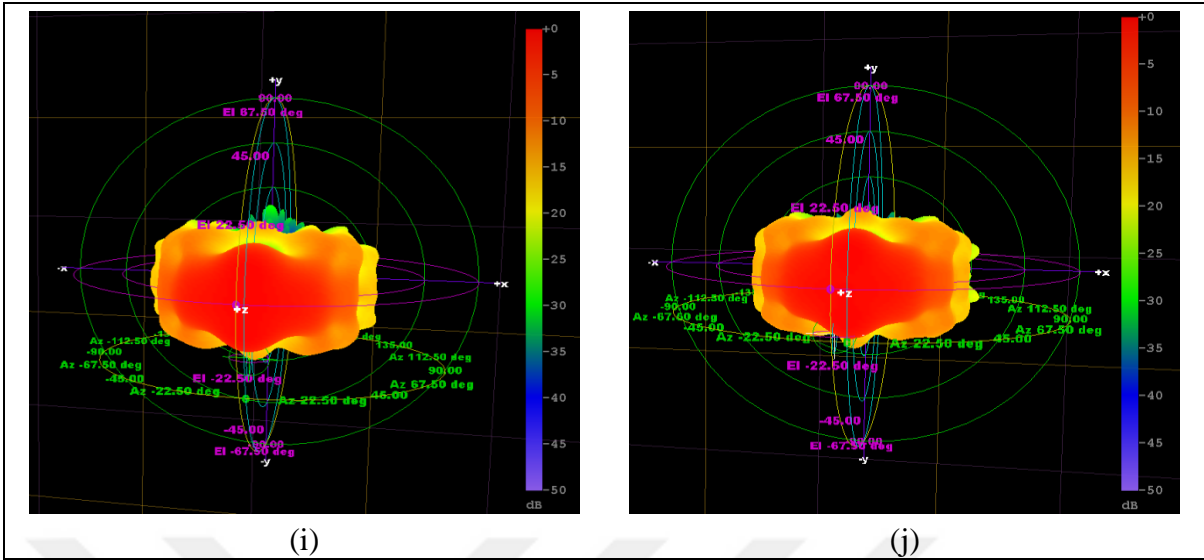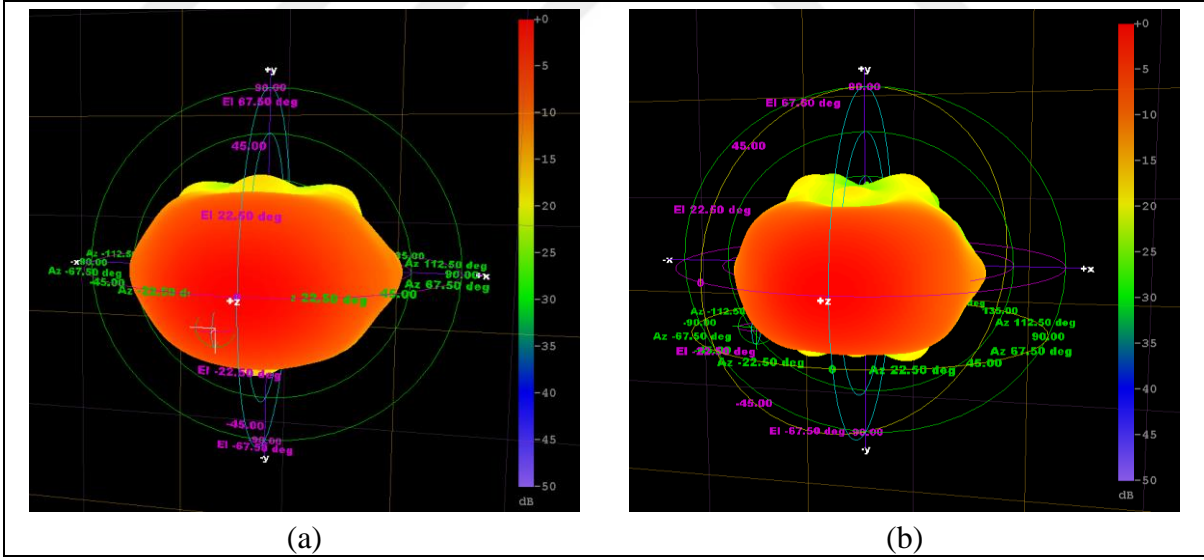
(c)

(d)

(e)

(f)

(g)

(h)

Figure 5.14. 3D radiation diagrams of coax-fed curved pinwall DRHA (a) 4.5 GHz, (b) 6 GHz, (c) 7.5 GHz, (d) 9 GHz, (e) 10.5 GHz, (f) 12 GHz, (g) 13.5 GHz, (h) 15 GHz, (i) 16.5 GHz, (j) 18 GHz

(c)

(d)

(e)

(f)

(g)

(h)

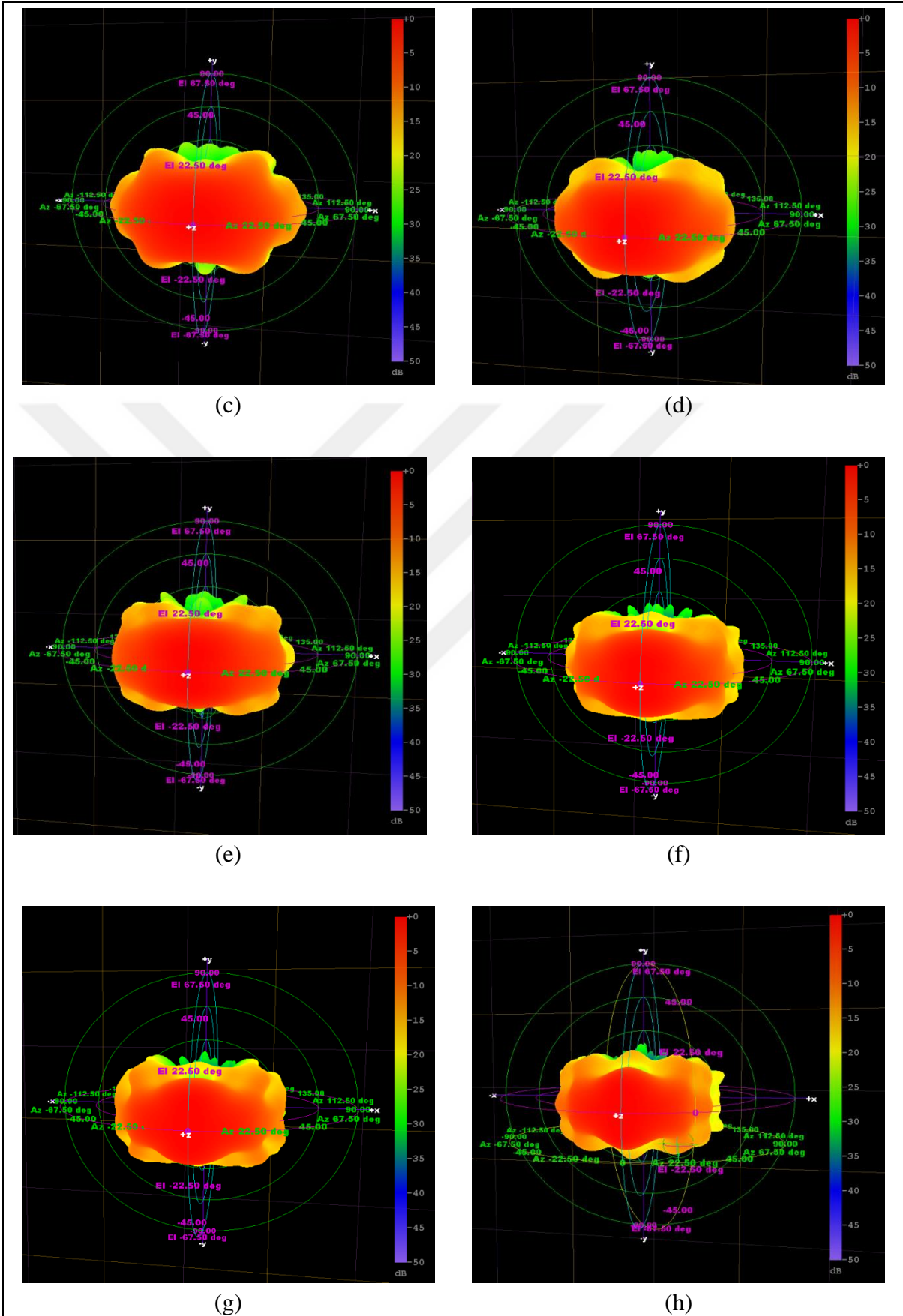(i)   (j)
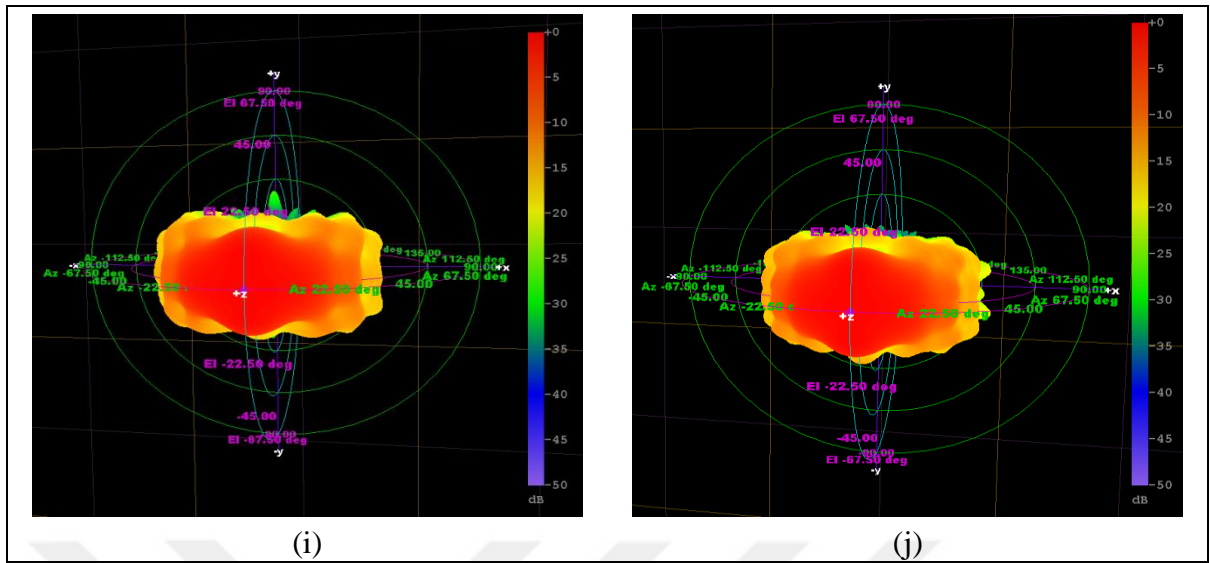
Figure 5.15. 3D radiation diagrams of NCBWHA (a) 4.5 GHz, (b) 6 GHz, (c) 7.5 GHz, (d)
9 GHz, (e) 10.5 GHz, (f) 12 GHz, (g) 13.5 GHz, (h) 15 GHz, (i) 16.5 GHz, (j) 18 GHz

HPBW-frequency variation of the antennas are presented in Figure 5.16 and Figure 5.17.

(a)
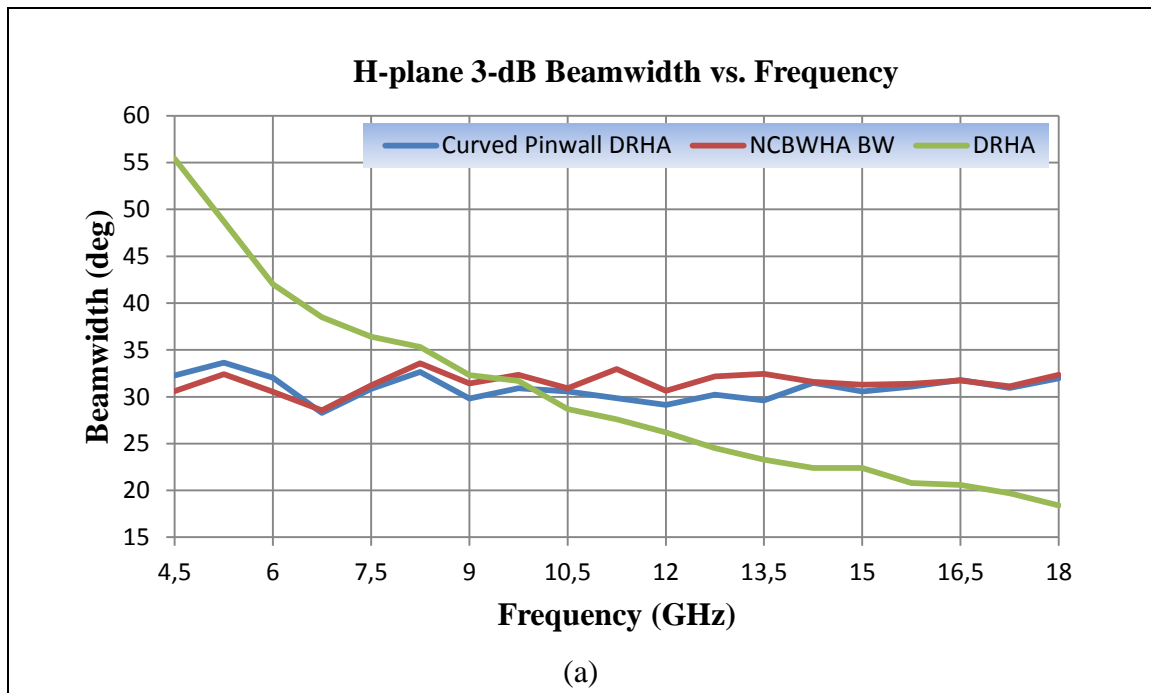
Figure 5.16. The comparison of HPBW-frequency variation of DRHA, curved pinwall
DRHA and NCBWHA (a) H-plane (b) E-plane

Figure 5.17. The variation of H- and E- plane normalized 3-dB beamwidths of NCBWHA
and DRHA along the frequency band: 4.5 – 18 GHz

Figure 5.16 shows that although the beamwidth variation and pattern smoothness in both azimuth and elevation are close to each other, NCBWHA is slightly better, especially in E-plane. The E- and H-plane 3-dB beamwidth is also drawn as normalized to average value of HPBWs to see the variation along the operating frequency band a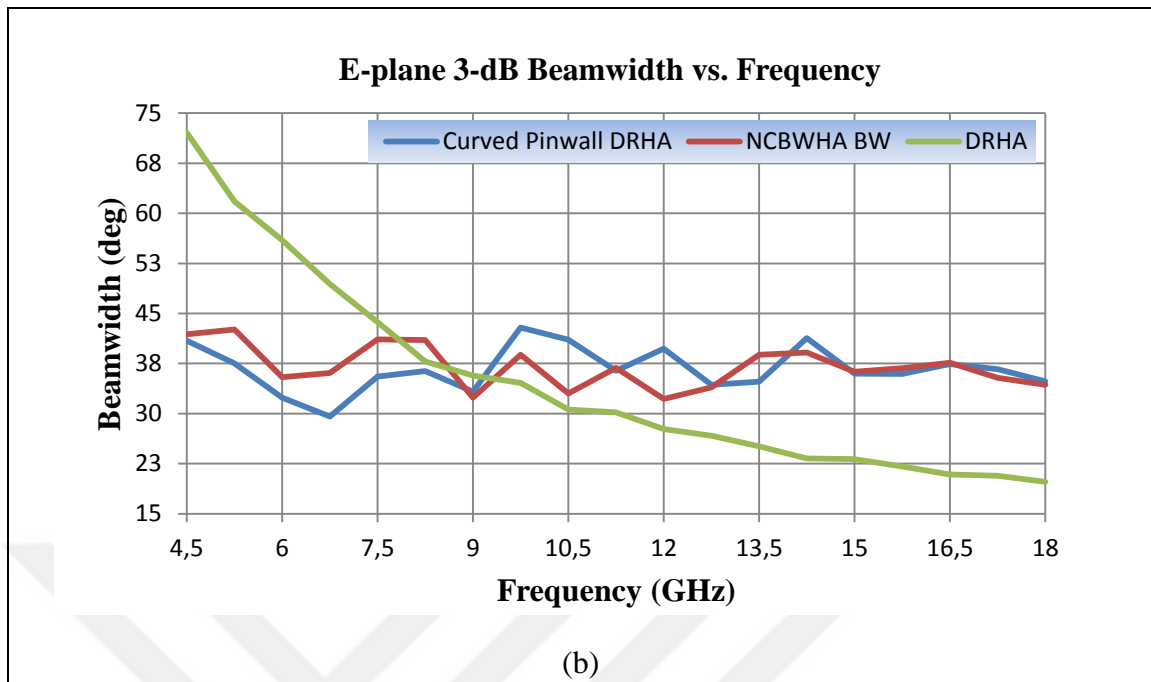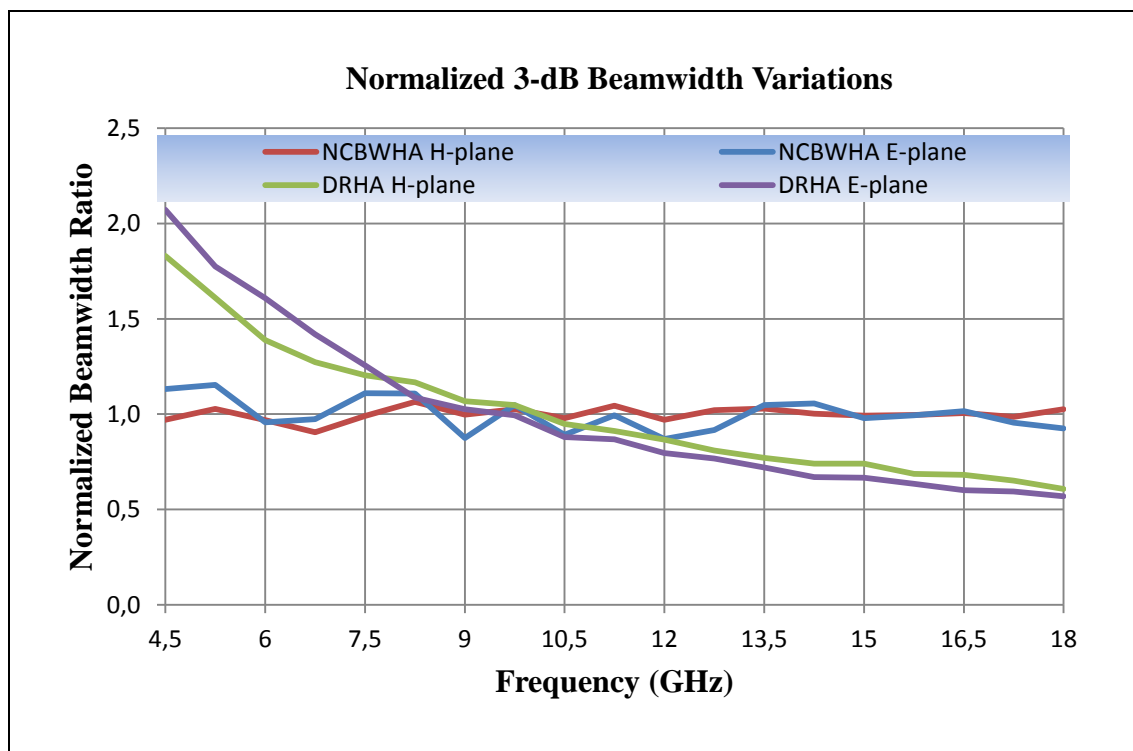nd to emphasize the difference between NCBWHA and conventional DRHA (Figure 5.17). It is evident from Figures 5.16 and 5.17 that the intended constant beamwidth is provided along the desired wideband.

Finally, the measured gains of the manufactured curved pinwall DRHA and NCBWHA are compared with conventional DRHA in Figure 5.18. The gains of the antennas are measured by comparison method in an anechoic chamber. First, previously determined and verified SGHA pattern measurements are performed in the same system to determine the field values. Then, the radiation pattern measurements of our manufactured antennas are performed and the gains of antennas are calculated from the comparison of field values of SGHA and manufactured antennas. The results are shown in Figure 5.18.
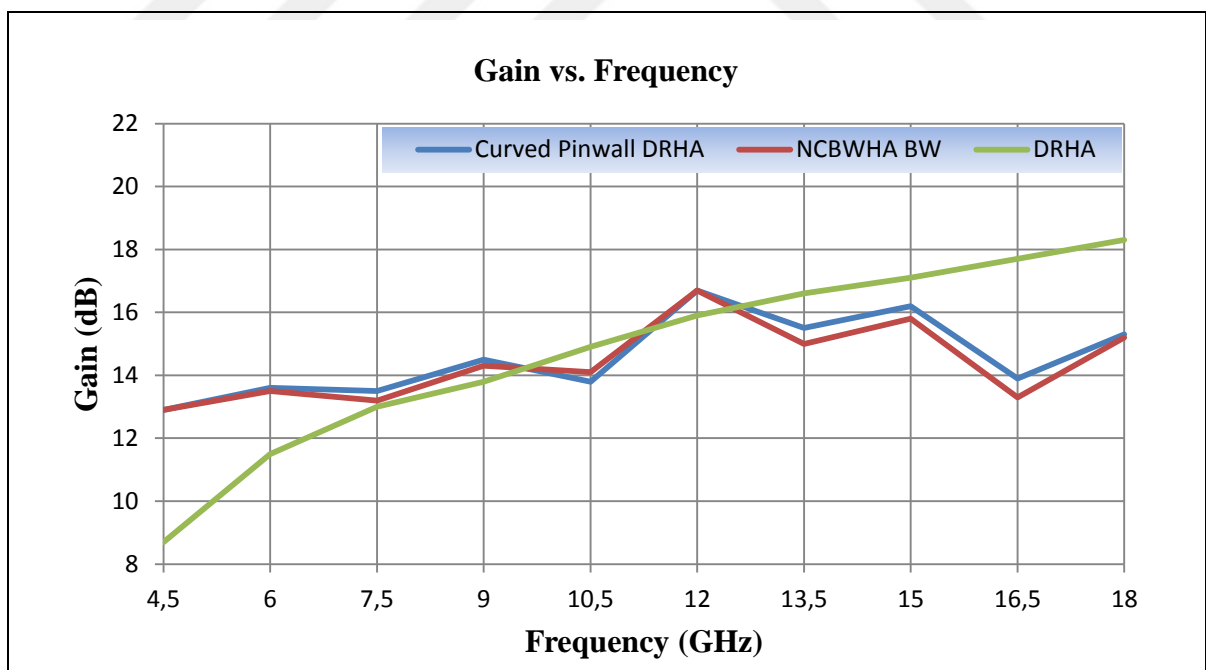

Figure 5.18. The comparison of gain variation along the frequency band: Curved pinwall DRHA, NCBWHA and DRHA

The change in critical antenna parameters and the improvement in beamwidth constancy from the first designed broadband antenna to the recently designed NCBWHA are presented in Table 5.2.

Table 5.2. The comparison of the parameters of DRHA, curved pinwall DRHA and NCBWHA

	DRHA	Curved pinwall DRHA	NCBWHA
Gain (dBi)	8.7-18.4	12.9-16.7	12.9-16.7
HPBW (Azimuth) (Degree)	18.4-55.4	28.2-33.6	28.5-33.5
HPBW (Elevation) (Degree)	19.8-72.1	29.5-42.9	32.2-42.6

Furthermore, the comparison of beamwidth variation of different antennas is given in Table 5.3.

Table 5.3. The H-plane beamwidth variations of six different wideband near-constant beamwidth antennas and X-band SGHA

	Designed NCBWHA	[3]*	[80]	[72]	[58]	DRHA	X band SGHA
Bandwidth Ratio	4:1	4:1	2.25:1	2.25:1	2.4:1	4:1	1.5:1
Beamwidth Variation (%)	± 8	± 13	± 14	± 13	± 12	± 50	± 17
*Major lobe was split and multilobe characteristics appeared.							

As a result of the design, the radiation pattern quality of NCBWHA, which includes pattern shape, beamwidth constancy, and side-lobe levels are far better than other designs providing a wide frequency band given in Table 5.3. In fact, there ss no previously

designed antenna with a frequency band of ratio 4:1 with beamwidth constancy feature. However, designed curved pinwall, stepped-shape corrugated, shaped-flare DRHA is even better than the narrower bandwidth antennas given in the literature. The measured H- and E- plane beamwidths have an average value of 31.0^o and 37.4^o with an associated standard deviation of 2.5^o and 5.2^o over the whole frequency band respectively. Table 5.2 shows that the frequency along the operating band of the antenna increases by 4 times (4.5 to 18 GHz), while half power beamwidths on the H- and E-plane vary by 1.17 and 1.32 times, respectively. Note that these ratios were 3.01 and 3.65 for the previously designed conventional DRHA (given in Chapter 3.2), 1.36 and 1.43 for the modified DRHA (given in Chapter 4.1), 1.19 and 1.45 for curved pinwall DRHA (given in Chapter 4.1).

6. CONCLUSIONS

In this study, we have designed a new 4.5 – 18 GHz near-constant beamwidth curved pinwall corrugated DRHA. Comprehensive design methodology is also presented.

Initially, we have examined waveguide and ridged waveguide structures, then we have designed an X-band SGHA and conventional DRHA to observe the characteristics of the horns and used them as references for beamwidth variation of the horns through the operating band. Later, we have investigated the requirements to achieve the constant beamwidth feature in detail.

It is possible to divide the proposed design process into four stages, i) conventional X-band SGHA and DRHA design including desired frequency band, 4.5 – 18 GHz, ii) modification of the conventional DRHA: adjustment of the flare including the aperture width, height, throat length and redesign of ridge profile, iii) the replacement of horn sidewalls by properly positioned pins: the pins can be designed as curved instead of straight line, and iv) E-plane walls are corrugated with a new wideband slot called "stepped-shape" and addition of section called "shaped-flare".

It is important to note that the derived expressions and the proposed design method present a simple and accurate way to design a constant beamwidth wideband horn antenna.

The most important points of the design are finding the location of the pins, and determining wideband slot design. First, we adjust the width of the aperture where the pins are located to achieve the desired beamwidth. Then, we arrange the distance between the two pins to be half-wavelength of the corresponding frequency. We choose the frequency points according to number of the pins, and 8 pins number is determined by looking at the results of the calculations and the simulations. We choose the arrangement as a logarithmic instead of linear, so that the distances are equal in per cent, and the pins are placed at these points accordingly. Additionally, we include the curved pinwalls instead of straight pins to make a further improvement in H-plane constant beamwidth. Further improvements to the E-plane beamwidths as well as H-plane necessitate a better understanding of the E-plane boundary conditions and need structural change. Thus, we introduce a new corrugation slot in E-plane walls called "stepped-shape". We derive the input admittance expression of a

new slot and compare it with the conventional ones. It is seen that, this new slot design provides approximately 2 times more bandwidth. Meanwhile, we design double ridged waveguide-to-coaxial adapter for impedance matching around 50 Ω.

We perform the electromagnetic simulations of the designed antenna using CST Microwave Studio. Two of designed antennas are manufactured and the antenna parameters such as radiation pattern, VSWR, gain and HPBW variations along the desired band are measured. The radiation pattern measurements are performed in an anechoic chamber at TUBITAK, ATAM using the spherical near-field measurement system. We observed that the measurement results of 2D H-plane and E-plane radiation patterns are in a good agreement with the ones obtained in simulations. Furthermore, directivities of simulated and measured antennas are also similar.

We have obtained a horn antenna which presents a ratio of 4:1 wideband characteristics with $31.0^{o} \pm 2.5^{o}$ H-plane 3-dB beamwidth (± 8.0 per cent variation about mean HPBW). Similar parameter values for E-plane 3-dB beamwidth are $37.4^{o} \pm 5.2^{o}$, which corresponds to ± 13.9 per cent variation.

It is possible to use the methodology outlined in the study to design a DRHA to be used as an antenna array element in broadband DF systems which require relatively high boresight gain and 3-dB beamwidth constancy.

7. FUTURE WORK

The designed NCBWHA is a single linear polarized horn antenna. It is possible to investigate the dual or circular polarized constant beamwidth horn antenna design for some DF systems and reflector antenna applications. There is a need to investigate how the proposed structures in this study can be used in quad ridged horn antennas (QRHA) and how they can be adapted to these antennas.

Furthermore, a horn antenna design similar to the one in this study can be proposed, but with a wider beamwidth as a reflector antenna feed. As we mentioned at the beginning of the dissertation, one of the two important application areas of the constant beamwidth horn antenna is the reflector antenna feed. In this study, we aimed to design 3-dB beamwidth around 30 degrees. Although 10-dB beamwidth parameter is important for reflector designs, designed NCBWHA can be considered as having a narrow beam for using it as a reflector feed. Therefore, a new constant beamwidth horn antenna with a wider beamwidth can be designed.

REFERENCES

1. Dewey RJ, Hill R. Wideband constant beamwidth horn antenna. *1981 11th European Microwave Conference*; 1981: IEEE.

2. Ferris JE, Zimmerman WE. A broadband constant beamwidth high-gain antenna. *1966 International Symposium on Antennas and Propagation Society;* 1966: IEEE.

3. Parker CF, Anderson RJ. Constant beamwidth broadband antennas. *1958 IRE International Convention Record*; 1966: IEEE.

4. Nakano H, Nogami K, Araj S, Mimaki H, Yamauchi J. A spiral antenna backed by a conducting plane reflector. *IEEE Transactions on Antennas and Propagation*. 1986;34(6):791-796.

5. Klimya TS, Parakash AK. Cavity backing in spiral antennas. *International Journal of Engineering Research and General Science*. 2015;3(1):955-959.

6. Dybdal R. Defocusing loss for a log periodic-fed reflector. *IEEE Transactions on Antennas and Propagation*. 1985;33(7):809–812.

7. IEEE standard for definitions of terms for antennas. *IEEE Antennas and Propagation Society*; IEEE Std 145™-2013.

8. Kretzschmar JG. Wave propagation in hollow conducting elliptical waveguides *IEEE Transactions on Microwave Theory and Techniques*. 1970;18(9):547-554.

9. Orfanidis SJ. *Electromagnetic waves and antennas.* New Jersey: Rutgers University; 2016.

10. Hayt WH, Buck JA. *Engineering electromagnetics*. New York: McGraw Hill Comp; 2001.

11. Pozar DM. *Microwave engineering*. New Jersey: John Wiley & Sons Inc; 2012.

12. Hopfer S. The design of ridged waveguides. *IRE Transactions on Microwave Theory and Technique*. 1955;3(5):20-29.

13.　Milligan TA. *Modern antenna design*. New Jersey: IEEE Press, John Wiley & Sons Inc; 2005.

14.　Marcuvitz N. *Waveguide handbook.* MIT Radiation Lab. Series, no. 10, Boston: Technical Publishers Inc; 1964.

15.　Helszajn J. *Ridge waveguides and passive microwave components.* London: The Institution of Engineering and Technology; 2000.

16.　Cohn SB. Properties of ridge waveguide. *Proceedings of the IRE.* 1947;35(8):783-788.

17.　Whinnery JR, Jamieson HW. Equivalent circuits for discontinuities in transmission lines. *Proceedings of the IRE.* 1944;32(2):98-114.

18.　Chen TS. Calculation of the parameters of ridge waveguide. *IRE Transactions on Microwave Theory and Techniques.* 1957;5(1):12–17.

19.　Getsinger WJ. Ridge waveguide field description and application to directional couplers. *IRE Transactions on Microwave Theory and Techniques.* 1962;10(1):41-50.

20.　Pyle JR. The cutoff wavelength of the TE10 mode in ridged rectangular waveguide of any aspect ratio. *IEEE Transactions on Microwave Theory and Techniques.* 1966;14(4);175–183.

21.　Montgomery JP. On the complete eigenvalue solution of ridged waveguide. *IEEE Transactions on Microwave Theory and Technology.* 1971;19(6):547-555.

22.　Balanis CA. *Antenna theory analysis and design.* New Jersey: John Wiley & Sons Inc; 2005.

23.　Volakis JL. *Antenna engineering handbook.* New York: McGraw-Hill Companies; 2007.

24.　Stutzman WL, Thiele GA. *Antenna theory and design.* New Jersey: John Wiley & Sons Inc; 2013.

25.   Pereira LPS, Terada MAB. New method for optimum design of pyramidal horn antennas. *Journal of Microwaves, Optoelectronics and Electromagnetic Applications*. 2011;10(1):266-277.

26.   Liu K, Balanis CA, Birtcher CR, Barber GC. Analysis of pyramidal horn antennas using moment methods. *IEEE Transactions on Antennas and Propagation*. 1993;41(10):1379-1389.

27.   Aurand JF. A new design procedure for optimum gain pyramidal horns. *Antennas and Propagation, 1988 IEEE International Symposium;* 1988: IEEE.

28.   Selvan KT. Accurate design method for pyramidal horns of any desired gain and aperture phase error. *IEEE Antennas and Wireless Propagation Letters*. 2008;7:31-32.

29.   Cozzens DE. Tables ease horn design. *Microwaves*. 1966;1:37-39.

30.   Schelkunoff SA. *Electromagnetic waves.* New York: Van Nostrand Rheinhold; 1943.

31.   Aurand J. Pyramidal horns, part 2: A novel design method for horns of any desired gain and aperture phase error. *Antennas and Propagation Society, 1989 International Symposium on*; 1989: IEEE.

32.   Guney K. A new design method for optimum gain pyramidal horns. *Electromagnetics.* 2001;21(6):497-505.

33.   Guney K, Hancer H. Improved formulas for narrow and wide aperture dimensions of optimum gain pyramidal horn. *International Journal RF Microwave Computer-aided Engineering*. 2003;13(3):239–245.

34.   Stutzman WL. Estimating directivity and gain of antennas. *IEEE Antennas and Propagation Magazine*. 1998;40(4):7–11.

35.   Kerr JL. Short axial length broad-band horns. *IEEE Transactions on Antennas and Propagation*. 1973;21(5):710-714.

36. Azimi MA, Arazm F, Dana RF. Design and optimization of a high-frequency EMC wideband horn antenna. *IET Microwave Antennas and Propagation*. 2007;1(3):580-585.

37. Xu H, Zhou Y, Li E, Liu H, Wang Q, Zhoung Z. Design and simulation of ultra-wideband double ridged horn antenna. *2010 International Conference on Microwave and Millimeter Wave Technology*; 2010: IEEE.

38. Jacobs OB, Odendaal JW, Joubert J. Elliptically shaped quad-ridge horn antennas as feed for a reflector. *IEEE Antennas and Wireless Propagation Letters*. 2011;10:756-759.

39. Jakobs OB, Odendaal JW, Joubert J. An improved design for a 1-18 GHz double-ridged guide horn antenna. *IEEE Transactions on Antennas and Propagation*. 2012;60(9):4110-4118.

40. Wang C, Li E, Zhang Y. Ridged horn antenna with adjustable metallic grid sidewalls and cross-shaped back cavity. *IEEE Antennas and Wireless Propagation Letters*. 2016;15:1221-1225.

41. Qiu J, Suo Y, Li W. Design and simulation of ultra-wideband quad-ridged horn antenna. *2007 International conference on Microwave and Millimeter Wave* Technology; 2007: IEEE.

42. Tenigeer, Zhang N, Qiu J, Zhang P, Zhang Y. Design of a novel broadband EMC double ridged guide horn antenna. *Progress in Electromagnetics Research C*. 2013;39:225-236.

43. Venkatesan V, Selvan KT. Rigorous gain measurements on wide-band ridge horn. *IEEE Transactions on Electromagnetic Compatibility*. 2006;48(3):592-594.

44. Cohn SB. Design of simple broad-band wave-guide-to-coaxial-line junctions. *Proceedings of the IRE*. 1947;920-926.

45. Isenlik T, Basaran E, Turetken B A novel 2-18 GHz double ridged horn antenna with an improved feed section design. *Electromagnetics*. 2015;35(3):145-154.

46. Akgiray A, Weinreb S. Ultrawideband square and circular quad-ridge horns with near-constant beamwidth. *2012 IEEE International Conference on Ultra-Wideband*; 2012: IEEE.

47. Akgiray A, Weinreb S, Imbriale W, Beaudoin C. Circular quadruple-ridged flared horn achieving near-constant beamwidth over multioctave bandwidth: design and measurements. *IEEE Transactions on Antennas and Propagation*. 2013;61(3):1099–1108.

48. Akgiray A, Weinreb S, Imbriale W. Design and measurements of dual-polarized wideband constant-beamwidth quadruple-ridged flared horn. *2011 IEEE International Symposium on Antennas and Propagation*; 2011: IEEE.

49. Massey PJ. Improvements in constant beamwidth horns. *1988 18th European Microwave Conference*; 1988: IEEE.

50. Beukman TS, Ivashina MV, Maaskant R, Meyer P, Bencivenni C. A quadraxial feed for ultra-wide bandwidth quadruple-ridged flared horn antennas. *2014 8th European Conference on Antennas and Propagation*; 2014: IEEE.

51. Morgan MA, Boyd TA. A 10-100-GHz double-ridged horn antenna and coax launcher. *IEEE Transactions on Antennas and Propagation*. 2015;63(8):3417-3422.

52. Jacobs OB. Quad-ridge horn antenna with elliptically shaped sidewalls for use as a reflector feed for radio astronomy. MSc Thesis, University of Pretoria, 2011.

53. Lai H, Franks R, Kong D, Kuck D, Gackstetter T. A broad band high efficient quad ridged horn. *1987 IEEE Antennas and Propagation Society International Symposium*; 1987: IEEE.

54. Qiu JH, Suo Y, Li W. Research and design on ultrawideband dielectric hemispheric lens loaded quad-ridged horn antenna. *2007 6th International Conference on Antenna Theory and Techniques;* 2007: IEEE.

55. Bauerle RJ, Schrimpf R, Gyorko E, Henderson J. The use of a dielectric lens to improve the efficiency of a dual polarized quad-ridge horn from 5 to 15 GHz. *IEEE Transactions on Antennas and Propagation*. 2009;57(6):1822–1825.

56. Serdar T, Kenan KA. Partially dielectric-loaded ridged horn antenna design for ultrawideband gain and radiation performance enhancement. *IEEE Antennas and Wireless Propagation Letters*. 2012;11:921-924.

57. Schneider WA, Blakney TL, Zanella VJ. Low sidelobe precise beam aspect ratio scalar horns. *IEEE Transactions on Antennas and Propagation*. 1980;28(3):412-416.

58. Morris G. A broad-band constant beamwidth corrugated rectangular horn. *IEEE Transactions on Antennas and Propagation*. 1982;30(5):966-974.

59. Kelleher KS, Parker CF. Constant Beamwidth Horn Antenna.US Patent, 2,946,999; 1960.

60. Clarricoats PJB, Olver AD. *Corrugated horns for microwave antennas.* London: Peter Peregrinus Ltd; 1984.

61. Granet C, James GL. Design of corrugated horns: a primer. *IEEE Antennas and Propagation Magazine*. 2005;47(2):76-84.

62. Clarricoats PJB, Saha PK. Propagation and radiation behaviour of corrugated feeds part 2-corrugated-conical-horn-feed. *Proceedings of IEE*. 1971;118(9):1177-1186.

63. Bryant GH. Propagation in corrugated waveguides. *Proceedings of IEE*. 1969;116(2):203-213.

64. Clarricoats PJB, Saha PK. Propagation and radiation behaviour of corrugated feeds part 1-corrugated-waveguide feed. *Proceedings of IEE*. 1971;118(9):1167-1176.

65. Love AW. *Electromagnetic horn antennas*. New York: IEEE Press; 1976.

66. Frank Z. Very wideband corrugated horns. *Electronic Letters*. 1975;11(6):131-133.

67. Elliott RS. On the theory of corrugated plane surfaces. *Proceedings of IRE*. 1951;39:952-959.

68. Encinar JA, Rebollar JM. A hybrid technique for analyzing corrugated and noncorrugated rectangular horns. *IEEE Transactions on Antennas and Propagation*. 1986;34(8):961-968.

69. Kuhn E, Watson BK. Rectangular corrugated horns – analysis, design and evaluation. *1984 14th European Microwave Conference*; 1984: IEEE.

70. Clarricoats PJB, Seng LM. Propagation and radiation characteristics of corrugated horns. *Electronics Letter*. 1973;9(1):7-9.

71. Rao S, Sharma SK, Shafai L. *Handbook of reflector antennas and feed systems, volume II, feed systems.* Artech House; 2013.

72. Abbas-Azimi M, Mazlumi F, Behnia F. Design of broadband constant-beamwidth conical corrugated-horn antennas. *IEEE Antennas and Propagation Magazine*. 2009;51(5):109-114.

73. Beniguel Y, Berthon A, Klooster CV, Costes L. Design realization and measurement of a high performance wide-band corrugated horn. *IEEE Transactions on Antennas and Propagation*. 2005;53(11):3540-3546.

74. Olver AD. Corrugated horns. *Microwave horns and feeds.* 1994:258-317.

75. Thomas BM. Design of corrugated conical horns. *IEEE Transactions on Antennas and Propagation.* 1978;26(2):367-372.

76. Kerr L, Timochko MJ. Broadband corrugated horn with double-ridged circular waveguide, US Patent, 4,021,814; 1977.

77. Ekstorm JL. The Z-matrix parameters of tapered transmission lines. *IRE Transactions on Circuit Theory*. 1962;9:132-135.

78. Takeda F, Hashimoto T. Broadbanding of corrugated conical horns by means of the ring-loaded corrugated waveguide structure. *IEEE Transactions on Antennas and Propagation*. 1976;24(6):786-792.

79. Hindman G, Hanjian, Yei WB. The implementation of a spherical near-field measurement system in Mainland China. *1997 Antenna Measurement Techniques Association Conference*; 1997: AMTA.

80. Kol Y, Herscovici N, Kastner R. Analysis and design of wideband constant beamwidth sectoral horns. *Journal of Electromagnetic Waves and Applications*. 1990;4(7):673-682.
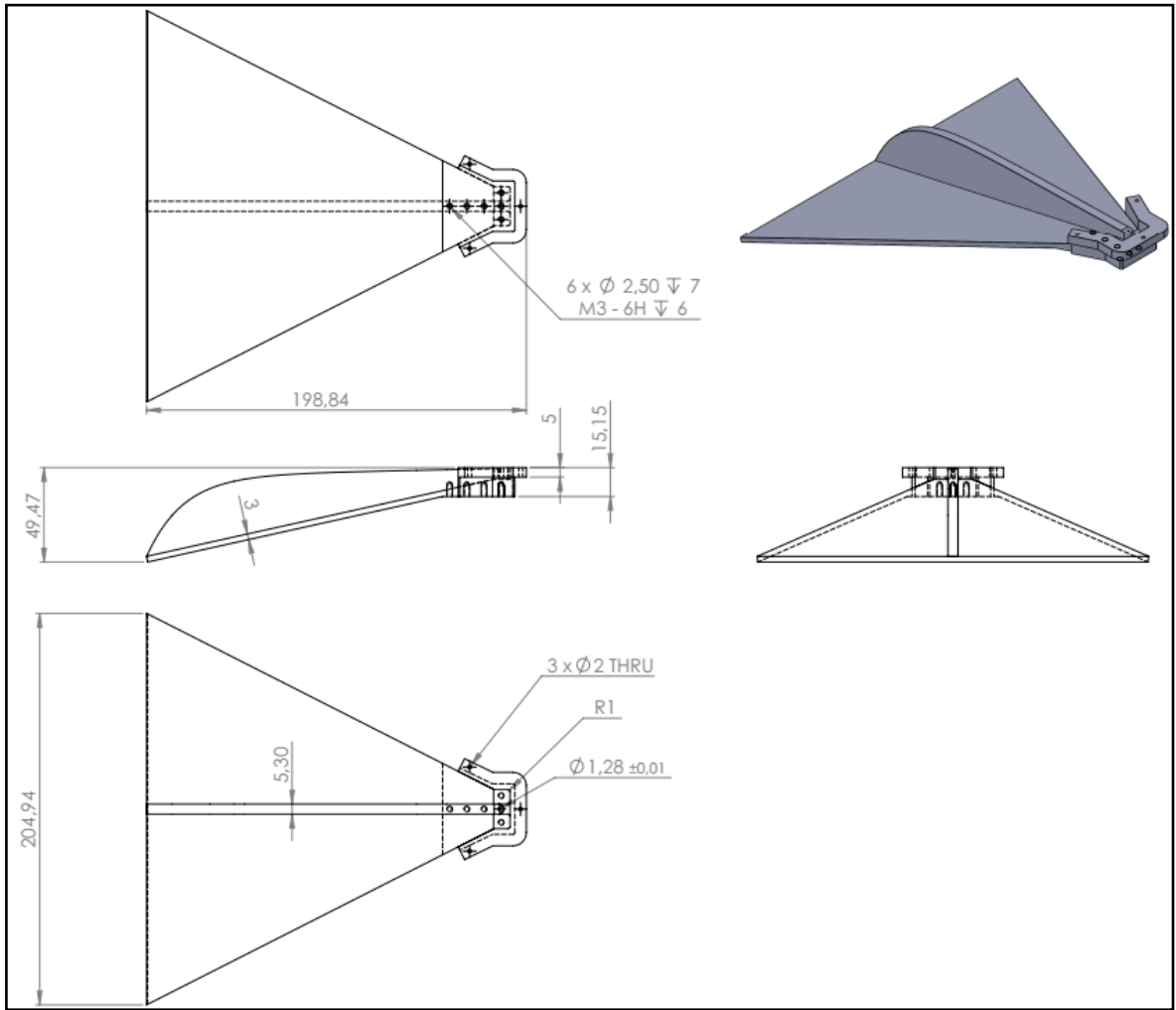
APPENDIX A: PRODUCTION PACKAGE OF CURVED PINWALL DRHA
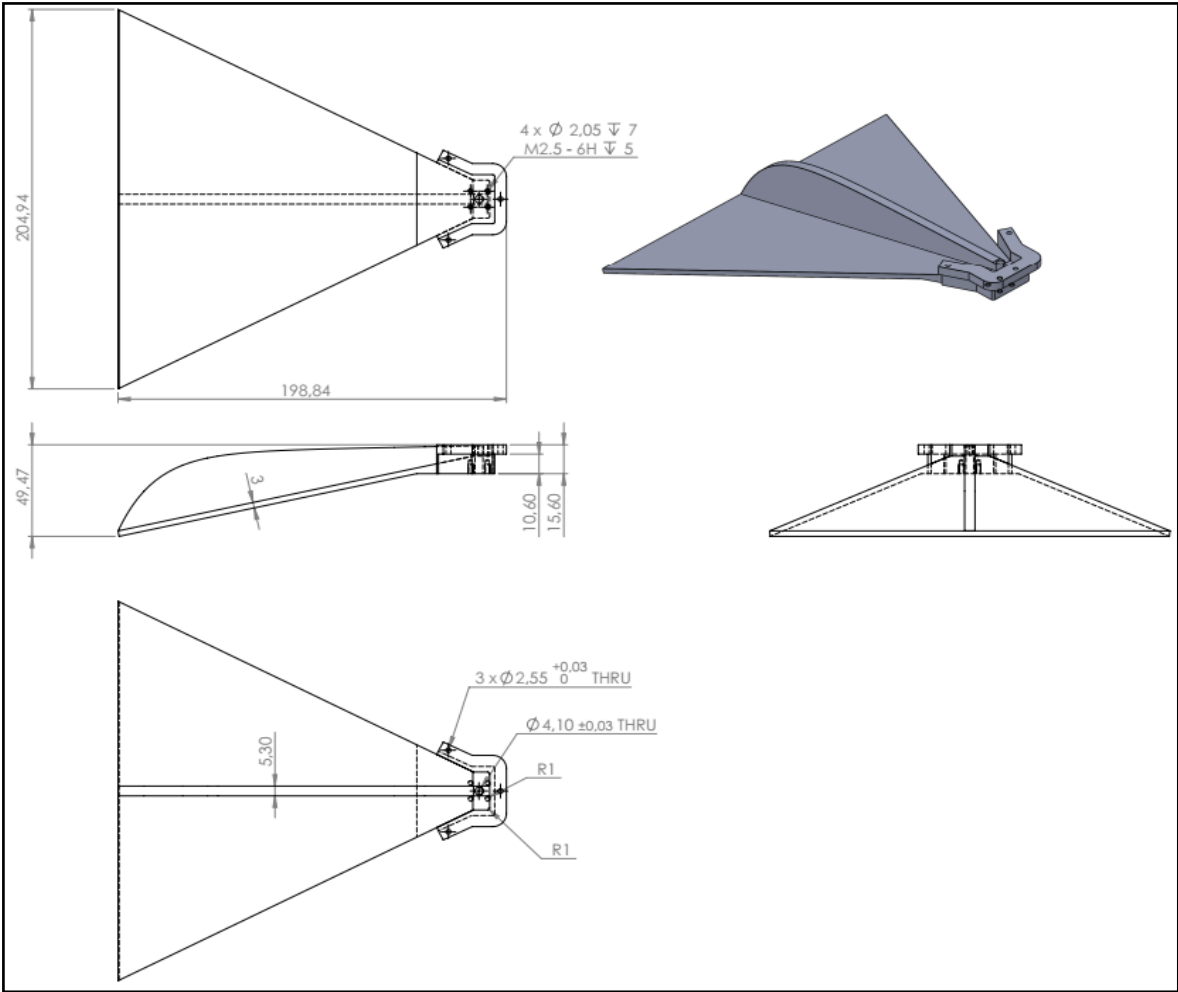

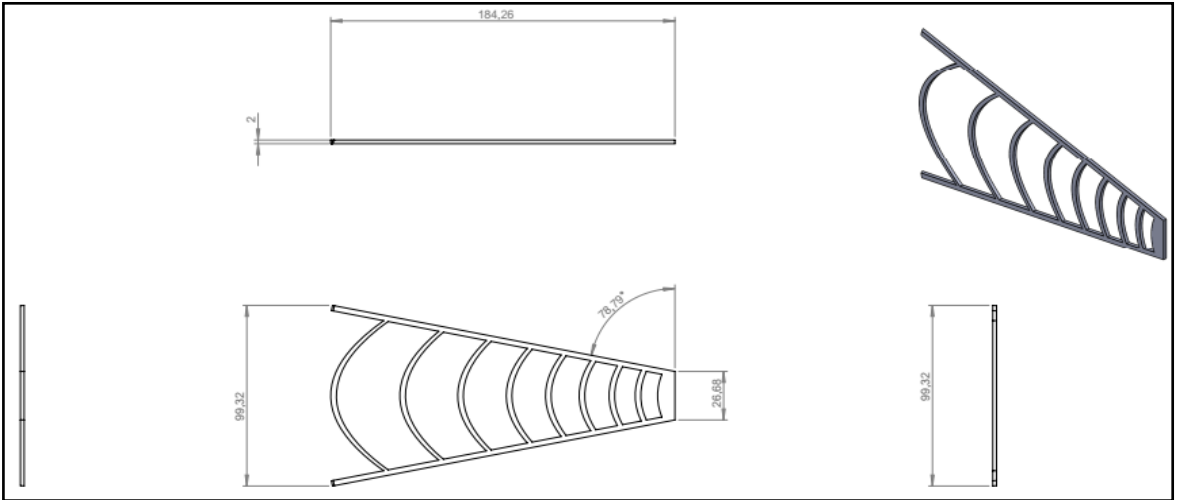Figure A.1. Bottom part

Figure A.2. Top part

Figure A.3. Side part

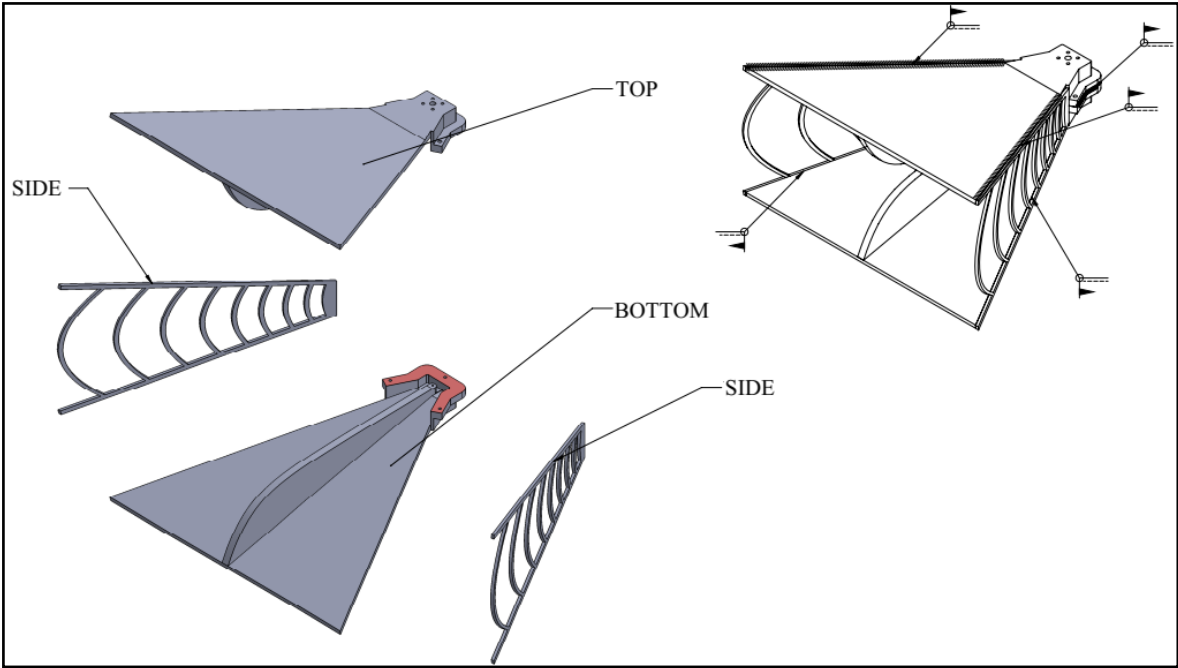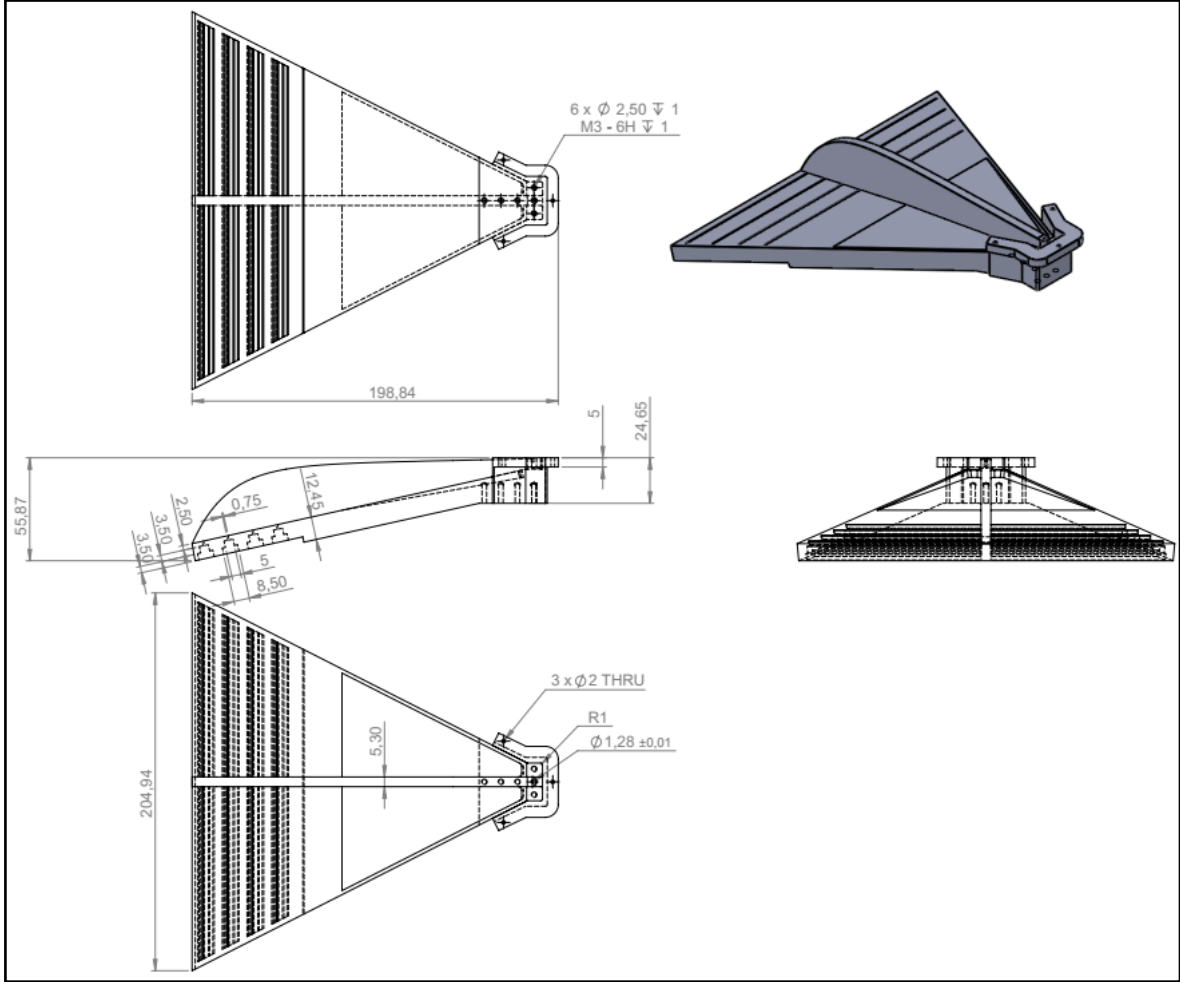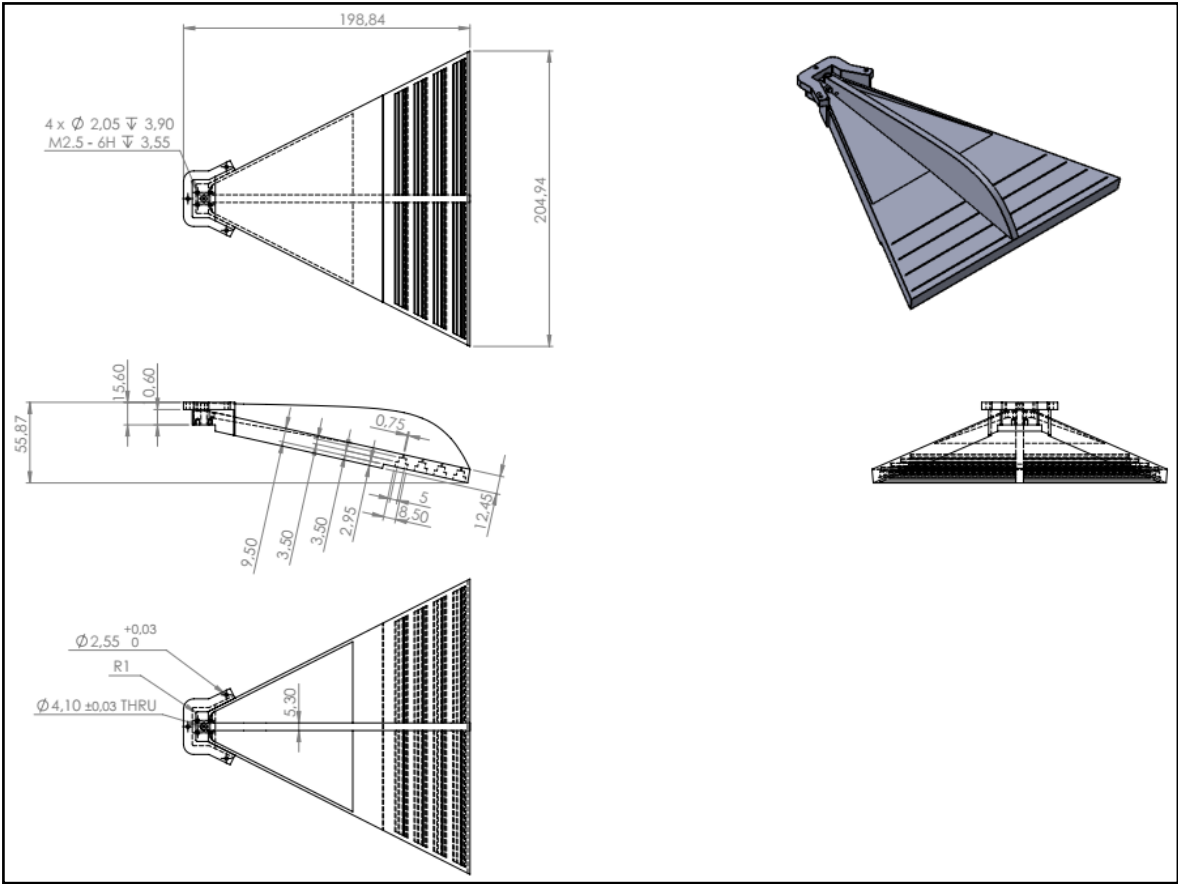Figure A.4. Integration by welding
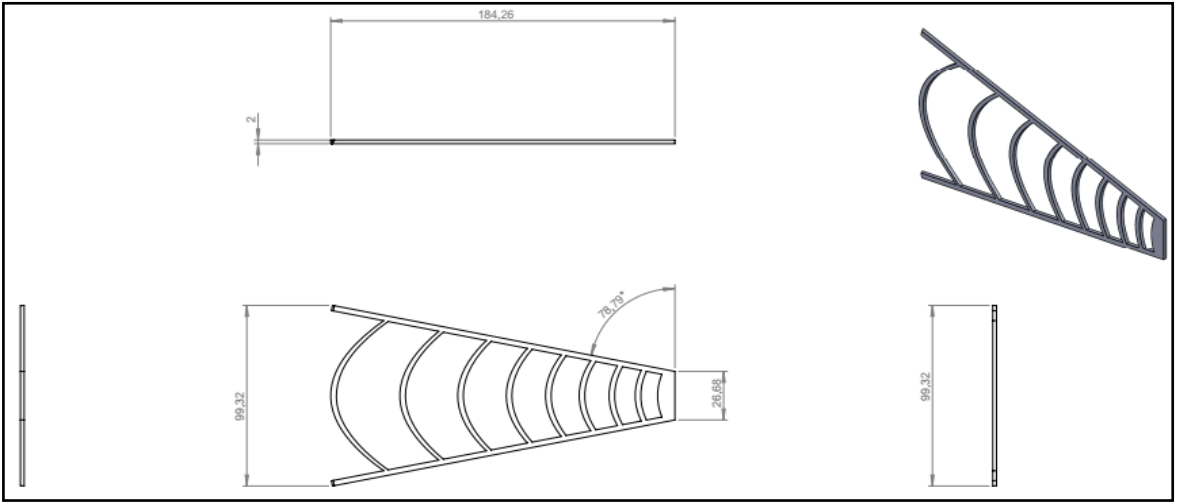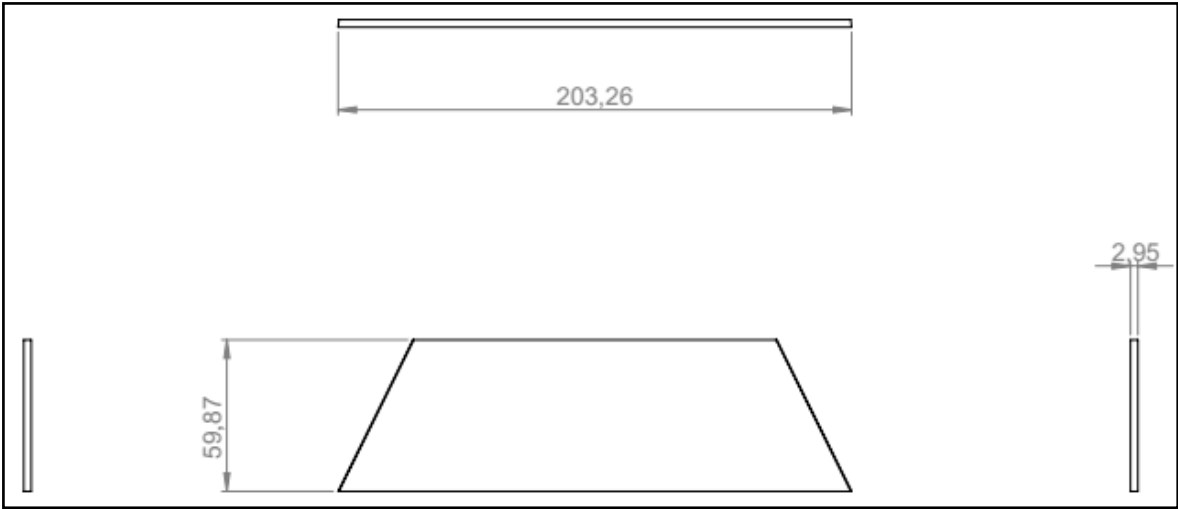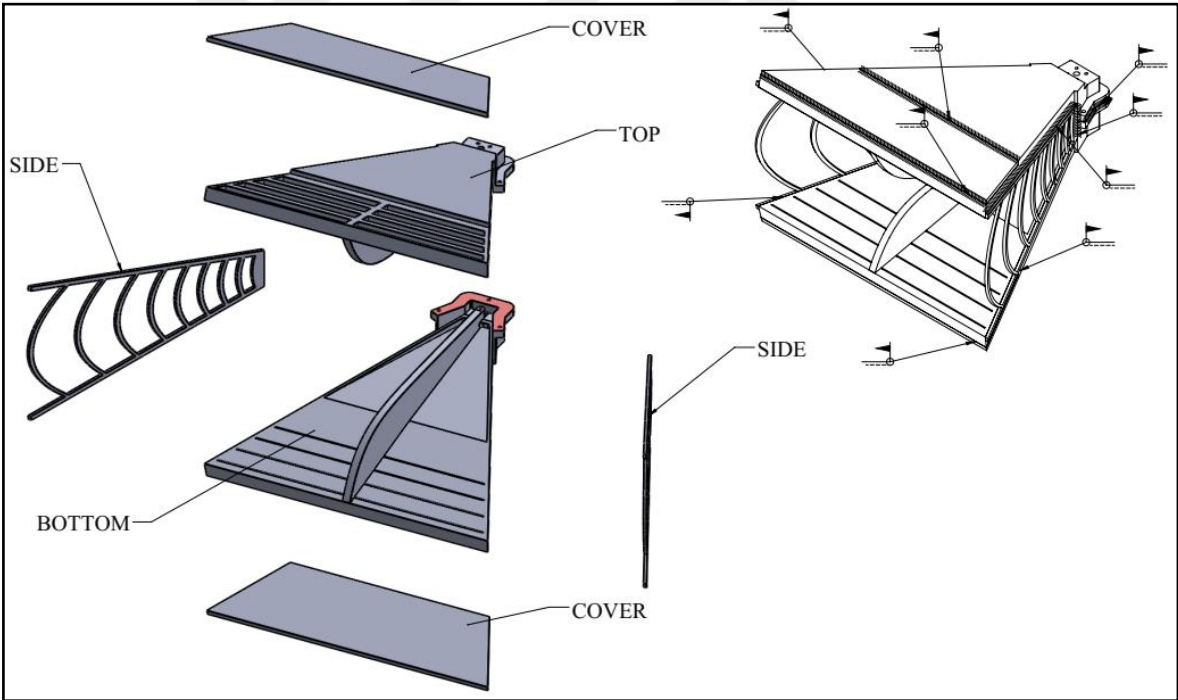
Figure B.2. Top part

Figure B.3. Side part

Figure B.4. Cover part

Figure B.5. Integration by welding